PD-linked LRRK2 G2019S mutation impairs astrocyte morphology and synapse maintenance via ERM hyperphosphorylation

Shiyi Wang[1,9], Ryan Baumert[1,9], Gabrielle Séjourné[1,9], Dhanesh Sivadasan Bindu[1,2], Kylie Dimond[3], Kristina Sakers[1,13], Leslie Vazquez[1,4,9], Jessica L. Moore[1,13], Christabel Xin Tan[5], Tetsuya Takano[6,7], Maria Pia Rodriguez[1], Nick Brose[1], Luke Bradley[1], Reed Lessing[1], Scott H. Soderling[1,8,9], Albert R. La Spada[10,11,12], and Cagla Eroglu[1,8,9,13]

[1]The Department of Cell Biology, Duke University Medical Center, Durham, NC, USA

[2]Department of Neonatology, Children's Mercy Hospital, Kansas City, MO, USA

[3]College of Psychology, Nova Southeastern University, Fort Lauderdale, FL, USA

[4]The Department of Neurobiology, Duke University Medical Center, Durham, NC, USA

[5]Life Sciences Institute, University of Michigan, Ann Arbor, MI, USA

[6]Division of Molecular Systems for Brain Function, Kyushu University Institute for Advanced Study, Medical Institute of Bioregulation, Japan

[7]Japan Science and Technology Agency, PRESTO, Japan

[8]The Department of Neurobiology, Duke University Medical Center, Durham, NC, USA

[9]Aligning Science Across Parkinson's (ASAP) Collaborative Research Network, Chevy Chase, MD

[10]The Department of Neurology, Duke University Medical Center, Durham, NC, USA

[11]Departments of Pathology & Laboratory Medicine, Neurology, Biological Chemistry, and Neurobiology & Behavior, University of California, Irvine, CA, USA

[12]UCI Center for Neurotherapeutics, University of California, Irvine, CA, USA

[13]Howard Hughes Medical Institute, Duke University Medical Center, Durham, NC, USA

Corresponding authors: Shiyi Wang: shiyi.wang@duke.edu;

Albert R. La Spada: alaspada@uci.edu;

Cagla Eroglu: cagla.eroglu@duke.edu

Abstract

Astrocytes are highly complex cells that mediate critical roles in synapse formation and maintenance by establishing thousands of direct contacts with synapses through their perisynaptic processes. Here, we found that the most common Parkinsonism gene mutation, LRRK2 G2019S, enhances the phosphorylation of the ERM proteins (Ezrin, Radixin, and Moesin), components of the perisynaptic astrocyte processes in a subset of cortical astrocytes. The ERM hyperphosphorylation was accompanied by decreased astrocyte morphological complexity and reduced excitatory synapse density and function. Dampening ERM phosphorylation levels in LRRK2 G2019S mouse astrocytes restored both their morphology and the excitatory synapse density in the anterior cingulate cortex. To determine how LRRK2 mutation impacts Ezrin interactome, we used an *in vivo* BioID proteomic approach, and we found that astrocytic Ezrin interacts with Atg7, a master regulator of autophagy. The Ezrin/Atg7 interaction is inhibited by Ezrin phosphorylation, thus diminished in LRRK2 G2019S astrocytes. Importantly, the Atg7 function is required to maintain proper astrocyte morphology. Our data provide a molecular pathway through which the LRRK2 G2019S mutation alters astrocyte morphology and synaptic density in a brain-region-specific manner.

45 ## INTRODUCTION

46 Most synapses in the central nervous system are in direct contact with perisynaptic
47 astrocyte processes (PAPs)[1], forming the “tripartite synapse”[1]. At the tripartite
48 synapse, astrocytes clear excess neurotransmitters, maintain ion homeostasis, and
49 secrete factors regulating synapse development and function[2]. To accomplish these
50 crucial functions, astrocytes develop elaborate morphologies to tile the entire brain
51 parenchyma[3-5]. Astrocyte morphogenesis and synaptogenesis are interdependent and
52 bidirectional[6, 7]. In neurological disorders like Parkinson’s Disease (PD), astrocytes
53 become reactive, undergoing morphological and molecular changes[8, 9]. Recent studies
54 suggested that astrocyte dysfunction contributes to PD[10-12]. However, the underlying
55 mechanisms are largely unknown.

56 Mutations in the leucine-rich repeat kinase 2 (*LRRK2*) gene cause familial PD[13,
57 14], with LRRK2 G2019S being the most common[15, 16]. It is largely accepted that
58 LRRK2 G2019S is a gain-of-function mutation that increases LRRK2’s kinase activity[17-
59 20]. Brain RNA-seq databases suggested that LRRK2 expressed in astrocytes[21, 22].
60 Previous studies also suggested ERM proteins (Ezrin, Radixin and Moesin) as LRRK2
61 substrates[18, 23, 24]. ERM proteins are structural components of perisynaptic astrocyte
62 processes (PAPs), with Ezrin being the most enriched in expression[25, 26]. Previous
63 studies suggested that LRRK2 phosphorylates a conserved threonine residue present in
64 all ERM proteins[18, 23, 24]. When phosphorylated, ERM proteins change conformation
65 and link the F-actin cytoskeleton to the cell membrane[27, 28]. This switch is thought to
66 play an important role in organizing cell morphology[28, 29]. Among the ERM proteins,
67 Ezrin is specifically and highly enriched in astrocytes and is known to localize at the PAPs

68 preferentially[25]. Genetic ablation or downregulation of Ezrin has been shown to alter
69 astrocyte morphology *in vivo*[30-33].

70 Here, we tested whether LRRK2 regulates astrocyte morphology and synaptic
71 densities using the LRRK2 G2019S knockin ($^{ki/ki}$) mouse model[34, 35] in conjunction with
72 *in vivo* astrocyte-specific genetic, proteomic, electrophysiological, and biochemical
73 approaches. We found that, in the prefrontal cortex of humans and mice carrying the
74 LRRK2 G2019S mutation, a subset of astrocytes has increased ERM (Ezrin, Radixin, and
75 Moesin) phosphorylation levels. This phospho-ERM change accompanies three
76 observations: Astrocytes have reduced morphological complexity; The anterior cingulate
77 cortex (ACC) has decreased excitatory (VGLUT1/PSD95) synapse density; The primary
78 motor cortex (MOp) has increased inhibitory (VGAT/Gephyrin) synapse density. By
79 overexpression of an Ezrin mutant that cannot be phosphorylated in astrocytes, we
80 dampened astrocytic ERM hyperphosphorylation. This reduction in astrocytic ERM
81 phosphorylation restored both LRRK2 G2019S astrocyte morphology and the ACC
82 excitatory synapse density. However, this phospho-ERM manipulation did not rescue the
83 MOp inhibitory synapse changes. We further compared *in vivo* Ezrin interactomes in WT
84 and LRRK2 G2019S$^{ki/ki}$ mouse cortical astrocytes. We discovered that Ezrin interacts with
85 a master regulator of autophagy, Atg7. This interaction is weakened by Ezrin's
86 phosphorylation. We also found that Atg7 is required for astrocyte morphological
87 complexity. Knocking down Atg7 in LRRK2 G2019S astrocytes partially restores their
88 morphology. This study shows that LRRK2-ERM pathways are important for astrocytes
89 to reach their morphological complexity. This study also hinted that astrocyte

90 morphological changes correlate with synapse density changes in a brain region-specific
91 manner.

92 **RESULTS**

93 **ERM phosphorylation is increased in the prefrontal cortices of mice and humans**
94 **carrying the LRRK2 G2019S mutation.**

95 To study how the LRRK2 G2019S mutation impacts astrocytes in the prefrontal
96 cortex, a cortical region linked to PD, we stained sections from the frontal cortices of age
97 and sex-matched control and LRRK2 G2019S mutation-carrying PD patients
98 (Supplemental Table 1) with glial fibrillary acidic protein (GFAP, a marker for astrocyte
99 branches) and phosphorylated ERM (Phospho-ERM, which are enriched in PAPs) (Figure
100 1A). Remarkably, the astrocytic organization, determined by GFAP staining, was severely
101 disrupted, and GFAP levels were significantly elevated (~42%) in PD patients carrying
102 the LRRK2 G2019S mutation, indicative of reactive gliosis (Figure 1B-C). Unexpectedly,
103 the phospho-ERM signal was increased by 7-fold in the frontal cortices of PD patients
104 carrying the LRRK2 G2019S mutation (Figure 1B-C). To determine if this ERM
105 hyperphosphorylation is cell type-specific we co-stained for phospho-ERM with astrocyte
106 marker S100β and neuronal dendrite marker MAP2. We found a significant increase in
107 phospho-ERM signal colocalized with both S100β and MAP2 (Figure S1A-C).

108 To determine whether ERM hyperphosphorylation is an early event in LRRK2
109 G2019S PD pathology, we used LRRK2 G2019S$^{ki/ki}$ mice, in which the human G2019S
110 mutation was introduced into exon 41 of the LRRK2 gene[34, 35]. To determine if ERM
111 hyperphosphorylation localizes to astrocytes, we crossed these mice to an astrocyte

112 reporter line carrying the Aldh1L1-eGFP transgene, which labels all astrocytes by
113 GFP[36]. We examined the phospho-ERM levels in coronal brain sections from 21-day-
114 old (P21, juvenile) and 12-week-old (P84, adult) WT or LRRK2 G2019S$^{ki/ki}$ mice.
115 Compared to WT mice, LRRK2 G2019S$^{ki/ki}$ mice across both age groups have a brain
116 region-specific and heterogeneous phospho-ERM increase (Figure 1D-L). This phospho-
117 ERM increase was localized to layers (L)1 and L2-3 of the anterior cingulate cortex (ACC)
118 and the primary motor cortex (MOp) (Figure 1E-L; Figure S2A-C) but was absent in both
119 the primary sensory cortex (SSp) and the dorsal medial striatum (DMS) (Figure S2D-I).
120 In P21 LRRK2 G2019S$^{ki/ki}$ mice, the phospho-ERM integrated densities in the ACC and
121 MOp L1 and L2-3 were increased by ~32% (ACC) and ~41% (MOp) compared to the
122 WTs (Figure 1I); In P84 LRRK2 G2019S$^{ki/ki}$ mice, the phospho-ERM integrated densities
123 were increased by ~57% (ACC) and ~37% (MOp) compared to the WTs (Figure 1L). In
124 the ACC and MOp L1 and L2/3 of LRRK2 G2019S$^{ki/ki}$ mice, phospho-ERM was
125 significantly increased and colocalized with S100β and MAP2 but not Iba1 (microglia
126 marker), with a predominant localization to astrocytes in the ACC and MOp of LRRK2
127 G2019S$^{ki/ki}$ mice (Figure S3A-C). We also confirmed the specificity of the phospho-ERM
128 antibody by treating brain sections from both mice and human samples with lambda
129 protein phosphatase (λ-PPase). λ-PPase dephosphorylates proteins[37]. In both cases,
130 the phospho-ERM signal was eliminated after λ-PPase treatment, confirming the
131 phospho-ERM antibody specificity (Figure S4A-F).

132 In the human samples, phospho-ERM elevation was observed concurrently with
133 reactive gliosis (elevated GFAP staining). To determine if, in LRRK2 G2019S$^{ki/ki}$ mice,
134 there were reactive astrocytes detectable at early ages, we stained sections from the

135 same P21 mouse brains with an anti-GFAP antibody. In the mouse cortex, grey matter
136 astrocytes do not display GFAP staining unless there is reactive gliosis[38, 39]. We did
137 not detect any increase in the levels of GFAP (Figure S5A-C). These data indicate that,
138 in LRRK2 G2019S$^{ki/ki}$ mice, phospho-ERM upregulation does not occur concurrently with
139 reactive astrogliosis. Moreover, distinct from the P21 and P84 LRRK2 G2019S$^{ki/ki}$ mice
140 where phospho-ERM was restricted to a subset of astrocytes in a brain region-specific
141 manner, in the human patient brains (~80 years old), phospho-ERM accumulation was
142 present equally in both astrocytes and neurons. These data suggest that ERM
143 hyperphosphorylation is an early and astrocyte-specific event in LRRK2 G2019S$^{ki/ki}$
144 mouse cortices; however, is more widespread in human patient brains.

145 **LRRK2 G2019S mutation alters excitatory and inhibitory synapse densities and**
146 **functions in the cortex.**

147 Previous studies did not observe dopaminergic neuron loss or motor dysfunction
148 in the LRRK2 G2019S$^{ki/ki}$ mice[40, 41]; however, synapse dysfunction at cortico-striatal
149 circuits was reported in adult mice[42]. Despite the critical role of LRRK2 in cortico-striatal
150 synapses and PD-related cortical circuits[43], whether LRRK2 G2019S affects cortical
151 synapse densities and function has not been explored. Understanding these cortical
152 synaptic abnormalities is crucial, as they may underlie the early cognitive deficits in PD.
153 Next, we investigated if LRRK2 G2019S mutation alters synaptic densities in the ACC
154 and MOp L1 and L2-3 (Figure 2A), regions in which ERM hyperphosphorylation within
155 astrocytes was observed.

156 We quantified the densities of excitatory and inhibitory intracortical synapses in
157 WT and LRRK2 G2019S$^{ki/ki}$ mice. To do so, we marked the excitatory synapses as the
158 co-localization of the presynaptic Vesicular Glutamate Transporter 1 (VGlut1) and the
159 Postsynaptic Density Protein (PSD95), whereas inhibitory synapses were labeled using
160 presynaptic Vesicular GABA Transporter (VGAT), and postsynaptic gephyrin [44, 45]
161 (Figure 2B). Structural synapses were identified as the apposition and co-localization of
162 presynaptic and postsynaptic markers, which are in two distinct neuronal compartments
163 (i.e., axons and dendrites) and would only appear to co-localize at synapses due to their
164 proximity[46].

165 Excitatory synapse density was quantified both at P21 and P84. In the ACC of the
166 LRRK2 G2019S$^{ki/ki}$ mice, there was a significant decrease in intracortical excitatory
167 synapse density in both layers and ages we analyzed (~30%) when compared to the WT
168 controls (Figure 2C-D and Figure S6A-B). However, no differences in excitatory synapse
169 density were observed between genotypes in the MOp (Figure 2E-F and Figure S6C-D).
170 When we quantified the densities of inhibitory synapses in the MOp, we found significant
171 differences between genotypes (~40% increase). In contrast, in the ACC of WT and
172 LRRK2 G2019S$^{ki/ki}$ mice, no differences were observed for inhibitory synapse density
173 (Figure 2G-J). These results revealed two changes in LRRK2 G2019S$^{ki/ki}$ mouse brains:
174 reduced excitatory synapse density in the ACC; increased inhibitory synapse density in
175 the MOp. These data suggested a brain region-specific synapse density change
176 associated with the LRRK2 G2019S mutation.

177 We then used electrophysiology to assess how altered synapse density in the ACC
178 and MOp of LRRK2 G2019S$^{ki/ki}$ mice affects synaptic function. We recorded miniature

179 excitatory postsynaptic currents (mEPSCs) in the ACC L2-3 pyramidal neurons and
180 miniature inhibitory postsynaptic currents (mIPSCs) in the MOp L2-3 pyramidal neurons
181 from acute brain slices of P84 WT and LRRK2 G2019S$^{ki/ki}$ mice. LRRK2 G2019S$^{ki/ki}$
182 neurons displayed reduced mEPSC frequency by ~65% and a corresponding right shift
183 in the cumulative distributions of mEPSC inter-event intervals (Figure 3A-B) when
184 compared to WT neurons, with no change in mEPSC amplitude (Figure 3C). mEPSC
185 frequency changes correlate with synapse densities and/or the probability of presynaptic
186 glutamate release[47], whereas mEPSC amplitude indicates the synaptic strength
187 reflecting the number of AMPARs at the postsynapse[48]. Therefore, together with our
188 anatomical data, these findings suggest that the LRRK2 G2019S mutation reduces the
189 number of intracortical excitatory connections formed on L2-3 pyramidal neurons in the
190 ACC without altering synaptic strength. In contrast, in the MOp, LRRK2 G2019S$^{ki/ki}$
191 neurons exhibited a ~72% increase in mIPSC frequency compared to WT, with no
192 significant change in amplitude (Figure 3D-F). These data indicate that inhibitory synapse
193 density is elevated in the MOp of the LRRK2 G2019S$^{ki/ki}$ mice.

194 **Reducing ERM hyperphosphorylation in astrocytes restores excitatory synapse**
195 **density and function in the ACC of adult LRRK2 G2019S$^{ki/ki}$ mice.**

196 LRRK2 phosphorylates a conserved threonine residue present in all ERM
197 proteins[18, 23]. We found that LRRK2 G2019S mutation increases ERM phosphorylation
198 in astrocytes (Figure 1) and asked if dampening ERM phosphorylation in astrocytes could
199 restore synapse densities in LRRK2 G2019S$^{ki/ki}$ mice. To test this, we overexpressed a
200 phospho-dead Ezrin mutant, which cannot be phosphorylated, in astrocytes via

201 adenovirus (AAV) retro-orbital injection. We chose Ezrin because Ezrin is highly abundant
202 and specifically enriched in astrocytes compared to its family members, Radixin and
203 Moesin[21] (Figure S7A-B). Switching the amino acid threonine (T) at location 567 with
204 alanine (A) results in a version of the protein that cannot be phosphorylated (Phospho-
205 dead Ezrin, Figure S7C)[28, 29].

206 To determine if phospho-dead Ezrin can reduce ERM phosphorylation in
207 astrocytes of LRRK2 G2019S$^{ki/ki}$ mice, we retro-orbitally injected 9-week-old WT and
208 LRRK2 G2019S$^{ki/ki}$ mice with AAVs to express Hemagglutinin (HA)-tagged WT Ezrin or
209 phospho-dead Ezrin under the control of the astrocyte-specific GfaABC1D promoter
210 (Figure S7D). The GfaABC1D promoter ensures astrocyte-specific expression, as
211 validated in prior work[49]. While AAV serotypes may infect multiple cell types, our data
212 support astrocyte-specific expression based on promoter specificity and cell labeling. 3
213 weeks after injection, the mouse brains were harvested for histological analyses. The
214 widespread viral expression of Ezrin in astrocytes was verified by staining with an anti-
215 HA tag antibody (Figure 4A). While WT or phospho-dead Ezrin overexpression had no
216 effect on ERM phosphorylation in WT brains, WT Ezrin increased phospho-ERM levels
217 in LRRK2 G2019S$^{ki/ki}$ astrocytes; phospho-dead Ezrin abolished this increase (Figure 4A-
218 B). This indicates that the LRRK2 G2019S sensitizes astrocytes to LRRK2-mediated
219 ERM phosphorylation. To determine the specificity of phospho-dead Ezrin, we examined
220 the hyperphosphorylation of another LRRK2 substrate, Rab10 (Thr 73)[19, 50]·[51]. We
221 found higher Rab10 phosphorylation in LRRK2 G2019S$^{ki/ki}$ brain sections than in WT mice.
222 However, neither WT nor phospho-dead Ezrin overexpression impacted Rab10

223 phosphorylation (Figure S8), showing that phospho-dead Ezrin selectively reduces ERM
224 hyperphosphorylation in astrocytes.

225 We next tested whether reducing ERM hyperphosphorylation in astrocytes could
226 rescue synaptic deficits in LRRK2 G2019S$^{ki/ki}$ ACC and MOp. We found that, in WT ACC,
227 WT Ezrin overexpression in astrocytes had no effect on excitatory synapse density
228 (Figure S9). However, compared to WT mice overexpressing WT Ezrin, overexpression
229 of phospho-dead Ezrin in WT astrocytes reduced excitatory synapse density by ~30%
230 (Figure 4C-D). In contrast, in LRRK2 G2019S$^{ki/ki}$ astrocytes, overexpression of phospho-
231 dead Ezrin increased the LRRK2 G2019S$^{ki/ki}$ ACC excitatory synapse density. This
232 increase brings the excitatory synapse density of LRRK2 G2019S$^{ki/ki}$ ACC similar to those
233 of WT ACC overexpressing astrocytic WT Ezrin (Figure 4C-D). We also found that, in the
234 MOp L1 and L2-3 of LRRK2 G2019S$^{ki/ki}$ mice, neither the WT nor the phospho-dead Ezrin
235 overexpression in adult astrocytes restored inhibitory synapse density back to the levels
236 in the WT MOp overexpressed with WT Ezrin (Figure S10). These data indicate that
237 phospho-dead Ezrin expression in adult WT or LRRK2 G2019S$^{ki/ki}$ astrocytes is sufficient
238 to modify excitatory synapse density in the ACC but cannot alter inhibitory synapse
239 density in the MOp. It is plausible that LRRK2 G2019S mutation impairs inhibitory
240 synapses in the MOp by altering the number or connectivity of cortical interneurons
241 through a developmental mechanism. Thus, manipulation in adults is insufficient to rectify
242 this inhibitory synapse phenotype.

243 Because astrocytic overexpression of phospho-dead Ezrin impacted excitatory
244 synapse density in the ACC of WT and LRRK2 G2019S$^{ki/ki}$ mice, we next performed
245 whole-cell patch-clamp recordings from ACC L2-3 pyramidal neurons transduced with the

246 same AAVs. In LRRK2 G2019S$^{ki/ki}$ ACC L2-3, overexpression of WT Ezrin in astrocytes
247 did not rescue the decreased frequency of mEPSCs. However, overexpression of
248 phospho-dead Ezrin in LRRK2 G2019S$^{ki/ki}$ astrocytes restored the frequency up to the
249 levels of WT mice expressing WT Ezrin (Figure 4E-F). Interestingly, in WT ACC L2-3,
250 overexpression of phospho-dead Ezrin in WT astrocytes significantly reduced the
251 frequency of mEPSCs (~54%) (Figure 4E-F). Posthoc comparisons confirmed no
252 significant differences in mean mEPSC amplitudes across all 4 conditions (Figure 4G).

253 Altogether, these electrophysiological and neuroanatomical analyses reveal that
254 the LRRK2 G2019S mutation dysregulates proper excitatory and inhibitory synapse
255 densities and functions in the cortex in a brain region-specific manner. These results also
256 pinpoint a link between ERM hyperphosphorylation in LRRK2 G2019S astrocytes (Figure
257 1) and the excitatory synaptic density change in the ACC (Figures 2 and 3). Our results
258 suggest that balancing ERM phosphorylation in astrocytes plays a role in maintaining
259 excitatory synapse density and function in the ACC.

260 **LRRK2 regulates astrocyte morphological complexity *in vivo* through ERM**
261 **phosphorylation.**

262 In the brain, astrocytes have numerous functions[2]. To accomplish these functions,
263 astrocytes develop elaborate morphologies[3-5]. Astrocyte morphology is a crucial
264 indicator for its function. We next asked whether ERM hyperphosphorylation in LRRK2
265 G2019S astrocytes would impair their morphological complexity. To answer this question,
266 we sparsely labeled astrocytes with a membrane-targeted fluorescent protein (mCherry-
267 CAAX) using postnatal astrocyte labeling by electroporation (PALE). To image and

268 reconstruct the morphology of individual whole astrocytes, we collected 100-μm thick
269 mouse brain sections (Figure S11A). We focused our analyses of astrocyte territory size
270 and complexity on the ACC and MOp L1 and L2-3 at P21 (see Methods for details). We
271 found that, compared to WT astrocytes, both the territory volumes and morphological
272 complexity of LRRK2 G2019S astrocytes were significantly reduced (by ~34%) (Figure
273 5A-C). However, this alteration of astrocyte morphology did not change the number of
274 ALDH1L1+/SOX9+ cells (number of astrocytes) in the LRRK2 G2019S$^{ki/ki}$ ACC and MOp
275 (Figure S11B-D). Together, these results reveal that, *in vivo*, LRRK2 G2019S mutation
276 reduces both astrocyte territory volume and morphological complexity without affecting
277 astrocyte numbers.

278 Because phospho-dead Ezrin overexpression in astrocytes differentially impacts
279 synapse densities and function in WT and LRRK2 G2019S$^{ki/ki}$ mice (Figure 4), we
280 wondered if overexpression of phospho-dead Ezrin would also impact astrocyte
281 morphology differently between genotypes. We found that, in the ACC and MOp, the
282 overexpression of phospho-dead Ezrin decreased the WT astrocyte territory volume and
283 morphological complexity but restored LRRK2 G2019S$^{ki/ki}$ astrocyte territory volume and
284 complexity (Figure 5A-C). These results suggested that unphosphorylated Ezrin
285 differentially regulates astrocyte morphology in WT versus LRRK2 G2019S$^{ki/ki}$ astrocytes.
286 We postulated that Ezrin's conformational status may need to be tightly regulated for
287 proper astrocyte morphogenesis (Figure 5D). In LRRK2 G2019S$^{ki/ki}$ astrocytes, Ezrin is
288 more likely to be in a phosphorylated and open state. This would deplete the presence of
289 the closed unphosphorylated Ezrin. Such a distorted phospho-Ezrin balance may explain
290 the morphological defects of LRRK2 G2019S$^{ki/ki}$ astrocytes. To test this possibility, we

291 sought to shift the balance in the opposing direction by reducing Ezrin phosphorylation
292 through the knockdown of mouse Lrrk2. Similar to LRRK2 G2019S$^{ki/ki}$ astrocytes,
293 astrocytes transfected with shLrrk2 (~90% *Lrrk2* reduction, Figure S12A-B) exhibited
294 significantly smaller territory volumes (~36% reduction) and reduced complexity (Figure
295 5E-G).

296 Previous studies suggested phosphorylation at T567 promotes Ezrin acquiring an
297 open conformation by binding to phosphatidylinositol-4,5-bisphosphate (PIP2)[52]. In this
298 conformation, the N-terminus interacts with membrane proteins, and the C-terminus is
299 available to bind to the actin cytoskeleton[53, 54]. An Ezrin mutant in which the T567
300 residue is switched to aspartate (D) prefers Ezrin's open conformation, thereby mimicking
301 the phosphorylated state (Phospho-mimetic Ezrin, Figure S4C)[55, 56]. When we
302 overexpressed phospho-mimetic Ezrin in astrocytes, we found that phospho-mimetic
303 Ezrin restored the territory volume and morphological complexity of shLRRK2 astrocytes
304 (Figure 5E-G) but had no effect on shControl astrocytes (Figure 5E-G). These results
305 show that both the gain of LRRK2 kinase function (in LRRK2 G2019S$^{ki/ki}$ mice) and the
306 loss of LRRK2 function (shLRRK2) decrease astrocyte complexity and size and the
307 manipulation of Ezrin conformational/phosphorylation states in opposing directions
308 (expression of phospho-dead or phospho-mimetic Ezrin respectively) can rescue these
309 morphological phenotypes.

310 **LRRK2 G2019S mutation changes Ezrin interactome in astrocytes**

311 To investigate how ERM hyperphosphorylation affects astrocyte morphology in
312 LRRK2 G2019S$^{ki/ki}$ astrocytes, we identified possible Ezrin interactors in WT and LRRK2

313 G2019S$^{ki/ki}$ astrocytes by *in vivo* astrocyte-specific proximity labeling. We used two virally
314 encoded astrocyte-specific biotin ligase probes: Ezrin fused with BioID (Astro-Ezrin-BioID)
315 and soluble BioID with a nuclear export sequence (Astro-Cyto-BioID) (Figure 6A). These
316 were delivered via intracortical AAV injections to P0-2 WT and LRRK2 G2019S$^{ki/ki}$ mouse
317 pups, followed by subcutaneous biotin injections starting at P18 for 3 days, and tissue
318 collection at P21 (Figure 6B). Biotinylated proteins were detected in astrocytes using
319 immunohistochemistry and immunoblotting for HA and Streptavidin (Figure S13).

320 Affinity-purified proteins from cortices were analyzed using quantitative liquid
321 chromatography-tandem mass spectrometry (LC-MS) (Figure 6B), identifying 30,815
322 unique peptides corresponding to 4,081 unique proteins (Supplemental Tables 2-4).
323 Principle component analyses (PCA) of BioID results showed that distinct clustering
324 between Cyto-BioID (control) and Ezrin-BioID (bait) samples, with further separation
325 between WT or LRRK2 G2019S$^{ki/ki}$ astrocytes (Figure S14A). Radixin and Moesin, known
326 as Ezrin family proteins, were significantly enriched in the Ezrin-BioID sample compared
327 to Cyto-BioID (Figure S14B)[57]. Comparative analysis revealed 344 proteins with
328 significantly altered proximity to Ezrin in LRRK2 G2019S$^{ki/ki}$ astrocytes (fold-change >1.5
329 or < -1.5, $p < 0.05$); 190 gained, and 154 lost Ezrin proximity (Figure 6C; Figure S14C-D;
330 Supplemental Table 5). Gene Ontology (GO) analysis of these proteins showed
331 enrichment in phospholipid binding, microtubule binding, and membrane transporter and
332 cell-adhesion mediator activity were over-represented in differentially enriched proteins
333 (Figure 6D; Supplemental Table 6). This aligns with our model that the LRRK2 G2019S
334 mutation would shift Ezrin towards its phosphorylated/open state, promoting membrane
335 interactions. Unexpectedly, GO-term analyses of biological processes highlighted

336 enrichment in catabolic processes, macroautophagy, negative regulation of
337 developmental growth, and intracellular transport (Figure 6E; Supplemental Table 7).
338 These findings indicated that Ezrin plays a role in these biological processes, which are
339 altered by the LRRK2 G2019S mutation.

340 Previous studies showed macroautophagy deficits in neurons with the LRRK2
341 G2019S mutation[58]. To assess global cytosolic changes, we analyzed the Astro-Cyto-
342 BioID dataset across genotypes, identifying 195 differentially enriched proteins (78 gained,
343 117 lost in LRRK2 G2019S$^{ki/ki}$; Figure S14E; Supplemental Table 8). GO-term analysis
344 revealed an enrichment of proteins associated with phospholipid binding and vesicle
345 trafficking (Figure S14F-G; Supplemental Tables 9-10). However, macroautophagy-
346 related terms were not enriched, suggesting that the observed changes in Ezrin-BioID
347 are specifically related to alterations in Ezrin function in the LRRK2 G2019S$^{ki/ki}$ astrocytes.

348 BioID captures proteins in close proximity to the bait but does not guarantee direct
349 interactions. To identify potential direct Ezrin interactors affected by LRRK2 G2019S, we
350 compared protein abundance in Astro-Ezrin-BioID to Astro-Cyto-BioID within each
351 genotype (Ezrin/Cyto fold -change > 1.5, $p < 0.05$, 346 proteins in WT and 335 proteins
352 in LRRK2 G2019S$^{ki/ki}$; Supplemental Tables 11-12). To generate high-confidence lists of
353 interactors that gained or lost proximity to Ezrin in LRRK2 G2019S$^{ki/ki}$ astrocytes, we set
354 a second requirement for proteins with fold-change > 1.5 or < -1.5 between LRRK2
355 G2019S$^{ki/ki}$ and WT Astro-Ezrin-BioID. Using these filters, we narrowed down our list to
356 28 as “gained proximity to Ezrin in LRRK2 G2019S astrocytes” and 30 as “lost proximity
357 to Ezrin in LRRK2 G2019S astrocytes” (Figure 6F-H; Supplemental Table 13).
358 Upregulated proteins, such as Rala, Cops3, and Anks1a, are involved in vesicular

359 trafficking, cell signaling, and cytoskeletal regulation, aligning with enhanced ERM
360 phosphorylation and their recruitment to the plasma membrane. In contrast, the
361 downregulated proteins (e.g., Atg7, Cul4b, Myo1e, Irs1) suggest a disruption in
362 intracellular trafficking and autophagy due to excessive ERM phosphorylation. Together,
363 these data map Ezrin interactomes in WT and LRRK2 G2019S$^{ki/ki}$ mouse cortical
364 astrocytes *in vivo*, revealing changes in Ezrin interactions with proteins involved in
365 catabolic processes and autophagy. This highlights a potential molecular mechanism
366 linking LRRK2-Ezrin signaling to astrocyte morphogenesis.

367 **Atg7 is an Ezrin interactor that is required for proper astrocyte morphogenesis**

368 Among high-confidence astrocytic Ezrin interactors, we identified autophagy-
369 related gene 7 (Atg7), a crucial autophagy regulator, which was enriched (~2.3-fold) in
370 the Ezrin-BioID fraction of WT astrocytes but de-enriched (0.5-fold) in the Ezrin-BioID
371 fraction of LRRK2 G2019S$^{ki/ki}$ astrocytes compared to the Cyto-BioID. Atg7 is essential
372 for autophagy initiation and has been implicated in neurological disorders[59],[60].
373 However, its role in astrocytes and its interaction with Ezrin is unclear. To explore this,
374 we used AlphaFold-2.0 Multimer[61] to model the structures of Ezrin and Atg7 alone or in
375 complex.

376 Atg7, a homodimer, has two globular domains: An N-terminal domain and a C-
377 terminal domain that are separated by a short flexible linker. The C-terminal domain is
378 further divided into the adenylation and extreme C-terminal domains (Figure 7A-B)[62].
379 Ezrin has an N-terminal FERM (four-point one, Ezrin, Radixin, Moesin) domain
380 (subdivided into three subdomains- F1, F2, and F3), α-helical domain, and a C-terminal

381 ERM Association domain (C-ERMAD) (Figure 7C)[56]. Upon phosphorylation of T567 and
382 binding to PIP2, Ezrin adopts an open conformation (Figure 7D; see Methods for details
383 of modeling)[63]. We then predicted the structure of the complex formed between the
384 closed conformation of Ezrin and the homodimer of Atg7 (Figure 7E). Alpha-fold 2.0
385 multimer, in conjunction with CABS-Flex 2.0 (https://biocomp.chem.uw.edu.pl/CABSflex2,
386 RRID: SCR_025674) and PyMol (http://www.pymol.org/, RRID: SCR_000305), were
387 used to predict and assess conformational changes in Atg7 and Ezrin after binding each
388 other (Figure 7F). When Ezrin binds Atg7, it is predicted to undergo drastic conformational
389 changes in its α-helical domain, which is pulled towards the ERMAD and FERM domains,
390 whereas the changes in the Atg7 dimer structure after Ezrin binding are minimal (Figure
391 7F).

392 To validate the interaction between Ezrin and Atg7, we performed co-
393 immunoprecipitation (Co-IP) in HEK293T cells overexpressing Myc-tagged Atg7 (Atg7-
394 Myc) and HA-tagged WT Ezrin. To understand how the open or closed conformation of
395 Ezrin would impact the Ezrin – Atg7 interaction, we also conducted Co-IPs with
396 modulation of Ezrin phosphorylation levels: phospho-mimetic T567D ("TD", open) and
397 phospho-dead T567A ("TA", closed) Ezrin. We found that WT Ezrin or phospho-dead
398 Ezrin coimmunoprecipitated with Myc-Atg7, indicating that Atg7 interacts with WT Ezrin
399 or phospho-dead Ezrin (Figure 7G). However, the interaction between Atg7 and phospho-
400 mimetic Ezrin was significantly reduced (Figure 7H). These results support a
401 phosphorylation-dependent interaction between Ezrin and Atg7, consistent with our BioID
402 data showing reduced Atg7-Ezrin interaction in LRRK2 G2019S$^{ki/ki}$ astrocytes.

403 To test if Atg7 is required for astrocyte morphology, we developed a short hairpin
404 RNA (shRNA) that targets both rat and mouse *Atg7,* which effectively reduced *Atg7*
405 mRNA in mouse cells (Figure S15A). Knockdown of Atg7 in rat astrocytes significantly
406 reduced neuron-induced astrocyte morphogenesis *in vitro* in a neuron-astrocyte co-
407 culture assay (Figure S15B-C). *In vivo*, Atg7 knockdown in WT astrocytes reduced
408 astrocyte territory volume and morphological complexity, resembling the LRRK2
409 G2019S$^{ki/ki}$ astrocytes transfected with shControl (Figure 7I-K). In LRRK2 G2019S$^{ki/ki}$
410 astrocytes, Atg7 knockdown improved morphological complexity but did not further
411 reduce territory volume (Figure 7J-K). These findings highlight Atg7's role in regulating
412 astrocyte morphology and suggest its dysfunction in LRRK2 G2019S$^{ki/ki}$ astrocytes
413 contributes to altered morphology.

414 DISCUSSION

415 Here, we describe a previously unknown role for LRRK2, a PD-linked gene, in
416 controlling astrocyte morphological complexity by regulating the phosphorylation state of
417 ERM proteins. In the presence of LRRK2 G2019S mutation, we found enhanced ERM
418 phosphorylation in human and mouse cortical astrocytes. ERM hyperphosphorylation in
419 the LRRK2 G2019S background is specific to a subset of the ACC and MOp astrocytes
420 of juvenile and adult mice. Previous studies suggested a direct interaction between
421 LRRK2 and ERM proteins[18] and that ERM proteins are substrates of LRRK2[23, 24].
422 However, whether the enhanced ERM phosphorylation in LRRK2 G2019S astrocytes is
423 due to a direct effect of LRRK2 kinase is unclear. Several other kinases, such as
424 lymphocyte-oriented kinase, STE20-like protein kinase (SLK), and Rho kinase, were
425 found to be involved in ERM phosphorylation[64], suggesting the enhanced ERM

426 phosphorylation we observed in LRRK2 G2019S brains may be an indirect effect of the
427 LRRK2 G2019S mutation on the activities of these kinases.

428 **How does ERM phosphorylation control astrocyte morphology and synaptogenic**
429 **functions?**

430 The canonical function of ERM proteins is linking the actin cytoskeleton with the
431 plasma membrane, thus allowing cellular process outgrowth and morphogenesis[53]. Our
432 findings suggest that disruptions in the interaction between Ezrin and a core autophagy-
433 related protein, Atg7, contribute to the altered astrocyte morphology observed in LRRK2
434 G2019S$^{ki/ki}$ mice. *In vivo* Ezrin interactome in astrocytes included several other proteins
435 related to autophagy, which changed their proximity to Ezrin in the LRRK2 G2019S$^{ki/ki}$
436 astrocytes, compared to WT astrocytes. These observations indicate that LRRK2
437 G2019S-induced ERM hyperphosphorylation may impair astrocyte autophagy and cause
438 astrocyte dysfunction.

439 Another intriguing observation is that, *in vivo*, knocking down Atg7 in WT
440 astrocytes reduces astrocyte morphological complexity. Atg7 is a homodimeric E1-like
441 enzyme essential for autophagy, which maintains cellular homeostasis by degrading and
442 recycling damaged organelles and proteins[59]. Autophagic dysregulation is linked to
443 neurodegenerative diseases, including those associated with PD-related LRRK2
444 mutations[40, 65],[58]. However, the role of autophagy in astrocyte morphology and
445 synaptogenic functions is not well understood, nor is the impact of LRRK2 G2019S on
446 autophagy in astrocytes. It is possible that Atg7 depletion disrupts autophagic flux,

447 causing the accumulation of damaged components that compromise astrocyte structure
448 and function.

449 Our data also show that Atg7 knockdown in LRRK2 G2019S astrocytes does not
450 worsen their morphological defects. The G2019S mutation enhances LRRK2's kinase
451 activity, leading to aberrant phosphorylation of Rab proteins and trapping them on the
452 membrane surface[66]. Our studies revealed that Atg7/Ezrin interaction requires the
453 unphosphorylated form of Ezrin. It is plausible that this interaction, which is impaired in
454 LRRK2 G2019S astrocytes, diminished astrocytic Atg7 function. Therefore, additional
455 knockdown of Atg7 in LRRK2 G2019S astrocytes does not further reduce their size and
456 complexity. Instead, LRRK2 G2019S astrocytes may try to compensate by upregulating
457 catabolic pathways like ubiquitination and proteasomal degradation. These mechanisms
458 are crucial for clearing misfolded or damaged proteins in the absence of functional
459 endolysosomal function and may help mitigate the loss of autophagic flux[67, 68]. Our
460 Ezrin BioID dataset also showed that Nedd4l, an E3 ubiquitin ligase[69], lost proximity to
461 Ezrin in LRRK2 G2019S astrocytes (Figure 6).

462 Astrocytes regulate synapse formation and function through cell adhesion
463 molecules and secreted proteins that signal to neurons[6]. Synaptogenic proteins like
464 Hevin and thrombospondins shape cortical excitatory circuits[70],[71]. ERM proteins are
465 known to link the actin cytoskeleton with the plasma membrane, supporting cellular
466 process outgrowth and morphogenesis[63, 72, 73], but their role in secretion is less
467 understood. Phosphorylation of ERM proteins may refine secretory mechanisms in
468 astrocytes or regulate synapse elimination via phagocytosis. In agreement with this
469 possibility, a recent study found that synapses are more likely to be eliminated if phospho-

470 ERM proteins are localized to peri-synaptic astrocyte processes in ALS patient brains and
471 mouse models[74]. Future research exploring the relationships between LRRK2, ERM,
472 and autophagy in astrocytes will help clarify these processes and their impact on brain
473 region-specific excitatory and inhibitory synapse phenotypes.

474 **Implications for Therapeutic Development**

475 LRRK2 G2019S$^{ki/ki}$ mice do not recapitulate motor symptoms of PD because there
476 is no detectable dopaminergic neuron loss in these mice[41, 75]. However, these mice
477 may serve as good models for the non-motor (prodromal) PD symptoms seen in LRRK2
478 G2019S carriers[76]. These non-motor symptoms, which arise long before motor
479 dysfunction in PD, indicate aberrant synaptic connectivity within multiple brain circuits,
480 including the cortex, long before the death of dopaminergic neurons[77]. LRRK2
481 G2019S$^{ki/ki}$ mice display early circuit dysfunction and non-motor symptoms akin to
482 prodromal PD. Previous studies showed that LRRK2 G2019S$^{ki/ki}$ mice have deficits in
483 attention and goal-directed learning and differential response to stress[34, 78, 79]. Our
484 findings showing synaptic deficits in the ACC of LRRK2 G2019S$^{ki/ki}$ mice (Figure 2-3) fit
485 well with these studies because the ACC is a brain region that controls attention, goal-
486 directed actions, and mood[80, 81]. Furthermore, we observed synaptic deficits in the
487 ACC of LRRK2 G2019S$^{ki/ki}$ mice concurrently with astrocyte morphological deficits
488 located in the ACC and MOp.

489 Why do ERM phosphorylation and synaptic deficits happen in specific brain
490 regions of LRRK2 G2019S$^{ki/ki}$ mice? Cortical astrocytes are heterogeneous in their gene
491 expression, morphology, and function[82, 83]. Interestingly, cortical astrocyte
492 heterogeneity is controlled by layer-specific neuron heterogeneity[82, 83]. It is plausible

493 that neurons and astrocytes in different cortical regions have varying levels of LRRK2 and
494 diverse susceptibilities to LRRK2 mutations. The ACC and MOp may highly depend on
495 the LRRK2-ERM pathway to maintain synaptic integrity and astrocyte function. A recent
496 single-nucleus RNA sequencing in the striatum revealed that the differential expression
497 level of LRRK2 is correlated with changes in the ciliogenesis of different cholinergic
498 neurons[84], suggesting that LRRK2 transcriptional states influence cell function in a cell-
499 type-specific manner. Future studies investigating the impacts of LRRK2 G2019S on
500 cortical neurons and astrocytes' transcriptional profiles may help explain why specific
501 brain regions and astrocyte populations are susceptible to the LRRK2 G2019S mutation.

502 In sum, our findings reveal that LRRK2 G2019S mutation-mediated ERM
503 hyperphosphorylation in astrocytes causes morphological dysfunction in cortical
504 astrocytes. Our results suggest that this astrocytic dysfunction could directly contribute to
505 excitatory synaptic deficits observed in the ACC of the LRRK2 G2019S mice. Restoring
506 astrocyte function by inhibiting ERM hyperphosphorylation, even post-development, was
507 sufficient to rectify excitatory synaptic pathology. Future studies aiming to identify the
508 molecular mechanisms by which LRRK2 controls ERM phosphorylation and the specific
509 phosphatases involved could lead to new therapeutic targets for PD.

510 **Limitations of the study**

511 In our study, we found that a subset of astrocytes in the ACC and MOp were
512 responsive to LRRK2 kinase activity. We also pinpoint that the balance of ERM
513 phosphorylation plays a crucial role in regulating astrocyte morphology in the ACC and
514 MOp. However, astrocytes display molecular, morphological, and functional

515 heterogeneities[85]. We do not yet know why these astrocytes in the ACC and MOp would
516 be sensitive to LRRK2 kinase activity and how these astrocytes are unique compared to
517 other astrocytes in terms of their transcriptional and proteomic profiles. Another future
518 direction would be to determine how the ERM phosphorylation balance modulates
519 astrocyte morphological changes and synapse changes. ERM is a crucial player in linking
520 F-actin to the cell membrane and is important for regulating membrane tension. Actin
521 cytoskeleton dynamics are important for astrocyte morphogenesis[86]. Future single-cell
522 multi-omics studies and experiments understanding how ERM phosphorylation alters
523 actin cytoskeleton dynamics in astrocytes will help us address these current limitations.
524 In addition, the difference in GFAP levels between human PD patients and LRRK2
525 G2019S$^{ki/ki}$ mice reflects the complexity of human PD pathology, the limitations of single-
526 gene mouse models, and potential species-specific differences in astrocyte reactivity.
527 This discrepancy highlights the challenges in modeling human neurodegenerative
528 diseases in animal models and underscores the need for caution when translating
529 findings from animal studies to human disease. Furthermore, in our study, we used PALE
530 to label astrocytes. While PALE is a powerful tool that allows us to label a sparse
531 population of astrocytes in the brain and study their morphological complexity in detail, it
532 has limitations in labeling astrocytes in deep brain regions like the striatum and substantia
533 pars compacta. Future studies using systemic approaches may overcome this technical
534 limitation and clarify whether and how LRRK2 G2019S affects astrocyte morphology and
535 function in additional brain regions.

536 **FIGURE LEGENDS**

537 **Figure 1: ERM phosphorylation is impaired in PD patients carrying LRRK2 G2019S**
538 **mutation.** (A) Schematic of human frontal cortex regions analyzed for phospho-ERM
539 staining. (B) Representative confocal images of GFAP (green) and phospho-ERM (purple)
540 in the frontal cortex of human controls (n = 4; 3M, 1F) and LRRK2 G2019S mutation
541 carriers (n = 3; 2M, 1F), aged >80 years. Scale bar, 200 µm. (C) Quantification of GFAP
542 integrated density in (B). GFAP: t (5) = 2.822, p = 0.037; phospho-ERM: t (5) = 5.695, p
543 = 0.0023. Grey dots: individual images; black dots: control averages; blue dots: mutation
544 carrier averages. (D) Schematic of mouse anterior cingulate cortex (ACC) and primary
545 motor cortex (MOp) analyzed for phospho-ERM staining. (E-F) Representative confocal
546 images of phospho-ERM in the ACC and the MOp of WT or LRRK2 G2019S$^{ki/ki}$ Aldh1L1-
547 eGFP mice at P21. Scale bar, 10 µm. (G-H) Representative confocal images of phospho-
548 ERM in the ACC and MOp of WT (n = 4; 2M, 2F) or LRRK2 G2019S$^{ki/ki}$ Aldh1L1-eGFP
549 mice (n = 4; 2M, 2F) at P21. Scale bar, 200 µm. (I) Quantification of phospho-ERM
550 integrated density in (G-H). For the ACC, nested t-test, unpaired two-tailed t-test. t (6) =
551 4.247, p = 0.0054. For the MOp, nested t-test, unpaired two-tailed t-test. t (6) = 2.392, p
552 = 0.0536. (J-K) Representative confocal images of phospho-ERM (purple) in the ACC
553 and MOp of WT (n = 4; 2M, 2F) or LRRK2 G2019S$^{ki/ki}$ Aldh1L1-eGFP (n = 4; 2M, 2F) mice
554 at P84. Scale bar, 200 µm. (L) Quantification of phospho-ERM integrated density in (J-K),
555 For the ACC, nested t-test, unpaired Two-tailed t-test. t (6) = 4.383, p = 0.0047. For the
556 MOp, nested t-test, unpaired Two-tailed t-test. t (6) = 3.898, p = 0.0080. Grey dots:
557 individual images; black dots: WT averages; blue dots: mutant averages.

558 **Figure 2: LRRK2 G2019S affects excitatory and inhibitory synapse densities in the**
559 **ACC and MOp.** (A-B) Schematics of analyzed brain regions (ACC and MOp) and
560 methods for quantifying VGluT1-PSD95 and VGAT-GEPHYRIN colocalized puncta. (C)
561 Representative images of VGluT1-PSD95 staining in ventral ACC L1 of WT and LRRK2
562 G2019S$^{ki/ki}$ mice at P84. Scale bar, 10 μm. (D) Quantification of VGluT1-PSD95 puncta
563 in ventral ACC L1 and L2-3, normalized to WT means. n = 5/group (3M, 2F). Nested One-
564 way ANOVA: [$F(3, 56) = 12.48$, $p < 0.0001$]. Bonferroni's test: L1 ($p < 0.0001$), L2-3 ($p =$
565 0.0002). (E) Representative images of VGluT1-PSD95 staining in MOp L1 at P84. Scale
566 bar, 10 μm. (F) Quantification of VGluT1-PSD95 puncta in MOp L1 and L2-3. n = 5/group
567 (3M, 2F). No significant differences (Bonferroni's test: $p > 0.05$). (G) Representative
568 images of VGAT-GEPHYRIN staining in ventral ACC L1. Scale bar, 10 μm. (H)
569 Quantification of VGAT-GEPHYRIN puncta in ACC L1 and L2-3, normalized to WT means.
570 n = 4/group (2M, 2F). No significant differences (Bonferroni's test: $p > 0.05$). (I)
571 Representative images of VGAT-GEPHYRIN staining in MOp L1. Scale bar, 10 μm. (J)
572 Quantification of VGAT-GEPHYRIN puncta in MOp L1 and L2-3. n = 6/group (3M, 3F).
573 Nested One-way ANOVA: [$F(3, 68) = 25.88$, $p < 0.0001$]. Bonferroni's test: L1 ($p < 0.0001$),
574 L2-3 ($p < 0.0001$). Grey dots: individual images; black dots: WT averages; blue dots:
575 mutant averages.

576 **Figure 3: LRRK2 G2019S affects excitatory and inhibitory synapse function in the**
577 **ACC and MOp.** (A) Representative mEPSC traces from ventral ACC L2-3 pyramidal
578 neurons in WT and LRRK2 G2019S$^{ki/ki}$ mice. (B) Cumulative probability and quantification
579 of mEPSC frequency: n = 15 (WT), 13 (LRRK2 G2019S$^{ki/ki}$) neurons, 4 mice/genotype.
580 Kolmogorov-Smirnov test: $D = 0.504$, $p < 0.001$. Mean frequency: WT (2.878 ± 0.6355),

581 LRRK2 G2019S$^{ki/ki}$ (0.9673 ± 0.2328). Unpaired t-test: t (6) = 2.823, p = 0.0302. (C)
582 Cumulative probability and quantification of mEPSC amplitude: n = 14 (WT), 12 (LRRK2
583 G2019S$^{ki/ki}$) neurons. Kolmogorov-Smirnov test: D = 0.194, p < 0.0001. Mean amplitude:
584 WT (15.5 ± 0.6325), LRRK2 G2019S$^{ki/ki}$ (13.9 ± 0.9017). Unpaired t-test: t (6) = 1.451, p
585 = 0.197. (D) Representative mIPSC traces from MOp L2-3 pyramidal neurons in WT and
586 LRRK2 G2019S$^{ki/ki}$ mice. (E) Cumulative probability and quantification of mIPSC
587 frequency: n = 12 (WT), 11 (LRRK2 G2019S$^{ki/ki}$) neurons, 4 WT, 3 LRRK2 G2019S$^{ki/ki}$
588 mice. Kolmogorov-Smirnov test: D = 0.424, p < 0.0001. Mean frequency: WT (0.7788 ±
589 0.1012), LRRK2 G2019S$^{ki/ki}$ (1.301 ± 0.07291). Unpaired t-test: t (5) = 3.883, p = 0.0116.
590 (F) Cumulative probability and quantification of mIPSC amplitude: n = 12 (WT), 11
591 (LRRK2 G2019S$^{ki/ki}$) neurons. Kolmogorov-Smirnov test: D = 0.382, p < 0.0001. Mean
592 amplitude: WT (8.633 ± 0.4883), LRRK2 G2019S$^{ki/ki}$ (9.834 ± 0.5558). Unpaired t-test: t
593 (5) = 1.62, p = 0.1662. Data are presented as mean ± s.e.m.

594 **Figure 4: Overexpression of phospho-dead Ezrin in adult LRRK2 G2019S$^{ki/ki}$**
595 **astrocytes restores excitatory synapse number and function in the ventral ACC.** (A)
596 Representative ventral ACC images of WT and LRRK2 G2019S$^{ki/ki}$ mice injected with
597 AAV-HA-WT or Phospho-dead EZRIN, stained for HA and phospho-ERM (P84). Scale
598 bar, 200 µm. (B) Quantification of phospho-ERM intensity (n = 6/group, 3 males, 3
599 females). One-way ANOVA [F(3, 20) = 31.62, p < 0.0001], Bonferroni's test: significant
600 differences between WT + WT EZRIN vs. LRRK2 + WT EZRIN (p < 0.0001), and LRRK2
601 + WT EZRIN vs. LRRK2 + Phospho-dead EZRIN (p < 0.0001). No significant differences
602 for other comparisons (p > 0.05). (C-D) Representative ACC L1 and L2-3 images of
603 VGluT1/PSD95 staining (P84). Scale bar, 10 µm. Quantification of co-localized puncta

604 normalized to WT + WT EZRIN (n = 5–6/group). L1: One-way ANOVA [F(3, 19) = 5.882,
605 p = 0.0051], Bonferroni's test: significant differences among WT + WT EZRIN, LRRK2 +
606 WT EZRIN, and their Phospho-dead counterparts (p < 0.05). L2-3: One-way ANOVA [F(3,
607 18) = 10.45, p = 0.0003], Bonferroni's test: significant group differences (p < 0.05). (E)
608 Representative mEPSC traces from L2-3 pyramidal neurons. (F) Synaptic event
609 frequency quantification (n = 11–15 neurons from 4 mice/group). Kruskal-Wallis test [H(3)
610 = 36.83, p < 0.0001], Dunn's posthoc: significant differences between WT + WT EZRIN
611 vs. all other groups (p < 0.0001), except LRRK2 + Phospho-dead EZRIN (p > 0.9999).
612 (G) Synaptic event amplitude (n = 11–15 neurons from 4 mice/group). Kruskal-Wallis test
613 [H(3) = 7.051, p = 0.0703]; no significant differences across groups (p > 0.05). Data are
614 mean ± s.e.m. Data are mean ± s.e.m.

615 **Figure 5: Astrocytic LRRK2 controls astrocyte morphology by balancing ERM**
616 **phosphorylation levels *in vivo*.** (A) Representative images of ACC and MOp L2-3
617 astrocytes in WT and LRRK2 G2019S$^{ki/ki}$ (P21) expressing PB-mCherry-CAAX ±
618 Phospho-dead EZRIN. Astrocyte territory in cyan. Scale bar, 10 µm. (B) Astrocyte territory
619 volume (n = 16–18 astrocytes, 6 mice/group). One-way ANOVA [F(3, 20) = 7.987, p =
620 0.0011] with Bonferroni's test showed significant differences: WT vs. LRRK2 G2019S$^{ki/ki}$
621 (p = 0.0178), WT vs. WT + Phospho-dead EZRIN O/E (p = 0.0037), and WT + Phospho-
622 dead EZRIN O/E vs. LRRK2 G2019S$^{ki/ki}$ + Phospho-mimetic EZRIN O/E (p = 0.0165);
623 other comparisons were not significant (p > 0.05). (C) Astrocyte branching complexity. n
624 = 16–18 astrocytes (6 mice per group). Two-way ANOVA showed main effects of
625 condition [F(2.505, 3305) = 158.4, p < 0.0001], radius [F(88, 1602) = 218.5, p < 0.0001],
626 and their interaction [F(264, 3958) = 10.62, p < 0.0001]. Bonferroni's test identified

627 significant differences between groups (all $p < 0.0001$), except WT vs. LRRK2 G2019S$^{ki/ki}$
628 + Phospho-dead EZRIN O/E ($p = 0.5469$). (D) Proposed model of Ezrin conformational
629 transition and LRRK2 regulation in astrocyte morphogenesis. (E) Images of ACC and
630 MOp L2-3 astrocytes expressing shControl-mCherry-CAAX or shLRRK2-mCherry-CAAX
631 ± Phospho-mimetic EZRIN. Scale bar, 10 µm. (F) Astrocyte territory volume. n = 18–22
632 astrocytes (5–6 mice/group). One-way ANOVA [$F(3, 19) = 5.47$, $p = 0.0070$] with
633 Bonferroni's test showed significant differences between shControl and shLRRK2 ($p =$
634 0.0132), and shLRRK2 vs. shLRRK2 + Phospho-mimetic EZRIN O/E ($p = 0.0152$); no
635 other comparisons were significant ($p > 0.05$). (G) Astrocyte branching complexity. n =
636 16–22 astrocytes. Two-way ANOVA revealed significant main effects of condition
637 [$F(2.435, 7008) = 225.0$, $p < 0.0001$], radius [$F(88, 8633) = 325.4$, $p < 0.0001$], and their
638 interaction [$F(264, 8633) = 5.908$, $p < 0.0001$]. Bonferroni's test identified significant
639 differences between most groups (all $p < 0.0001$) except shControl vs. shControl +
640 Phospho-mimetic EZRIN O/E ($p > 0.9999$). Data are mean ± s.e.m.

641 **Figure 6: LRRK2 G2019S alters the interactome of astrocytic Ezrin *in vivo*.** (A)
642 astrocyte-specific AAVs (serotype PHP.eB) were used to express Ezrin or nonspecific
643 cytosolic control. NES, nuclear export sequence; ITR, inverted terminal repeats;
644 GfaABC1D truncated GFAP promoter; HA, hemagglutinin tag; pA, polyadenylation. (B)
645 outline of the experimental paradigm. n = 3 biological replicates/construct/genotype (1
646 replicate = 2 animals per pooled sample). (C) Volcano plot showing the differential
647 abundance of proteins detected by Astro-EZRIN-BioID in WT and LRRK2 G2019S$^{ki/ki}$
648 cortices. (D-E) Bars show the top 10 most significant Gene Ontology (GO) terms, ordered
649 by lowest adjusted p-value, for the proteins differentially detected by Astro-EZRIN-BioID

650 in WT compared to LRRK2 G2019S$^{ki/ki}$ (D) Molecular function (E) Biological Process. (F)
651 The interaction network depicts 58 high-confidence proteins that gained or lost proximity
652 to Ezrin in LRRK2 G2019S$^{ki/ki}$ compared to WT mice. (G-H) heatmaps depict fold-change
653 in abundance (Astro-EZRIN-BioID / Asto-Cyto-BioID) of proteins with high confidence
654 changed proximity to Ezrin in LRRK2 G2019S$^{ki/ki}$ astrocytes.

655 **Figure 7: Interaction Between Atg7 and Ezrin Depends on Ezrin's Phosphorylation**
656 **State.** (A) Schematic of Atg7 domains. (B) Predicted Atg7 homodimer model. (C)
657 Schematic of Ezrin domains. (D) Predicted Ezrin structures in closed and open
658 conformations. (E) Predicted Atg7-Ezrin interaction. (F) Structural changes in Ezrin and
659 Atg7 upon binding. (G) Co-immunoprecipitation of Ezrin-HA by Atg7-Myc in HEK293T
660 cells expressing WT, phospho-dead, or phospho-mimetic Ezrin. Ezrin was detected with
661 anti-HA and Atg7 was detected with anti-Myc. (H) Quantification of (G). One-way ANOVA
662 [$F(2,6) = 9.932$, $p = 0.0125$] with Tukey's test: WT vs. phospho-mimetic Ezrin ($p = 0.0151$),
663 phospho-dead vs. phospho-mimetic Ezrin ($p = 0.0272$), WT vs. phospho-dead Ezrin ($p =$
664 0.8658). n = 3 experiments. (I) Images of ACC and MOp L2-3 astrocytes at P21
665 expressing shControl or shAtg7-PB-mCherry-CAAX. Scale bar, 10 µm. (J) Quantification
666 of astrocyte territories. Nested ANOVA [$F(3,28) = 9.484$, $p = 0.0002$] with Bonferroni tests:
667 WT shControl vs. LRRK2 G2019S$^{ki/ki}$ shControl ($p = 0.0036$), WT shControl vs. WT
668 shAtg7 ($p = 0.0003$), WT shAtg7 vs. LRRK2 G2019S$^{ki/ki}$ shAtg7 ($p = 0.0109$). n = 20–25
669 cells from 4–5 mice/group. (K) Astrocyte branching complexity. Two-way ANOVA
670 revealed significant condition [$F(2.324, 472.6) = 43.1$, $p < 0.05$], radius [$F(9, 250) = 301.8$,
671 $p < 0.05$], and interaction effects [$F(27, 610) = 4.539$, $p < 0.05$]. Bonferroni tests showed

672 significant differences between groups, including WT shControl vs. LRRK2 G2019S$^{ki/ki}$

673 shControl ($p < 0.0001$) and WT shControl vs. WT shAtg7 ($p < 0.0001$).

674 **MATERIALS AND METHODS**

675 **KEY RESOURCES TABLE**

REAGENT or RESOURCE	SOURCE	IDENTIFIER
β-actin	Sigma-Aldrich	Cat# A5441, RRID: AB_476744
ERM	Cell Signaling	Cat# 3142, RRID:AB_2100313
GAPDH	Abcam	Cat# ab8245, RRID:AB_2107448
Gephyrin	Synaptic Systems	Cat# 147 011, RRID:AB_887717
GFAP	Agilent	Cat# Z0334, RRID:AB_10013382
GFAP	Millipore	Cat# AB5541, RRID:AB_177521
GFP	Aves labs	GFP-1020, RRID:AB_10000240
HA	Roche	Cat# 11867423001, RRID:AB_390918
L1 (ASCS4)	DSHB	Cat# ascs4, RRID:AB_528349
LRRK2	Abcam	Cat# ab133474, RRID:AB_2713963
phospho-ERM	Cell Signaling	Cat# 3141, RRID:AB_330232
phospho-ERM	Cell Signaling	Cat# 3726, RRID: AB_10560513
phospho-Rab10	Abcam	Cat# ab230261, RRID:AB_2811274
PSD-95	Innovative Research	Cat# 51-6900, RRID: AB_87705
Sox9	Millipore	Cat# AB5535, RRID:AB_2239761
VGAT	Synaptic Systems	Cat# 131 004, RRID: AB_887873
VGluT1	Synaptic Systems	Cat# 135304, RRID: AB_887878
S100β	Millipore Sigma	Cat# S2532, RRID: AB_477499
Iba1	Synaptic Systems	Cat# 234009, RRID: AB_2891282
MAP2	Thermo Fisher Scientific	Cat# 13-1500, RRID:AB_2533001
Lambda protein phosphatase	New England Biolabs	Cat# P0753L
Bacterial and virus strains		
One Shot STBL3	Thermo Fisher	Cat# C737303
AAV PhP.eB	This paper	N/A
Chemicals, peptides, and recombinant proteins		

AraC	Sigma	Cat# C1768
B27	GIBCO	Cat# 17504044
B27 Plus	GIBCO	Cat# A3582801
BDNF	PeproTech	Cat# 450-02
Carboxypeptidase E	R&D	Cat# 3587-ZN
CNTF	PeproTech	Cat# 450-13
DMEM	GIBCO	Cat# 11960
DPBS	GIBCO	Cat# 14287
Dystroglycan	R&D	Cat# 6868-DG
Fetal Bovine Serum	Thermo Fisher	Cat# 10-437-028
Forskolin	Sigma	Cat# F6886
Glycerol	Acros Organics	Cat# AC158920010
L-Glutamine	GIBCO	Cat# 25030-081
Hydrocortisone	Sigma	Cat# H0888-5G
Insulin	Sigma	Cat# I1882
Neurobasal	GIBCO	Cat# 21103049
Neurobasal Plus	GIBCO	Cat# A3582901
Odyssey Blocking Buffer	LI-COR Biosciences	Cat# 927-40000
Opti-MEM	Thermo Fisher	Cat# 11058021
Paraformaldehyde	Electron microscopy Sciences	Cat# 19210
Pen/Strep	GIBCO	Cat# 15140
PhosSTOP™	Roche	Cat# 4906845001
Poly-D-Lysine	Sigma	Cat# P6407
Protease Inhibitor Cocktail	Roche	Cat# 4693132001
RIPA Buffer	Sigma	Cat# R0278
Sodium Pyruvate	GIBCO	Cat# 11360-070
Tissue-Tek® O.C.T. Compound	Sakura® Finetek	Cat# 4583
Triton X-100	Roche	Cat# 11332481001
Critical commercial assays		
Endo-Free Maxi Prep Kit	QIAGEN	Cat# 12362
Experimental models: cell lines		
HEK293T	ATCC	Cat# CRL-11268, RRID:CVCL_1926

Rat primary cortical neurons	This paper	N/A
Rat primary cortical astrocytes	This paper	N/A
Experimental models: organisms/strains		
Mouse: Aldh1L1-EGFP	MMRRC	RRID: MMRRC_011015-UCD
Mouse: CD1	Charles River	RRID: IMSR_CRL:022
Mouse: LRRK2 G2019S$^{ki/ki}$	Taconic	RRID: IMSR_TAC:13940
Rat: Sprague-Dawley	Charles River	Cat# 001, RRID:IMSR_CRL:400
Recombinant DNA		
pZac2.1-GfaABC1D-Ezrin WT-BioID2-HA	This paper	RRID:Addgene_227681
pZac2.1-GfaABC1D-Ezrin T567D-BioID2-HA	This paper	RRID:Addgene_227682
pZac2.1-GfaABC1D-Ezrin T567A-BioID2-HA plasmid	This paper	RRID:Addgene_227683
pLKO.1-sh*Atg7*-EGFP	This paper	RRID:Addgene_227684
pLKO.1-shControl-EGFP	This paper	RRID:Addgene_227685
pPB-CAG-sh*LRRK2*-mCherry-CAAX	This paper	RRID:Addgene_227686
pPB-CAG-sh*Atg7*-mCherry-CAAX	This paper	RRID:Addgene_227687
pPB-CAG-shControl-mCherry-CAAX	This paper	RRID:Addgene_227689
Software and algorithms		
GraphPad Prism 9	GraphPAD	https://www.graphpad.com/scientific-software/prism/, RRID:SCR_002798
ImageJ	NIH	https://imagej.nih.gov/ij/, RRID:SCR_003070
Puncta Analyzer	Savage et al., 2024[87]	https://github.com/Eroglu-Lab/Syn_Bot, RRID:SCR_025425
Minhee Analysis	Kim et al., 2021[88]	https://github.com/parkgilbong/Minhee_Analysis_Pack; RRID:SCR_021250

In vitro Sholl analysis	Tan et al., 2023[89]	https://github.com/Eroglu-Lab/In-Vitro-Sholl, RRID:SCR_015795
CABS-Flex	CABS-Flex	https://biocomp.chem.uw.edu.pl/CABSflex2, RRID:SCR_025674
PyMol	PyMol	http://www.pymol.org/, RRID:SCR_000305
Imaris	Imaris	http://www.bitplane.com/imaris/imaris, RRID:SCR_007370
Simple Western Compass	Bio-techne	https://www.bio-techne.com/resources/instrument-software-download-center/compass-software-simple-western, RRID:SCR_022930
Alphafold	Alphafold	https://github.com/google-deepmind/alphafold, RRID:SCR_025454
AMBER	AMBER	https://github.com/CAMI-challenge/AMBER, RRID:SCR_016151
Proteome Discoverer	Thermofisher	https://www.thermofisher.com/order/catalog/product/IQLAAEGABSFAKJMAUH, RRID:SCR_014477
Cytoscape	Cytoscape	http://cytoscape.org, RRID:SCR_003032
ClusterProfiler	ClusterProfiler	http://bioconductor.org/packages/release/bioc/html/clusterProfiler.html, RRID:SCR_016884
R	R Project for Statistical Computing	https://www.r-project.org/, RRID:SCR_001905
Gene Ontology (GO)	Gene Ontology	http://www.geneontology.org/, RRID:SCR_002811
Image Studio	LICOR	https://www.licor.com, RRID:SCR_015795

RESOURCE AVAILABILITY

Lead contact

679 Further information and requests for resources and reagents should be directed to and
680 will be fulfilled by the lead contacts, Shiyi Wang (shiyi.wang@duke.edu) and Cagla Eroglu
681 (cagla.eroglu@duke.edu).

682 **Materials availability**

683 The reagents generated in this study are available without restriction.

684 **Data availability**

685 The data generated during this study are available at the link
686 https://zenodo.org/records/15282825.

687 The proteomic data is uploaded to the repository ProteomeXchange via the PRIDE
688 database (https://www.ebi.ac.uk/pride/), project accession number: PXD062312.

689 **Code availability**

690 The code used to analyze Sholl data is available via the link https://github.com/Eroglu-
691 Lab/Sholl_Macro.

692 **Protocol availability**

693 The protocols used for this study are available at the link
694 https://www.protocols.io/researchers/shiyi-wang1/publications

695

696 **EXPERIMENTAL MODELS AND SUBJECT DETAILS**

697 **Animals**

698 All mice and rats were used in accordance with the Institutional Animal Care and Use
699 Committee (IACUC) and the Duke Division of Laboratory Animal Resources (DLAR)
700 oversight (IACUC Protocol Numbers A147-17-06 and A117-20-05). All mice and rats were

701 housed under typical day/night conditions of 12-hour cycles. LRRK2 G2019S$^{ki/ki}$ mice
702 (RRID: IMSR_TAC:13940) were obtained through Taconic. This model was generated on
703 the C57BL6/NTac background. It has been maintained on that pure background in
704 Taconic. Aldh1l1-EGFP (RRID: MMRRC_011015-UCD) mice were obtained through
705 MMRRC and backcrossed on a C57BL/6J background. Wild-type CD1 mice used for
706 PALE were purchased through Charles River Laboratories (RRID: IMSR_CRL:022).

707 Mice and rats were used for experiments as specified in the text and figure legends.
708 For all experiments, age, and sex-matched mice were randomly assigned to experimental
709 groups based on genotypes. Mice of both sexes were included in the analysis, and we
710 did not observe any influence or association of sex on the experimental outcomes.

711 **Primary cortical neuron isolation and culture**

712 Purified (glia-free) rat cortical neurons were prepared as described previously[36]. Briefly,
713 cortices from P1 rat pups of both sexes (Sprague Dawley, Charles River Laboratories,
714 SD-001) were micro-dissected, digested in papain (~7.5 units/ml) at 33°C for 45 minutes,
715 triturated in low and high ovomucoid solutions, resuspended in panning buffer (DPBS
716 (GIBCO 14287) supplemented with BSA and insulin) and passed through a 20 μm mesh
717 filter (Elko Filtering 03-20/14). Filtered cells were incubated on negative panning dishes
718 coated with Bandeiraea Simplicifolia Lectin 1 (x2), followed by goat anti-mouse IgG+IgM
719 (H+L) (Jackson ImmunoResearch 115-005-044), and goat anti-rat IgG+IgM (H+L)
720 (Jackson ImmunoResearch 112-005-044) antibodies, then incubated on positive panning
721 dishes coated with mouse anti-L1 (ASCS4, Developmental Studies Hybridoma Bank,
722 Univ. Iowa) to bind cortical neurons. Adherent cells were collected by forceful pipetting
723 with a P1000 pipette. Isolated neurons were pelleted (11 minutes at 200 g) and

724 resuspended in serum-free neuron growth media (NGM; Neurobasal, B27 supplement,
725 2 mM L-Glutamine, 100 U/ml Pen/Strep, 1 mM sodium pyruvate, 4.2 µg/ml Forskolin,
726 50 ng/mL BDNF, and 10 ng/mL CNTF). 70,000 neurons were plated onto 12 mm glass
727 coverslips coated with 10 µg/ml poly-D-lysine (PDL, Sigma P6407) and
728 2 µg/ml laminin and incubated at 37°C in 10% CO_2. On day *in-vitro* (DIV) 2, half of the
729 media was replaced with NGM Plus (Neurobasal Plus, B27 Plus, 100 U/mL Pen/Strep,
730 1 mM sodium pyruvate, 4.2 µg/ml Forskolin, 50 ng/ml, BDNF, and 10 ng/ml CNTF) and
731 AraC (10 µM) was added to stop the growth of proliferating contaminating cells. On DIV
732 3, all the media was replaced with NGM Plus. In experiments involving lentivirus infection,
733 100 µl of supernatant containing lentivirus plus polybrene (1 µg/ml) was added to the
734 AraC NGM mixture on DIV 2 and completely washed out on DIV 3 and replaced with NGM
735 Plus containing 100 ng/ml BDNF. Neurons were fed on DIV 6 and DIV 9 by replacing half
736 of the media with NGM Plus.

737 **Primary cortical astrocyte isolation and culture**

738 **Rat astrocyte isolation and culture**

739 Rat cortical astrocytes were prepared as described previously[36]. P1 rat cortices from
740 both sexes were micro-dissected, papain digested, triturated in low and high ovomucoid
741 solutions, and resuspended in astrocyte growth media (AGM: DMEM (GIBCO 11960), 10%
742 FBS, 10 µM, hydrocortisone, 100 U/ml Pen/Strep, 2 mM L-Glutamine, 5 µg/ml Insulin,
743 1 mM Na Pyruvate, 5 µg/ml N-Acetyl-L-cysteine). Between 15-20 million cells were plated
744 on 75 mm^2 flasks (non-ventilated cap) coated with poly-D-lysine and incubated at 37°C
745 in 10% CO_2. On DIV 3, the removal of non-astrocyte cells was performed by forcefully
746 shaking closed flasks by hand for 10-15 s until only an adherent monolayer of astrocytes

747 remained. AraC was added to the media from DIV 5 to DIV 7 to eliminate contaminating
748 fibroblasts. On DIV 7, astrocytes were trypsinized (0.05% Trypsin-EDTA) and plated into
749 12-well or 6-well dishes. On DIV 8, cultured rat astrocytes were transfected
750 with shRNA and/or expression plasmids using Lipofectamine LTX with Plus Reagent
751 (Thermo Scientific) per the manufacturer's protocol. Briefly, 1 µg (12-well) or 2 µg (6-well)
752 total DNA was diluted in Opti-MEM containing Plus Reagent, mixed with Opti-MEM
753 containing LTX (1:2 DNA to LTX), and incubated for 30 minutes. The transfection solution
754 was added to astrocyte cultures and incubated at 37°C for 3 hours. On DIV 10, astrocytes
755 were trypsinized, resuspended in NGM plus, plated (20,000 cells per well) onto DIV 10
756 neurons, and co-cultured for 48 hours.

757 **shRNA plasmids**

758 pLKO.1 Puro plasmids containing shRNA (pLKO.1-shRNA) against mouse/rat *Lrrk2*
759 (sh*LRRK2*: TRCN0000322193; GGCCGAGTTGTGGATCATATT) and mouse/rat *Atg7*
760 (sh*Atg7*: TRCN0000092163; TATTATTGAGTTCAGAGCTGG), were obtained from the
761 RNAi Consortium (TRC) via Dharmacon. Two scrambled shRNA sequences were
762 generated (GTTGCTGAATGGCGGATCTAT; GTTGCGGTTATGAATAGTACT) and
763 cloned into the pLKO.1 TRC cloning vector[90] according to Addgene protocols
764 (https://www.addgene.org/protocols/plko/). To generate pLKO.1 shRNA plasmids that
765 express EGFP (pLKO.1-shRNA-EGFP), CAG-EGFP was removed from pLenLox-shNL1-
766 CAG-EGFP[91] and inserted between Kpn1 and SpeI sites in pLKO.1 Puro, replacing
767 the puromycin resistance gene. pLKO.1 shRNA mCherry plasmids were generated by
768 replacing EGFP with mCherry between KpnI and NheI sites.

769 **PiggyBac plasmids**

770 pPB-CAG-EGFP (RRID:Addgene_40973) and pGLAST-PBase were a gift from Dr.
771 Joseph Loturco[92]. To generate pPB-CAG-mCherry-CAAX, mCherry-CAAX was
772 inserted between XmaI and NotI restrictions sites to replace EGFP. To insert the hU6
773 promoter and shRNA in pPB-CAG-mCherry-CAAX, a DNA fragment containing hU6 and
774 shRNA was amplified from pLKO.1-shRNA using Phusion High-Fidelity DNA
775 Polymerase (NEB) with primers that introduced SpeI restriction sites (Forward Primer:
776 GGACTAGTCAGGCCCGAAGGAATAGAAG; Reverse Primer:
777 GGACTAGTGCCAAAGTGGATCTCTGCTG). PCR products were purified, digested with
778 SpeI, and ligated into pPB-CAG-mCherry-CAAX at the SpeI restriction site. An analytical
779 digest with EcoRI followed by sequencing was used to confirm the orientation of the
780 inserted DNA fragment.

781 **Ezrin plasmids**

782 pZac2.1-GfaABC1D-Lck-GCaMP6f was a gift from Dr. Baljit Khakh (Addgene plasmid
783 #52924, RRID:Addgene_52924). pZac2.1-GfaABC1D-BioID2-HA was generated by PCR
784 of BioID2 from pAAV-hSyn-BioID2-Linker-Synapsin1a-HA[93] (primers Fwd: 5'-
785 ctagcctcgagaattcaccatgttcaaaaatcttatttg-3', Rev: 5'-
786 ccgggtcgactctagatgcgtaatccggtacatcg-3') and insertion into the EcoRI and XbaI
787 restriction sites of pZac2.1-GfaABC1D-Lck-GCaMP6f using In-Fusion cloning (TaKaRa).
788 pHJ421(pEGFP-Ezrin WT) and pHJ423 (pEGFP-Ezrin T567D) were a gift from Stephen
789 Shaw (Addgene plasmid # 20680 and # 20681; RRID:Addgene_20680,
790 RRID:Addgene_20681). pZac2.1-GfaABC1D-Ezrin WT-BioID2-HA
791 (RRID:Addgene_227681) and pZac2.1-GfaABC1D-Ezrin T567D-BioID2-HA

792 (RRID:Addgene_227682) were generated by PCR of Ezrin from pHJ421 or pHJ423
793 (primers Fw: 5'-ctagcctcgagaattcaccatgccgaaaccaatca-3', Rv: 5'-
794 tgaacatggtgaattccgacagggcctcgaactcg-3') and insertion into the EcoRI restriction sites of
795 pZac2.1-GfaABC1D-BioID2, respectively. To generate pZac2.1-GfaABC1D-Ezrin
796 T567A-BioID2-HA plasmid, Q5® Site-Directed Mutagenesis Kit (NEB) was used with
797 mutagenesis primers (Fwd: CAAGTACAAGGCGCTGCGGCAGA; Rev:
798 TCCCGGCCTTGCCTCATG)

799 **Lentivirus production and transduction**

800 Lentiviruses containing shRNA targeting vectors were produced to test the knockdown
801 efficiency of shRNA constructs in cultured primary astrocytes or to bulk transduce
802 neurons with shRNA and GFP. To produce lentivirus, HEK293T cells were transfected
803 with a pLKO.1 shRNA Puro targeting plasmid (for astrocyte transduction), an envelope
804 plasmid (VSVG) (RRID:Addgene_12259), and a packaging plasmid (dR8.91) using X-
805 tremeGENE (Roche). One day after transfection, the media was replaced with AGM (for
806 astrocyte transduction), and media containing lentivirus was collected on days 2 and 3
807 post-transfection. To assess the knockdown efficiency of shRNAs in astrocytes, rat
808 primary astrocytes at DIV 7 were plated in 6-well dishes in 2 ml of AGM. On DIV 8, 1 ml
809 of AGM was removed, and 500 µl of fresh AGM was added along with 500 µl of lentivirus-
810 containing media and 1 µg/ml polybrene. Cultured astrocytes were treated with
811 puromycin (1 µg/ml) from DIV 10-15 to select for transduced cells. Cultured astrocytes
812 were lysed at DIV 15 for protein extraction and Western blot analysis.

813 **Immunocytochemistry**

814 Astrocyte-neuron co-cultures on glass coverslips were fixed on DIV 12 with warm 4%
815 PFA for 7 minutes, washed 3 times with PBS, blocked in a blocking buffer containing 50%
816 normal goat serum (NGS) and 0.4% Triton X-100 for 30 minutes, and washed in PBS.
817 Samples were then incubated overnight at 4°C in primary antibodies diluted in blocking
818 buffer containing 10% NGS, washed with PBS, incubated in Alexa Fluor conjugated
819 secondary antibodies (Life Technologies) for 2 hours at room temperature, and washed
820 again in PBS. Coverslips were mounted onto glass slides (VWR Scientific) with
821 Vectashield mounting media containing DAPI (Vector Labs), sealed with nail polish, and
822 imaged on an AxioImager M1 (Zeiss) fluorescence microscope. Images of healthy
823 astrocytes with strong expression of fluorescent markers that did not overlap with other
824 fluorescent astrocytes were acquired at 40x magnification in red, green, and/or DAPI
825 channels using a CCD camera. Astrocyte morphological complexity was analyzed in FIJI
826 using the Sholl analysis plugin[94], as described previously[36]
827 (https://github.com/Eroglu-Lab/In-Vitro-Sholl, RRID: SCR_022758). Statistical analyses
828 were conducted using a custom code in R (https://github.com/Eroglu-Lab/In-Vitro-Sholl,
829 RRID: SCR_022758). A mixed-effect model with multiple comparisons made using the
830 Tukey post-test was used for Sholl analysis to account for the variability per experiment
831 as a random effect to evaluate differences between the conditions. The exact number of
832 independent experiments and the exact number of cells analyzed are indicated in the
833 figure legend for each experiment. To ensure the health of astrocyte-neuron co-cultures,
834 the peak for the number of astrocyte intersections must be greater than or equal to 25 in
835 the control condition. We imaged non-overlapping astrocytes that contained a single

836 nucleus (DAPI stain) and expressed consistent fluorescent markers and Ezrin constructs
837 according to the experimental conditions.

838 **Postnatal astrocyte labeling by electroporation (PALE)**

839 Late P0/early P1 mice were sedated by hypothermia until anesthetized, and 1 µl
840 of plasmid DNA mixed with Fast Green Dye was injected into the lateral ventricle of one
841 hemisphere using a pulled glass pipette (Drummond). For shRNA knockdown
842 experiments in wild-type CD1 mice, the 1 µl of DNA contained 1 µg of pGLAST-PBase
843 and 1 µg of pPB-shRNA-mCherryCAAX was injected. To label astrocytes in WT
844 and LRRK2 G2019S$^{ki/ki}$ mice, the 1 µl of DNA contained 1 µg of pGLAST-PBase and 1
845 µg of pPB-mCherry-CAAX was injected per mouse.

846 For PALE-mediated overexpression of phospho-mimetic Ezrin in shRNA knockdown
847 experiments, 0.5 µg pGLAST-PBase, 0.5 µg pPB-shRNA-mCherryCAAX, and 1 µg
848 pZac2.1-GfaABC1D-Ezrin T567D-BioID2-HA were injected in a total volume of 1 µl. For
849 phospho-dead Ezrin overexpression in WT and LRRK2 G2019S$^{ki/ki}$ mice, 0.5 µg pGLAST-
850 PBase, 0.5 µg of pZac2.1-gfaABC1D-mCherry-CAAX and 1 µg of pZac2.1-GfaABC1D-
851 Ezrin T567A-BioID2-HA were injected in a total volume of 1 µl. Following DNA injection,
852 electrodes were oriented with the positive terminal above the frontal cortex and the
853 negative terminal below the chin, and 5 discrete 50 ms pulses of 100 V spaced 950 ms
854 apart were applied. Pups were recovered on a heating pad, returned to their home cage,
855 and monitored until collection at P21. The number of mice used for each experiment is
856 indicated in the figure legends. All animals appeared healthy at the time of collection.
857 Brain sections were examined for the presence of electroporated cells before staining.

858 **Adeno-associated virus (AAV) production and administration**

859 Purified AAVs were produced as described previously[95]. Briefly, HEK293T cells were
860 transfected with pAd-DELTA F6, serotype plasmid AAV PHP.eB (RRID:
861 Addgene_103005), and AAV plasmid (pZac2.1-GfaABC1D-Ezrin-BioID2-HA;
862 RRID:Addgene_227681 or pZac2.1-GfaABC1D-Ezrin T567A-BioID2-HA;
863 RRID:Addgene_227683). Three days after transfection, cells were collected in 15 mM
864 NaCl, 5 mM Tris-HCl, pH 8.5, and lysed with repeat freeze-thaw cycles followed by
865 treatment with Benzonase (Novagen 70664) at 37°C for 30 minutes. Lysed cells were
866 pelleted by centrifugation, and the supernatant, containing AAVs, was applied to an
867 Optiprep density gradient (Sigma D1556, 15%, 25%, 40%, and 60%) and centrifuged at
868 67,000 rpm using a Beckman Ti-70 rotor for 1 hour. The AAV-enriched fraction was
869 isolated from between 40% and 60% iodixanol solution and concentrated by repeated
870 washes with sterile PBS in an Amicon Ultra-15 filtration unit (NMWL: 100 kDa, Millipore
871 UFC910008) to a final volume of ~100 µl and aliquoted for storage at −80°C. 9-week-old
872 WT or LRRK2 G2019S$^{ki/ki}$ mice placed in a stereotaxic frame were anesthetized through
873 inhalation of 1.5% isofluorane gas. 10 µl of purified AAVs having a titer of ~1 x 10^{12} GC/ml
874 was introduced into the mouse brain intravenously by injection into the retro-orbital sinus.
875 After 3 weeks at 12-week-old, mice were anesthetized with 200 mg/kg Tribromoethanol
876 (Avertin) and transcardially perfused with TBS/Heparin and 4% paraformaldehyde (PFA)
877 at room temperature (RT). Harvested brains were post-fixed overnight in 4% PFA,
878 cryoprotected in 30% sucrose, and the brain blocks were prepared with O.C.T.
879 (TissueTek) to store at −80°C. 30 µm thick brain sections were obtained through

880 cryosectioning using a Leica CM3050S (Leica, Germany) vibratome and stored in a
881 mixture of TBS and glycerol at −20°C for further free-float antibody staining procedures.

882 **Immunohistochemistry on mouse brain sections**

883 Mice used for immunohistochemistry were anesthetized with 200 mg/kg Avertin and
884 perfused with TBS/Heparin and 4% PFA. Brains were collected and post-fixed in 4% PFA
885 overnight, cryoprotected in 30% sucrose, frozen in a solution containing 2 parts 30%
886 sucrose and 1-part O.C.T. (TissueTek), and stored at −80°C. Floating coronal tissue
887 sections of 30 µm, 40 µm or 100 µm thickness were collected and stored in a 1:1 mixture
888 of TBS/glycerol at −20°C. For immunostaining, sections were washed in 1x TBS
889 containing 0.2% Triton X-100 (TBST), blocked in 10% NGS diluted in TBST, and
890 incubated in primary antibody for 2-3 nights at 4°C with gentle shaking. Primary antibodies
891 used were anti-LRRK2 (Rabbit, 1:500; ab133474, Abcam, RRID:AB_2713963), HA (Rat,
892 1:500; 11867423001, Roche, RRID:AB_390918), phospho-ERM (Rabbit, 1:500; 3141,
893 Cell Signaling, RRID:AB_330232), Sox9 (Rabbit, 1:500; AB5535, Millipore Sigma,
894 RRID:AB_2239761), GFAP (Rabbit, 1:500; Z0334, Agilent DAKO, RRID:AB_177521),
895 VGluT1 (Guinea pig, 1:2000; 135304, Synaptic Systems, RRID: AB_887878), PSD95
896 (Rabbit, 1:300; 51-6900, Innovative Research, RRID: AB_87705), VGAT (Guinea pig,
897 1:1000; 131004, Synaptic Systems, RRID: AB_887873), Gephyrin (Rabbit, 1:1000;
898 147011, Synaptic Systems, RRID:AB_887717), S100β (Mouse IgG1, 1:200; S2532,
899 Millipore Sigma, RRID: AB_477499), MAP2 (Mouse IgG1, 1:200; 13-1500, Thermo Fisher
900 Scientific, RRID:AB_2533001), and Iba1 (Chicken, 1:500; 234009, Synaptic Systems,
901 RRID: AB_2891282). For lambda protein phosphatase (λ-PPase) treatment, brain
902 sections were divided into two groups: λ-PPase treatment group and a control group.

903 Brain sections in the treatment group were incubated with λ-PPase at 30°C for 2 hours,
904 while brain sections in the control group were incubated under identical conditions without
905 the enzyme. All sections were blocked in 5% normal goat serum and 0.3% Triton X-100
906 for 1 hour at room temperature, followed by overnight incubation with primary antibodies
907 at 4°C. Following the primary incubation, sections were washed in TBST, incubated in
908 Alexa Fluor conjugated secondary antibodies diluted 1:200 (Life Technologies) for 2-3
909 hours at room temperature, washed with TBST, and mounted onto glass slides using a
910 homemade mounting media (90% Glycerol, 20 mM Tris pH 8.0, 0.5% n-Propyl gallate)
911 and sealed with nail polish. Images were acquired with an Olympus FV 3000 microscope.

912 **Immunohistochemistry on human brain sections**

913 Floating human frontal cortex sections of 40 μm thickness were obtained from Banner
914 Sun Health Research Institute in Sun City, Arizona (4 control and 3 LRRK2 G2019S
915 mutation carrier subjects). None of the control subjects had a history of dementia or
916 neurological or psychiatric disorders at the time of death (See Supplemental Table 1).
917 Informed and written consent was obtained from the donors. For immunostaining,
918 sections were washed in 1x TBS containing 0.3% Triton X-100 (TBST), blocked in 3%
919 NGS diluted in TBST, and incubated in primary antibody 2-3 nights at 4°C with shaking.
920 Primary antibodies used were GFAP (chicken, 1:250; AB5541, Millipore Sigma,
921 RRID:AB_177521), phospho-ERM (Rabbit, 1:250; 3726, Cell Signaling, RRID:
922 AB_10560513), S100β (Mouse IgG1, 1:200; S2532, Millipore Sigma, RRID: AB_477499),
923 and MAP2 (Mouse IgG1, 1:200; 13-1500, Thermo Fisher Scientific, RRID:AB_2533001).
924 Following primary incubation, sections were washed in TBST, incubated in Alexa Fluor
925 conjugated secondary antibodies diluted 1:200 (Life Technologies) for 2-3 hours at room

926 temperature, washed with TBST, and mounted onto glass slides using a homemade
927 mounting media (90% Glycerol, 20 mM Tris pH 8.0, 0.5% n-Propyl gallate) and sealed
928 with nail polish.

929 **Mouse astrocyte territory volume analysis**

930 To assess the territory volume of individual astrocytes in the mouse cortex, 100 µm-thick
931 floating sections containing anterior cingulate cortex (ACC) and primary motor cortex
932 (MOp) astrocytes labeled sparsely via PALE with mCherry-CAAX were collected. High-
933 magnification images containing an entire astrocyte (50-60 µm z-stack) were acquired
934 with an Olympus FV 3000 microscope with the 60x objective. Criteria for data inclusion
935 required that the entirety of the astrocyte could be captured within a single brain section
936 and that the astrocyte was in L2-3 of the ACC or MOp. Astrocytes in which the entire
937 astrocyte could not be captured within the section or was in other layers or outside of the
938 ACC or MOp were not imaged. Imaged astrocytes were analyzed using Imaris Bitplane
939 software (RRID: SCR_007370) as described previously[36]. Briefly, surface
940 reconstructions were generated, and the Imaris Xtensions "Visualize Surface Spots" and
941 "Convex Hull" were used to create an additional surface render representing the territory
942 of the astrocyte. The volume of each territory was recorded, and astrocyte territory sizes
943 from biological replicates were analyzed across experimental conditions using a nested
944 two-way ANOVA followed by the Bonferroni posthoc test. For 3D Sholl analysis of
945 individual PALE astrocytes, we first loaded images onto Imaris and then created a surface.
946 After generating the surface of astrocytes, we created filaments using 'Add new filament
947 (leaf icon)'. For the quantification of complexity, we clicked on the gear tool on Imaris to

948 display Sholl intersections. The number of animals and cells/animals analyzed are
949 specified in the figure legend for each experiment.

950 **Mouse synapse imaging and analysis**

951 Staining, image acquisition, and analysis of synaptic density were performed as described
952 previously[96]. Synaptic staining was performed in coronal sections (30 μm thick)
953 containing the ACC and MOp from WT and LRRK2 G2019S$^{ki/ki}$ mice. To label pre and
954 postsynaptic proteins, the following antibody combinations were used: VGluT1 and
955 PSD95 (excitatory, intracortical), VGAT, and GEPHYRIN (inhibitory). High magnification
956 60x objective plus 1.64x optical zoom z-stack images containing 15 optical sections
957 spaced 0.34 μm apart were obtained using an Olympus FV 3000 inverted confocal
958 microscope. Each z-stack was converted into 5 maximum projection images (MPI), each
959 corresponding to a 1 μm section of z plane, using FIJI. Synapses were identified by the
960 colocalization of pre and postsynaptic puncta. The number of co-localized synaptic puncta
961 of excitatory intracortical (VGluT1-PSD95) and inhibitory (VGAT-GEPHYRIN) synapses
962 were obtained using the FIJI plugin Puncta Analyzer[46]. 15 MPIs were analyzed for each
963 mouse (5 MPI/tissue section, 3 tissue sections/mouse). Between 4 and 5, age and sex-
964 matched mice/genotype/condition were analyzed for each synaptic staining combination,
965 as indicated in the figure legends. All animals appeared healthy at the time of collection.
966 No data were excluded.

967 **Cell counting, imaging, and analysis**

968 Tile scan images containing the anterior cingulated cortex (ACC) and primary motor
969 cortex (MOp) from P21 WT and LRRK2 G2019S$^{ki/ki}$; Aldh1l1-eGFP mice were acquired

970 on a confocal Leica SP8 STED microscope using the galvo scanner and 20x objective.
971 For ALDH1L1-EGFP and SOX9 double positive cell counting in the ACC and MOp, the
972 cells labeled with ALDH1L1-EGFP and SOX9 were counted by hand using the cell
973 counter tool in FIJI. 2-4 sections per brain from 3 sex and age-matched mice/genotype
974 were analyzed.

975 **Biochemical assays**

976 **mRNA extraction and cDNA preparation**

977 Cells stored in TRIzol (15596026, Invitrogen) were thawed and resuspended in 1 mL of
978 TRIzol. After adding 200 µL of chloroform, the samples were centrifuged at 12,000 g for
979 15 minutes at 4°C. The aqueous phase was collected, and RNA was precipitated with
980 GlycoBlue Coprecipitant (AM9515, Invitrogen) and isopropanol. The RNA pellet was
981 washed with 75% ethanol, air-dried, and resuspended in 40 µL of nuclease-free water.
982 The RNA was then isolated using the Zymo Research RNA Clean & Concentrator-5 Kit
983 (R1014, Zymo), quantified with the Qubit RNA HS Assay Kit (Q32852, Invitrogen), and
984 diluted to equalize concentrations. Finally, cDNA libraries were generated using qScript
985 cDNA SuperMix (101414-102, VWR) with a temperature profile of 25°C for 5 minutes,
986 42°C for 30 minutes, and 85°C for 5 minutes, and the resulting cDNA was diluted threefold
987 and stored at −80°C.

988 **Real-time qPCR**

989 cDNA samples were plated on a 96-well qPCR plate and incubated with Fast SYBR
990 Green Master Mix (4385616, Applied Biosystems), nuclease-free water, and the forward
991 and reverse primers of interest at a ratio of 5 µl SYBR: 3 µl water: 0.5 µl forward primer:
992 0.5 µl reverse primer: 1 µl sample. Each sample was plated two to four times to ensure

993 technical replicates. A control sample (water with primers and Master Mix) served as a
994 negative control. Cycle threshold values were collected for each well and normalized to
995 GAPDH as a housekeeping gene. The sequences of forward (F) and reverse (R) primers
996 used (5′→ 3′) are:

997 Atg7: (F) 5′- GTTCGCCCCCTTTAATAGTGC -3′ and (R) 5′-
998 TGAACTCCAACGTCAAGCGG -3′

999 **Protein extraction and Western blotting**

1000 Protein was extracted from cultured rat astrocytes using membrane solubilization buffer
1001 (25 mM Tris pH 7.4, 150 mM NaCl, 1 mM $CaCl_2$, 1 mM $MgCl_2$, 0.5% NP-40, and protease
1002 inhibitors). Cultured astrocytes were washed twice with ice-cold TBS containing 1 mM
1003 $CaCl_2$ and 1 mM $MgCl_2$ and incubated on ice in membrane solubilization buffer for
1004 20 minutes with occasional agitation. Cell lysates were collected, vortexed briefly, and
1005 centrifuged at 4°C at high speed for 10 minutes to pellet non-solubilized material. The
1006 supernatant was collected and stored at −80°C.

1007 Pierce BCA Protein Assay Kit (Thermo Fisher) was used to determine protein
1008 concentration, and lysates were mixed with 4x Pierce™ Reducing Sample Buffer (Thermo
1009 Scientific) and incubated at 45°C for 45 minutes to denature proteins. 7-10 µg (cultured
1010 astrocyte lysates) of protein was loaded into Bolt™ 4–12% Bus-Tris Plus gels (Thermo
1011 Scientific) and run at 150 V for 1 hour. Proteins were transferred at 100 V to PVDF
1012 membrane (Millipore) for 1.5 hours, blocked in 5% BSA in TBST (137 mM NaCl, 2.68 mM
1013 KCl, 24.7 mM Tris-Base, 0.1% (w/v) Tween 20) for 1 hour and incubated in primary
1014 antibodies overnight at 4°C. Primary antibodies used were: anti-LRRK2 (Rabbit, 1:500;

1015 ab133474, abcam, RRID:AB_2713963), GAPDH (mouse, 1:5000; ab8245, abcam,
1016 RRID:AB_2107448), β-actin (mouse, 1:5000; A5441, Millipore Sigma, RRID:AB_476744).
1017 The next day, membranes were washed with TBST, incubated in HRP secondary
1018 antibodies (Thermo Fisher Scientific) for 2 hours, washed in TBST, and imaged on a
1019 Biorad Gel Doc imaging system. Protein levels were quantified using FIJI.

1020 **Coimmunoprecipitation**

1021 Co-immunoprecipitation assays were performed in HEK293T cells. Cells were
1022 transfected 36 hours prior to lysis with Ezrin/Atg7 cDNA using X-tremeGENE HP (Roche)
1023 and grown to 85-90% confluency. At 36 hours post-transfection, cells were rinsed with 1x
1024 PBS and collected for lysis. Cellular lysis and protein extraction was conducted via brief
1025 vortexing in chilled membrane solubilization buffer (25mM HEPES, 150mM KCl, 1.5mM
1026 MgCl2, 0.5% NP40, 10% Glycerol) in the presence of both protease (cOmplete, Roche)
1027 and phosphatase (PhosSTOP, Roche) inhibitors. Protein concentrations of cell lysates
1028 were equalized using the Pierce™ BSA Protein Assay Kit (Thermo Fisher) and
1029 CLARIOstar Plus Plate Reader (BMG Labtech). Equalized cell lysates were incubated,
1030 while rotating, with Pierce™ Anti-c-Myc Magnetic Beads (Thermo Fisher) for 6 hours at
1031 4°C. Following this incubation, the beads were washed with chilled lysis buffer. Protein
1032 samples were eluted from beads through the addition of 2x Bromophenol Blue-free
1033 Laemilli Sample Buffer and heating to 95°C for 5 minutes. Eluted protein samples were
1034 subjected to western blot analysis and quantification using a SimpleWestern Jess
1035 (ProteinSimple) automated immunoassay system with a 12-230kDa Fluorescence
1036 Separation module and associated manufacturer's protocol. Primary antibodies used for
1037 protein detection were: Anti-Myc (Rabbit, 1:40, Cell Signaling Technologies, mAb#2278)

1038 and Anti-HA (Rat, 1:20, Roche, 11867423001). Signal detection was achieved using the
1039 following fluorescently conjugated secondary antibodies at a dilution of 1:100: IRDye®
1040 680RD Goat anti-Rabbit IgG (LI-COR, 926-68071) and IRDye® 680RD Goat anti-Rat IgG
1041 (LI-COR, 926-68076). Signal quantification was conducted with the Simple Western
1042 Compass software (https://www.bio-techne.com/resources/instrument-software-
1043 download-center/compass-software-simple-western, RRID: SCR_022930), utilizing
1044 quantitative electropherograms of detected signals. Ezrin co-immunoprecipitation signal
1045 intensity was background-subtracted and normalized to Ezrin protein load and Atg7 IP
1046 levels for statistical analysis. Statistical analysis was performed in GraphPad Prism 9,
1047 using One-way ANOVA with Tukey's multiple comparisons test and alpha threshold of
1048 0.05.

1049 **Protein interaction modeling**

1050 Full-length mouse Ezrin (UniProt ID: Q4KML7) and Atg7 (UniProt ID: Q9D906) were used
1051 for structure prediction in Alphafold 2.0 Multimer. The structure of Ezrin in the open
1052 conformation was generated by segmenting independently predicted Ezrin N- and C-
1053 termini and threading them onto an open ERM hinge structure using the PyMOL2
1054 molecular visualization software. To model the Ezrin:Atg7 interaction and associated
1055 conformational changes, the structures of Ezrin and the Atg7 homodimer were predicted
1056 and docked using Alphafold 2.0 Multimer. Conformational changes in the Ezrin:Atg7
1057 protein complex were assessed using PyMOL2 and CABS-flex 2.0[97]. For all predicted
1058 structure models, the highest-confidence structures, calculated via the predicted local
1059 distance difference test (pLDDT), were subjected to energy-minimization via AMBER

1060 relaxation. The resulting minimized structures were imported into PyMOL2 for
1061 representative model production.

1062 **Proteomic analysis**

1063 ***In vivo* BioID protein purification**

1064 *In vivo,* BioID experiments were performed as described in Takano et al., 2020 with
1065 modifications[98]. Genotype-matched animals (wild-type C57BL6 or LRRK2 G2019S$^{ki/ki}$)
1066 were bred to produce single-genotype litters. For each genotype (WT or G2019S), 6 pups
1067 were injected with AAVs carrying Astro-Ezrin-BioID (PHP.eB.GfaABC1D-Ezrin WT-
1068 BioID2-HA) or Astro-CYTO-BioID (PHP.eB.GfaABC1D-BioID2-HA). 2 genotype-matched
1069 cortices were pooled at the time of protein isolation, yielding 3 independent replicates per
1070 BioID construct. 12 total samples (3 per genotype per construct) were subjected to LC-
1071 MS/MS and downstream analysis. WT and LRRK2 G2019S$^{ki/ki}$ P0 – P2 mouse pups were
1072 anesthetized by hypothermia, and 1µl of each concentrated AAV-BioID vector was
1073 injected bilaterally into the cortex using a Hamilton syringe. Pups were monitored until
1074 they recovered on a heating pad. At P18, P19, and P20, biotin was subcutaneously
1075 injected at 24 mg/kg to increase the biotinylation efficiency. At P21, the cerebral cortices
1076 were removed and stored at -80° C. For the protein purification, each cortex was lysed in
1077 a buffer containing 50 mM Tris/HCl, pH 7.5; 150 mM NaCl; 1 mM EDTA; protease inhibitor
1078 mixture (Roche); and phosphatase inhibitor mixture (PhosSTOP, Roche). Next, an equal
1079 volume of buffer containing 50 mM Tris/HCl, pH 7.5; 150 mM NaCl; 1 mM EDTA; 0.4 %
1080 SDS; 2 % TritonX-100; 2 % deoxycholate; protease inhibitor mixture; and phosphatase
1081 inhibitor mixture was added to the samples, following by sonication and centrifugation at
1082 15,000 g for 10 min. The remaining supernatant was ultracentrifuged at 100,000g for

1083 30min at 4° C. Finally, SDS detergent was added to the samples and heated at 45 ° C for
1084 45 min. After cooling on ice, each sample was incubated with High-Capacity Streptavidin
1085 Agarose beads (ThermoFisher) at 4° C overnight. Following incubation, the beads were
1086 serially washed: 1) twice with a solution containing 2% SDS; 2) twice with a buffer 1%
1087 TritonX-100, 1% deoxycholate, 25 mM LiCl; 3) twice with 1M NaCl, and finally, five times
1088 with 50 mM ammonium bicarbonate. The biotinylated proteins attached to the agarose
1089 beads were eluted in a buffer of 125 mM Tris/HCl, pH6.8; 4 % SDS; 0.2 % β-
1090 mercaptoethanol; 20 % glycerol; 3 mM biotin at 60°C for 15min.

1091 **Sample Preparation**

1092 The Duke Proteomics and Metabolomics Shared Resource (DPMSR) received 12
1093 samples (3 of each WT CYT, GS CYT, WT EZR, and GS EZR) which were kept at -80C
1094 until processing. Samples were spiked with undigested bovine casein at a total of either
1095 1 or 2 pmol as an internal quality control standard. Next, they were reduced for 15 min at
1096 80C, alkylated with 20 mM iodoacetamide for 30 min at room temperature, then
1097 supplemented with a final concentration of 1.2% phosphoric acid and 636 µl of S-Trap
1098 (Protifi) binding buffer (90% MeOH/100mM TEAB). Proteins were trapped on the S-Trap
1099 micro cartridge, digested using 20 ng/µL sequencing grade trypsin (Promega) for 1 hr at
1100 47C, and eluted using 50 mM TEAB, followed by 0.2% FA, and lastly using 50% ACN/0.2%
1101 FA. All samples were then lyophilized to dryness. Samples were resuspended in 12 µl of
1102 1% TFA/2% acetonitrile with 12.5 fmol/µl of yeast ADH. A study pool QC (SPQC) was
1103 created by combining equal volumes of each sample.

1104 **LC-MS/MS Analysis**

1105 Quantitative LC/MS/MS was performed on 3 µL of each sample, using an MClass UPLC
1106 system (Waters Corp) coupled to a Thermo Orbitrap Fusion Lumos high resolution
1107 accurate mass tandem mass spectrometer (Thermo) equipped with a FAIMSPro device
1108 via a nanoelectrospray ionization source. Briefly, the sample was first trapped on a
1109 Symmetry C18 20 mm × 180 µm trapping column (5 µl/min at 99.9/0.1 v/v
1110 water/acetonitrile), after which the analytical separation was performed using a 1.8 µm
1111 Acquity HSS T3 C18 75 µm × 250 mm column (Waters Corp.) with a 90-min linear
1112 gradient of 5 to 30% acetonitrile with 0.1% formic acid at a flow rate of 400
1113 nanoliters/minute (nL/min) with a column temperature of 55C. Data collection on the
1114 Fusion Lumos mass spectrometer was performed for three difference compensation
1115 voltages (-40v, -60v, -80v). Within each CV, a data-dependent acquisition (DDA) mode
1116 of acquisition with a r=120,000 (@ m/z 200) full MS scan from m/z 375 – 1500 with a
1117 target AGC value of 4e5 ions was performed. MS/MS scans with HCD settings of 30%
1118 were acquired in the linear ion trap in “rapid” mode with a target AGC value of 1e4 and
1119 max fill time of 35 ms. The total cycle time for each CV was 0.66s, with total cycle times
1120 of 2 sec between like full MS scans. A 20s dynamic exclusion was employed to increase
1121 the depth of coverage. The total analysis cycle time for each sample injection was
1122 approximately 2 hours.

1123 **Quantitative Data Analysis**

1124 Following 15 total UPLC-MS/MS analyses (excluding conditioning runs, but including 3
1125 replicate SPQC samples), data were imported into Proteome Discoverer 3.0 (Thermo
1126 Scientific Inc.) and individual LCMS data files were aligned based on the accurate mass
1127 and retention time of detected precursor ions (“features”) using Minora Feature Detector

1128 algorithm in Proteome Discoverer. Relative peptide abundance was measured based on
1129 peak intensities of selected ion chromatograms of the aligned features across all runs.
1130 The MS/MS data was searched against the SwissProt *M. musculus* database, a common
1131 contaminant/spiked protein database (bovine albumin, bovine casein, yeast ADH, etc.),
1132 and an equal number of reversed-sequence "decoys" for false discovery rate
1133 determination. Sequest with INFERYS was utilized to produce fragment ion spectra and
1134 to perform the database searches. Database search parameters included fixed
1135 modification on Cys (carbamidomethyl) and variable modification on Met (oxidation).
1136 Search tolerances were 2ppm precursor and 0.8Da product ion with full trypsin enzyme
1137 rules. Peptide Validator and Protein FDR Validator nodes in Proteome Discoverer were
1138 used to annotate the data at a maximum 1% protein false discovery rate based on q-
1139 value calculations. Note that peptide homology was addressed using razor rules in which
1140 a peptide matched to multiple different proteins was exclusively assigned to the protein
1141 has more identified peptides. Protein homology was addressed by grouping proteins that
1142 had the same set of peptides to account for their identification. A master protein within a
1143 group was assigned based on % coverage.

1144 Prior to normalization, a filter was applied such that a peptide was removed if it was not
1145 measured at least twice across all samples and in at least 50% of the replicates in any
1146 one single group. After that filter, samples were total intensity normalized (total intensity
1147 of all peptides for a sample are summed and then normalized across all samples). Next,
1148 the following imputation strategy is applied to missing values. If less than half of the values
1149 are missing in a biological group, values are imputed with an intensity derived from a
1150 normal distribution of all values defined by measured values within the same intensity

1151 range (20 bins). If greater than half values are missing for a peptide in a group and a
1152 peptide intensity is > 5e6, then it was concluded that the peptide was misaligned and its
1153 measured intensity is set to 0. All remaining missing values are imputed with the lowest
1154 2% of all detected values. Peptide intensities were then subjected to a trimmed-mean
1155 normalization in which the top and bottom 10 percent of the signals were excluded, and
1156 the average of the remaining values was used to normalize across all samples. Lastly, all
1157 peptides belonging to the same protein were then summed into a single intensity. These
1158 normalized protein level intensities are what was used for the remainder of the analysis.

1159 To assess technical reproducibility, we calculated the % coefficient of variation (%CV) for
1160 each protein across 3 injections of an SPQC pool that were interspersed throughout the
1161 study (Table S4). The mean %CV of the SPQC pools was 11.7%, which is well within our
1162 expected analytical tolerances. To assess biological + technical variability, %CVs were
1163 measured for each protein across the individual groups which averaged 19.8%, which is
1164 also within our normal tolerances and indicated a reproducible IP and sample processing.

1165 As an initial statistical analysis, we calculated fold-changes between various sample
1166 groups based on the protein expression values and calculated two-tailed heteroscedastic
1167 t-test on log2-transformed data for this comparison. Those fold changes and p-values are
1168 presented for all proteins in Tables S5, S7, S9, and S10. False Discovery Rate (FDR)
1169 correction was performed using the Benjamini-Hochberg procedure, and these values are
1170 reported ("p.adjusted") in Tables S5, S7, S9, and S10. To optimize for discovery, we opted
1171 to use the less stringent parameter of unadjusted p-value for downstream analyses.
1172 Within supplemental tables, we have labeled proteins significantly more abundant ("Up",
1173 fold change >1.5 and unadjusted p-value <0.05), or less abundant ("Down", fold change

1174 >-1.5 and unadjusted p-value <0.05) in a particular genotype or BioID sample group.
1175 These annotated proteins were used for downstream analyses, including protein
1176 interaction networks using Cytoscape (v.3.9.1) and Gene Ontology (GO) enrichment
1177 analysis using the ClusterProfiler package for R, with all M. musculus genes as the
1178 reference background.

1179 **Mouse brain slice electrophysiology**

1180 For whole-cell patch-clamp recordings, 3-4 mice of each genotype and condition were
1181 used for miniature excitatory postsynaptic current (mEPSC) and miniature inhibitory
1182 postsynaptic current (mIPSC) measurements. WT and *LRRK2* G2019S$^{ki/ki}$ mice of both
1183 sexes were anesthetized with 200 mg/kg tribromoethanol (avertin) and decapitated. After
1184 decapitation, the brains were immersed in ice-cold artificial cerebrospinal fluid (aCSF, in
1185 mM): 125 NaCl, 2.5 KCl, 3 mM $MgCl_2$, 0.1 mM $CaCl_2$, 10 glucose, 25 $NaHCO_3$, 1.25
1186 $NaHPO_4$, 0.4 L-ascorbic acid, and 2 Na-pyruvate, pH 7.3-7.4 (310 mOsmol). 350 µm thick
1187 coronal slices containing the ACC were obtained using a vibrating tissue slicer (Leica
1188 VT1200; Leica Biosystems). Slices were immediately transferred to standard aCSF (33°C,
1189 continuously bubbled with 95% O_2 – 5% CO_2) containing the same as the low-calcium
1190 aCSF but with 1 mM $MgCl_2$ and 1-2 mM $CaCl_2$. After 30-minute incubation at 33°C, slices
1191 were transferred to a holding chamber with the same extracellular buffer at room
1192 temperature (RT: ~25°C). Brain slices were visualized by an upright microscope (BX61WI,
1193 Olympus) through a 40x water-immersion objective equipped with infrared-differential
1194 interference contrast optics in combination with a digital camera (ODA-IR2000WCTRL).
1195 Patch-clamp recordings were performed by using an EPC 10 patch-clamp amplifier,

1196 controlled by Patchmaster Software (HEKA). Data were acquired at a sampling rate of 50
1197 kHz and low-pass filtered at 6 kHz.

1198 To measure mEPSCs, the internal solution contained the following (in mM): 125 K-
1199 gluconate, 10 NaCl, 10 HEPES, 0.2 EGTA, 4.5 MgATP, 0.3 NaGTP, and 10 Na-
1200 phosphocreatine, pH adjusted to 7.2 – 7.4 with KOH and osmolality set to ~ 300 mOsmol.
1201 mEPSCs were measured in the aCSF bath solution containing 1 μM tetrodotoxin and 50
1202 μM Picrotoxin at -70 mV in voltage-clamp mode. To measure mIPSCs, the internal
1203 solution contained the following (in mM): 77 K-gluconate, 77 KCl, 10 HEPES, 0.2 EGTA,
1204 4.5 MgATP, 0.3 NaGTP, and 10 Na-phosphocreatine, pH adjusted to 7.2 – 7.4 with KOH
1205 and osmolality set to ~ 300 mOsmol. mIPSCs were measured in the aCSF bath solution
1206 containing 1 μM tetrodotoxin and 10 μM 6-cyano-7-nitroquinoxaline-2,3-dione (CNQX),
1207 and 50 μM D-2-amino-5-phosphonopentanoate (D-AP5) at -70 mV in voltage-clamp
1208 mode. mEPSCs and mIPSCs recorded at -70 mV were detected using Minhee Analysis
1209 software (https://github.com/parkgilbong/Minhee_Analysis_Pack). To analyze the
1210 frequency, events were counted over 5 minutes of recording. To obtain the average
1211 events for each cell, at least 100 non-overlapping events were detected and averaged.
1212 The peak amplitude of the average mEPSCs was measured relative to the baseline
1213 current.

1214 **Quantification and statistical analysis**

1215 All statistical analyses were performed in GraphPad Prism 9. Exact value of n, what n
1216 represents, and specific statistical tests for each experiment are indicated in the figure
1217 legend for each experiment. All data are represented as mean ± standard error of the
1218 mean, and data points are shown where applicable. Exact *P*-values are listed in the figure

1219 for each experiment. Where indicated, the unpaired two-tailed t-tests were run using
1220 Welch`s correction, and a correction for multiple comparisons was applied using Hom-
1221 Sidak method with an alpha threshold of 0.05 for adjusted *P*-value. A Geisser-
1222 Greenhouse correction was used for both One-way and Two-way ANOVA analyses. For
1223 Sholl analysis, statistical analyses were conducted using a custom code in R
1224 (https://github.com/Eroglu-Lab/In-Vitro-Sholl). A mixed-effect model with multiple
1225 comparisons made using the Tukey post-test was used for Sholl analysis to account for
1226 the variability per experiment as a random effect to evaluate differences between the
1227 conditions. Sample sizes were determined based on previous experience for each
1228 experiment to yield high power to detect specific effects. No statistical methods were used
1229 to predetermine the sample size. All experimental animals that appeared healthy at the
1230 time of tissue collection were processed for data collection.

1231 **ACKNOWLEDGMENTS**

1232 We thank Drs. Amy Lee, Zhiyong Liu, Nicole Calakos, Katja Brose, and Andrew Singleton
1233 for critical feedback about the manuscript. We thank Adam Okinaga and Donna Porter
1234 for their excellent technical help. This work was supported by a Foerster Bernstein
1235 Women In STEM Postdoctoral Fellowship to SW, and a Chan Zuckerberg Initiative,
1236 Neurodegeneration Challenge Network Collaborative grant (DAF2018-191999 and
1237 DAF2021-237435) to CE and ARLS, and by the N.I.H. grants R35-NS122140 to A.R.L.S.
1238 and R01-NS102237 to CE, and by the Michael J. Fox Foundation for Parkinson's
1239 Research (MJFF) Astrocyte Biology in PD pilot grant (MJFF 17914 to CE and ARLS), and
1240 by the joint efforts of MJFF and the Aligning Science Across Parkinson's (ASAP) initiative.
1241 MJFF administers the grant [ASAP-020607 to CE and SHS] on behalf of ASAP and the
1242 Michael J Fox Foundation. Dr. Cagla Eroglu is an HHMI Investigator. We are grateful to
1243 the Banner Sun Health Research Institute Brain and Body Donation Program of Sun City,
1244 Arizona for the provision of human biological materials. The Brain and Body Donation
1245 Program has been supported by the National Institute of Neurological Disorders and
1246 Stroke (U24 NS072026 National Brain and Tissue Resource for Parkinson's Disease and
1247 Related Disorders), the National Institute on Aging (P30AG19610 and P30AG072980,
1248 Arizona Alzheimer's Disease Center), the Arizona Biomedical Research Commission
1249 contracts 4001, 0011, 05-901 and 1001 to the Arizona Parkinson's Disease Consortium
1250 and the Michael J. Fox Foundation for Parkinson's Research.

1251

1252 **IP RIGHTS NOTICE**

1253 This article is subject to HHMI's Open Access to Publications policy. HHMI lab heads
1254 have previously granted a nonexclusive CC BY 4.0 license to the public and a
1255 sublicensable license to HHMI in their research articles. Pursuant to those licenses, the
1256 author-accepted manuscript of this article can be made freely available under a CC BY
1257 4.0 license immediately upon publication.

1258 **AUTHOR CONTRIBUTIONS**

1259 Conceptualization, SW, ARLS, and CE; Methodology, SW, RB, GS, DSB, LV, KS, JM,
1260 CXT, TT, MPR, KD, NB, LB, SHS, and CE; Investigation, SW, RB, GS, and LV; Formal
1261 analysis, SW, RB, GS, and LV; Resources, CXT, MPR, and KS; Writing – original draft,
1262 SW and CE; Writing – Review & Editing, SW, RL, and CE; Funding Acquisition, SW, SHS,
1263 ARLS, and CE.

1264 **DECLARATION OF INTERESTS**

1265 The authors declare no competing interests.

1266 **REFERENCE**

1267 1. Semyanov, A. and A. Verkhratsky, *Astrocytic processes: from tripartite synapses*
1268 *to the active milieu.* Trends Neurosci, 2021. **44**(10): p. 781-792.
1269 2. Allen, N.J. and C. Eroglu, *Cell Biology of Astrocyte-Synapse Interactions.*
1270 Neuron, 2017. **96**(3): p. 697-708.
1271 3. Clavreul, S., et al., *Cortical astrocytes develop in a plastic manner at both clonal*
1272 *and cellular levels.* Nat Commun, 2019. **10**(1): p. 4884.

1273 4. Torres-Ceja, B. and M.L. Olsen, *A closer look at astrocyte morphology:*
1274 *Development, heterogeneity, and plasticity at astrocyte leaflets.* Curr Opin
1275 Neurobiol, 2022. **74**: p. 102550.
1276 5. Farizatto, K.L.G. and K.T. Baldwin, *Astrocyte-synapse interactions during brain*
1277 *development.* Curr Opin Neurobiol, 2023. **80**: p. 102704.
1278 6. Tan, C.X. and C. Eroglu, *Cell adhesion molecules regulating astrocyte-neuron*
1279 *interactions.* Curr Opin Neurobiol, 2021. **69**: p. 170-177.
1280 7. Holt, L.M., et al., *Astrocyte morphogenesis is dependent on BDNF signaling via*
1281 *astrocytic TrkB.T1.* Elife, 2019. **8**.
1282 8. Kam, T.I., et al., *Microglia and astrocyte dysfunction in parkinson's disease.*
1283 Neurobiol Dis, 2020. **144**: p. 105028.
1284 9. Brandebura, A.N., et al., *Astrocyte contribution to dysfunction, risk and*
1285 *progression in neurodegenerative disorders.* Nat Rev Neurosci, 2023. **24**(1): p.
1286 23-39.
1287 10. Chan, C.S., T.S. Gertler, and D.J. Surmeier, *Calcium homeostasis, selective*
1288 *vulnerability and Parkinson's disease.* Trends Neurosci, 2009. **32**(5): p. 249-56.
1289 11. Dong, X.X., Y. Wang, and Z.H. Qin, *Molecular mechanisms of excitotoxicity and*
1290 *their relevance to pathogenesis of neurodegenerative diseases.* Acta Pharmacol
1291 Sin, 2009. **30**(4): p. 379-87.
1292 12. Booth, H.D.E., W.D. Hirst, and R. Wade-Martins, *The Role of Astrocyte*
1293 *Dysfunction in Parkinson's Disease Pathogenesis.* Trends Neurosci, 2017. **40**(6):
1294 p. 358-370.

1295 13. Gilks, W.P., et al., *A common LRRK2 mutation in idiopathic Parkinson's disease.*
1296 Lancet, 2005. **365**(9457): p. 415-6.
1297 14. Benamer, H.T., *The ancestry of LRRK2 Gly2019Ser parkinsonism.* Lancet
1298 Neurol, 2008. **7**(9): p. 769-70; author reply 770-1.
1299 15. Pang, S.Y., et al., *LRRK2, GBA and their interaction in the regulation of*
1300 *autophagy: implications on therapeutics in Parkinson's disease.* Transl
1301 Neurodegener, 2022. **11**(1): p. 5.
1302 16. Ren, C., et al., *G2019S Variation in LRRK2: An Ideal Model for the Study of*
1303 *Parkinson's Disease?* Front Hum Neurosci, 2019. **13**: p. 306.
1304 17. West, A.B., et al., *Parkinson's disease-associated mutations in leucine-rich*
1305 *repeat kinase 2 augment kinase activity.* Proc Natl Acad Sci U S A, 2005.
1306 **102**(46): p. 16842-7.
1307 18. Jaleel, M., et al., *LRRK2 phosphorylates moesin at threonine-558:*
1308 *characterization of how Parkinson's disease mutants affect kinase activity.*
1309 Biochem J, 2007. **405**(2): p. 307-17.
1310 19. Ito, G., et al., *Phos-tag analysis of Rab10 phosphorylation by LRRK2: a powerful*
1311 *assay for assessing kinase function and inhibitors.* Biochem J, 2016. **473**(17): p.
1312 2671-85.
1313 20. Steger, M., et al., *Systematic proteomic analysis of LRRK2-mediated Rab*
1314 *GTPase phosphorylation establishes a connection to ciliogenesis.* Elife, 2017. **6**.
1315 21. Zhang, Y., et al., *An RNA-sequencing transcriptome and splicing database of*
1316 *glia, neurons, and vascular cells of the cerebral cortex.* J Neurosci, 2014. **34**(36):
1317 p. 11929-47.

1318 22. Zhang, Y., et al., *Purification and Characterization of Progenitor and Mature*
1319 *Human Astrocytes Reveals Transcriptional and Functional Differences with*
1320 *Mouse.* Neuron, 2016. **89**(1): p. 37-53.
1321 23. Parisiadou, L., et al., *Phosphorylation of ezrin/radixin/moesin proteins by LRRK2*
1322 *promotes the rearrangement of actin cytoskeleton in neuronal morphogenesis.* J
1323 Neurosci, 2009. **29**(44): p. 13971-80.
1324 24. Parisiadou, L. and H. Cai, *LRRK2 function on actin and microtubule dynamics in*
1325 *Parkinson disease.* Commun Integr Biol, 2010. **3**(5): p. 396-400.
1326 25. Lavialle, M., et al., *Structural plasticity of perisynaptic astrocyte processes*
1327 *involves ezrin and metabotropic glutamate receptors.* Proc Natl Acad Sci U S A,
1328 2011. **108**(31): p. 12915-9.
1329 26. Derouiche, A., et al., *Anatomical aspects of glia-synapse interaction: the*
1330 *perisynaptic glial sheath consists of a specialized astrocyte compartment.* J
1331 Physiol Paris, 2002. **96**(3-4): p. 177-82.
1332 27. Bretscher, A., K. Edwards, and R.G. Fehon, *ERM proteins and merlin: integrators*
1333 *at the cell cortex.* Nat Rev Mol Cell Biol, 2002. **3**(8): p. 586-99.
1334 28. Gautreau, A., D. Louvard, and M. Arpin, *Morphogenic effects of ezrin require a*
1335 *phosphorylation-induced transition from oligomers to monomers at the plasma*
1336 *membrane.* J Cell Biol, 2000. **150**(1): p. 193-203.
1337 29. Zhu, L., et al., *High turnover of ezrin T567 phosphorylation: conformation,*
1338 *activity, and cellular function.* Am J Physiol Cell Physiol, 2007. **293**(3): p. C874-
1339 84.

1340 30. Endo, F., et al., *Molecular basis of astrocyte diversity and morphology across the*
1341 *CNS in health and disease.* Science, 2022. **378**(6619): p. eadc9020.
1342 31. Kruyer, A., et al., *Heroin Cue-Evoked Astrocytic Structural Plasticity at Nucleus*
1343 *Accumbens Synapses Inhibits Heroin Seeking.* Biol Psychiatry, 2019. **86**(11): p.
1344 811-819.
1345 32. Schacke, S., et al., *Ezrin deficiency triggers glial fibrillary acidic protein*
1346 *upregulation and a distinct reactive astrocyte phenotype.* Glia, 2022. **70**(12): p.
1347 2309-2329.
1348 33. Soto, J.S., et al., *Astrocyte-neuron subproteomes and obsessive-compulsive*
1349 *disorder mechanisms.* Nature, 2023.
1350 34. Matikainen-Ankney, B.A., et al., *Parkinson's Disease-Linked LRRK2-G2019S*
1351 *Mutation Alters Synaptic Plasticity and Promotes Resilience to Chronic Social*
1352 *Stress in Young Adulthood.* J Neurosci, 2018. **38**(45): p. 9700-9711.
1353 35. Matikainen-Ankney, B.A., et al., *Altered Development of Synapse Structure and*
1354 *Function in Striatum Caused by Parkinson's Disease-Linked LRRK2-G2019S*
1355 *Mutation.* J Neurosci, 2016. **36**(27): p. 7128-41.
1356 36. Stogsdill, J.A., et al., *Astrocytic neuroligins control astrocyte morphogenesis and*
1357 *synaptogenesis.* Nature, 2017. **551**(7679): p. 192-197.
1358 37. Dumas, L., et al., *RNA G-quadruplexes control mitochondria-localized mRNA*
1359 *translation and energy metabolism.* Nat Commun, 2025. **16**(1): p. 3292.
1360 38. Sofroniew, M.V. and H.V. Vinters, *Astrocytes: biology and pathology.* Acta
1361 Neuropathol, 2010. **119**(1): p. 7-35.

1362 39. Hol, E.M. and M. Pekny, *Glial fibrillary acidic protein (GFAP) and the astrocyte*
1363 *intermediate filament system in diseases of the central nervous system.* Curr
1364 Opin Cell Biol, 2015. **32**: p. 121-30.
1365 40. Yue, M., et al., *Progressive dopaminergic alterations and mitochondrial*
1366 *abnormalities in LRRK2 G2019S knock-in mice.* Neurobiol Dis, 2015. **78**: p. 172-
1367 95.
1368 41. Longo, F., et al., *Age-dependent dopamine transporter dysfunction and*
1369 *Serine129 phospho-alpha-synuclein overload in G2019S LRRK2 mice.* Acta
1370 Neuropathol Commun, 2017. **5**(1): p. 22.
1371 42. Kuhlmann, N. and A.J. Milnerwood, *A Critical LRRK at the Synapse? The*
1372 *Neurobiological Function and Pathophysiological Dysfunction of LRRK2.* Front
1373 Mol Neurosci, 2020. **13**: p. 153.
1374 43. Skelton, P.D., V. Tokars, and L. Parisiadou, *LRRK2 at Striatal Synapses: Cell-*
1375 *Type Specificity and Mechanistic Insights.* Cells, 2022. **11**(1).
1376 44. Fremeau, R.T., Jr., et al., *The expression of vesicular glutamate transporters*
1377 *defines two classes of excitatory synapse.* Neuron, 2001. **31**(2): p. 247-60.
1378 45. Micheva, K.D., et al., *Single-synapse analysis of a diverse synapse population:*
1379 *proteomic imaging methods and markers.* Neuron, 2010. **68**(4): p. 639-53.
1380 46. Ippolito, D.M. and C. Eroglu, *Quantifying synapses: an immunocytochemistry-*
1381 *based assay to quantify synapse number.* J Vis Exp, 2010(45).
1382 47. Glasgow, S.D., et al., *Approaches and Limitations in the Investigation of Synaptic*
1383 *Transmission and Plasticity.* Front Synaptic Neurosci, 2019. **11**: p. 20.

1384 48. Matsuzaki, M., et al., *Dendritic spine geometry is critical for AMPA receptor*
1385 *expression in hippocampal CA1 pyramidal neurons.* Nat Neurosci, 2001. **4**(11): p.
1386 1086-92.
1387 49. Bindu, D.S., et al., *GEARBOCS: An Adeno Associated Virus Tool for In Vivo*
1388 *Gene Editing in Astrocytes.* bioRxiv, 2024.
1389 50. Steger, M., et al., *Phosphoproteomics reveals that Parkinson's disease kinase*
1390 *LRRK2 regulates a subset of Rab GTPases.* Elife, 2016. **5**.
1391 51. Chua, C.E.L. and B.L. Tang, *Rab 10-a traffic controller in multiple cellular*
1392 *pathways and locations.* J Cell Physiol, 2018. **233**(9): p. 6483-6494.
1393 52. Fievet, B.T., et al., *Phosphoinositide binding and phosphorylation act sequentially*
1394 *in the activation mechanism of ezrin.* J Cell Biol, 2004. **164**(5): p. 653-9.
1395 53. Yin, L.M. and M. Schnoor, *Modulation of membrane-cytoskeleton interactions:*
1396 *ezrin as key player.* Trends Cell Biol, 2022. **32**(2): p. 94-97.
1397 54. Heiska, L., et al., *Association of ezrin with intercellular adhesion molecule-1 and -*
1398 *2 (ICAM-1 and ICAM-2). Regulation by phosphatidylinositol 4, 5-bisphosphate.* J
1399 Biol Chem, 1998. **273**(34): p. 21893-900.
1400 55. Zaman, R., et al., *Effector-mediated ERM activation locally inhibits RhoA activity*
1401 *to shape the apical cell domain.* J Cell Biol, 2021. **220**(6).
1402 56. Tsai, F.C., et al., *Ezrin enrichment on curved membranes requires a specific*
1403 *conformation or interaction with a curvature-sensitive partner.* Elife, 2018. **7**.
1404 57. Soto, J.S., et al., *Astrocyte-neuron subproteomes and obsessive-compulsive*
1405 *disorder mechanisms.* Nature, 2023. **616**(7958): p. 764-773.

1406 58. Plowey, E.D., et al., *Role of autophagy in G2019S-LRRK2-associated neurite*
1407 *shortening in differentiated SH-SY5Y cells.* J Neurochem, 2008. **105**(3): p. 1048-
1408 56.
1409 59. Mizushima, N., et al., *A protein conjugation system essential for autophagy.*
1410 Nature, 1998. **395**(6700): p. 395-8.
1411 60. Collier, J.J., et al., *Developmental Consequences of Defective ATG7-Mediated*
1412 *Autophagy in Humans.* N Engl J Med, 2021. **384**(25): p. 2406-2417.
1413 61. Evans, R., et al., *Protein complex prediction with AlphaFold-Multimer.* bioRxiv,
1414 2022: p. 2021.10.04.463034.
1415 62. Kaiser, S.E., et al., *Structures of Atg7-Atg3 and Atg7-Atg10 reveal noncanonical*
1416 *mechanisms of E2 recruitment by the autophagy E1.* Autophagy, 2013. **9**(5): p.
1417 778-80.
1418 63. Pelaseyed, T., et al., *Ezrin activation by LOK phosphorylation involves a PIP(2)-*
1419 *dependent wedge mechanism.* Elife, 2017. **6**.
1420 64. Kawaguchi, K. and S. Asano, *Pathophysiological Roles of Actin-Binding Scaffold*
1421 *Protein, Ezrin.* Int J Mol Sci, 2022. **23**(6).
1422 65. Bravo-San Pedro, J.M., et al., *The LRRK2 G2019S mutant exacerbates basal*
1423 *autophagy through activation of the MEK/ERK pathway.* Cell Mol Life Sci, 2013.
1424 **70**(1): p. 121-36.
1425 66. Alessi, D.R. and S.R. Pfeffer, *Leucine-Rich Repeat Kinases.* Annu Rev Biochem,
1426 2024. **93**(1): p. 261-287.

1427 67. Zhang, Y., et al., *The role of ubiquitin proteasomal system and autophagy-*
1428 *lysosome pathway in Alzheimer's disease.* Rev Neurosci, 2017. **28**(8): p. 861-
1429 868.
1430 68. Harris, L.D., S. Jasem, and J.D.F. Licchesi, *The Ubiquitin System in Alzheimer's*
1431 *Disease.* Adv Exp Med Biol, 2020. **1233**: p. 195-221.
1432 69. Rotin, D. and G. Prag, *Physiological Functions of the Ubiquitin Ligases Nedd4-1*
1433 *and Nedd4-2.* Physiology (Bethesda), 2024. **39**(1): p. 18-29.
1434 70. Singh, S.K., et al., *Astrocytes Assemble Thalamocortical Synapses by Bridging*
1435 *NRX1alpha and NL1 via Hevin.* Cell, 2016. **164**(1-2): p. 183-196.
1436 71. Kucukdereli, H., et al., *Control of excitatory CNS synaptogenesis by astrocyte-*
1437 *secreted proteins Hevin and SPARC.* Proc Natl Acad Sci U S A, 2011. **108**(32):
1438 p. E440-9.
1439 72. Pelaseyed, T. and A. Bretscher, *Regulation of actin-based apical structures on*
1440 *epithelial cells.* J Cell Sci, 2018. **131**(20).
1441 73. Lombardo, A.T., et al., *ARHGAP18-Ezrin functions as a RhoA autoregulatory*
1442 *module in the organization of apical microvilli.* bioRxiv, 2023: p.
1443 2022.09.12.507663.
1444 74. Broadhead, M.J., et al., *Selective vulnerability of tripartite synapses in*
1445 *amyotrophic lateral sclerosis.* Acta Neuropathol, 2022. **143**(4): p. 471-486.
1446 75. Chang, E.E.S., et al., *LRRK2 mutant knock-in mouse models: therapeutic*
1447 *relevance in Parkinson's disease.* Transl Neurodegener, 2022. **11**(1): p. 10.
1448 76. Blesa, J., et al., *Motor and non-motor circuit disturbances in early Parkinson*
1449 *disease: which happens first?* Nat Rev Neurosci, 2022. **23**(2): p. 115-128.

1450 77. Hussein, A., et al., *Non-Motor Symptoms of Parkinson's Disease: The*
1451 *Neurobiology of Early Psychiatric and Cognitive Dysfunction.* Neuroscientist,
1452 2023. **29**(1): p. 97-116.
1453 78. Guevara, C.A., et al., *LRRK2 mutation alters behavioral, synaptic, and*
1454 *nonsynaptic adaptations to acute social stress.* J Neurophysiol, 2020. **123**(6): p.
1455 2382-2389.
1456 79. Hussein, A., et al., *Cognitive deficits and altered cholinergic innervation in young*
1457 *adult male mice carrying a Parkinson's disease Lrrk2(G2019S) knockin mutation.*
1458 Exp Neurol, 2022. **355**: p. 114145.
1459 80. Shenhav, A., M.M. Botvinick, and J.D. Cohen, *The expected value of control: an*
1460 *integrative theory of anterior cingulate cortex function.* Neuron, 2013. **79**(2): p.
1461 217-40.
1462 81. Tervo, D.G.R., et al., *The anterior cingulate cortex directs exploration of*
1463 *alternative strategies.* Neuron, 2021. **109**(11): p. 1876-1887 e6.
1464 82. Lanjakornsiripan, D., et al., *Layer-specific morphological and molecular*
1465 *differences in neocortical astrocytes and their dependence on neuronal layers.*
1466 Nat Commun, 2018. **9**(1): p. 1623.
1467 83. Bayraktar, O.A., et al., *Astrocyte layers in the mammalian cerebral cortex*
1468 *revealed by a single-cell in situ transcriptomic map.* Nat Neurosci, 2020. **23**(4): p.
1469 500-509.
1470 84. Khan, S.S., et al., *Loss of primary cilia and dopaminergic neuroprotection in*
1471 *pathogenic LRRK2-driven and idiopathic Parkinson's disease.* bioRxiv, 2024: p.
1472 2024.01.15.575737.

1473 85. Zimmer, T.S., A.L. Orr, and A.G. Orr, *Astrocytes in selective vulnerability to*
1474 *neurodegenerative disease.* Trends Neurosci, 2024. **47**(4): p. 289-302.
1475 86. Murk, K., et al., *The antagonistic modulation of Arp2/3 activity by N-WASP,*
1476 *WAVE2 and PICK1 defines dynamic changes in astrocyte morphology.* J Cell
1477 Sci, 2013. **126**(Pt 17): p. 3873-83.
1478 87. Savage, J.T., et al., *SynBot: An open-source image analysis software for*
1479 *automated quantification of synapses.* bioRxiv, 2024.
1480 88. Kim, Y.G., J.J. Shin, and S.J. Kim, *Minhee Analysis Package: an integrated*
1481 *software package for detection and management of spontaneous synaptic*
1482 *events.* Mol Brain, 2021. **14**(1): p. 138.
1483 89. Tan, C.X., et al., *delta-Catenin controls astrocyte morphogenesis via layer-*
1484 *specific astrocyte-neuron cadherin interactions.* J Cell Biol, 2023. **222**(11).
1485 90. Moffat, J., et al., *A lentiviral RNAi library for human and mouse genes applied to*
1486 *an arrayed viral high-content screen.* Cell, 2006. **124**(6): p. 1283-98.
1487 91. Chih, B., L. Gollan, and P. Scheiffele, *Alternative splicing controls selective trans-*
1488 *synaptic interactions of the neuroligin-neurexin complex.* Neuron, 2006. **51**(2): p.
1489 171-8.
1490 92. Chen, F. and J. LoTurco, *A method for stable transgenesis of radial glia lineage*
1491 *in rat neocortex by piggyBac mediated transposition.* J Neurosci Methods, 2012.
1492 **207**(2): p. 172-80.
1493 93. O'Neil, S.D., et al., *Action potential-coupled Rho GTPase signaling drives*
1494 *presynaptic plasticity.* Elife, 2021. **10**.

1495 94. Ferreira, T.A., et al., *Neuronal morphometry directly from bitmap images.* Nat
1496 Methods, 2014. **11**(10): p. 982-4.
1497 95. Uezu, A., et al., *Identification of an elaborate complex mediating postsynaptic*
1498 *inhibition.* Science, 2016. **353**(6304): p. 1123-9.
1499 96. Risher, W.C., et al., *Thrombospondin receptor alpha2delta-1 promotes*
1500 *synaptogenesis and spinogenesis via postsynaptic Rac1.* J Cell Biol, 2018.
1501 **217**(10): p. 3747-3765.
1502 97. Kuriata, A., et al., *CABS-flex 2.0: a web server for fast simulations of flexibility of*
1503 *protein structures.* Nucleic Acids Res, 2018. **46**(W1): p. W338-W343.
1504 98. Takano, T., et al., *Chemico-genetic discovery of astrocytic control of inhibition in*
1505 *vivo.* Nature, 2020. **588**(7837): p. 296-302.

1506

Figure 1

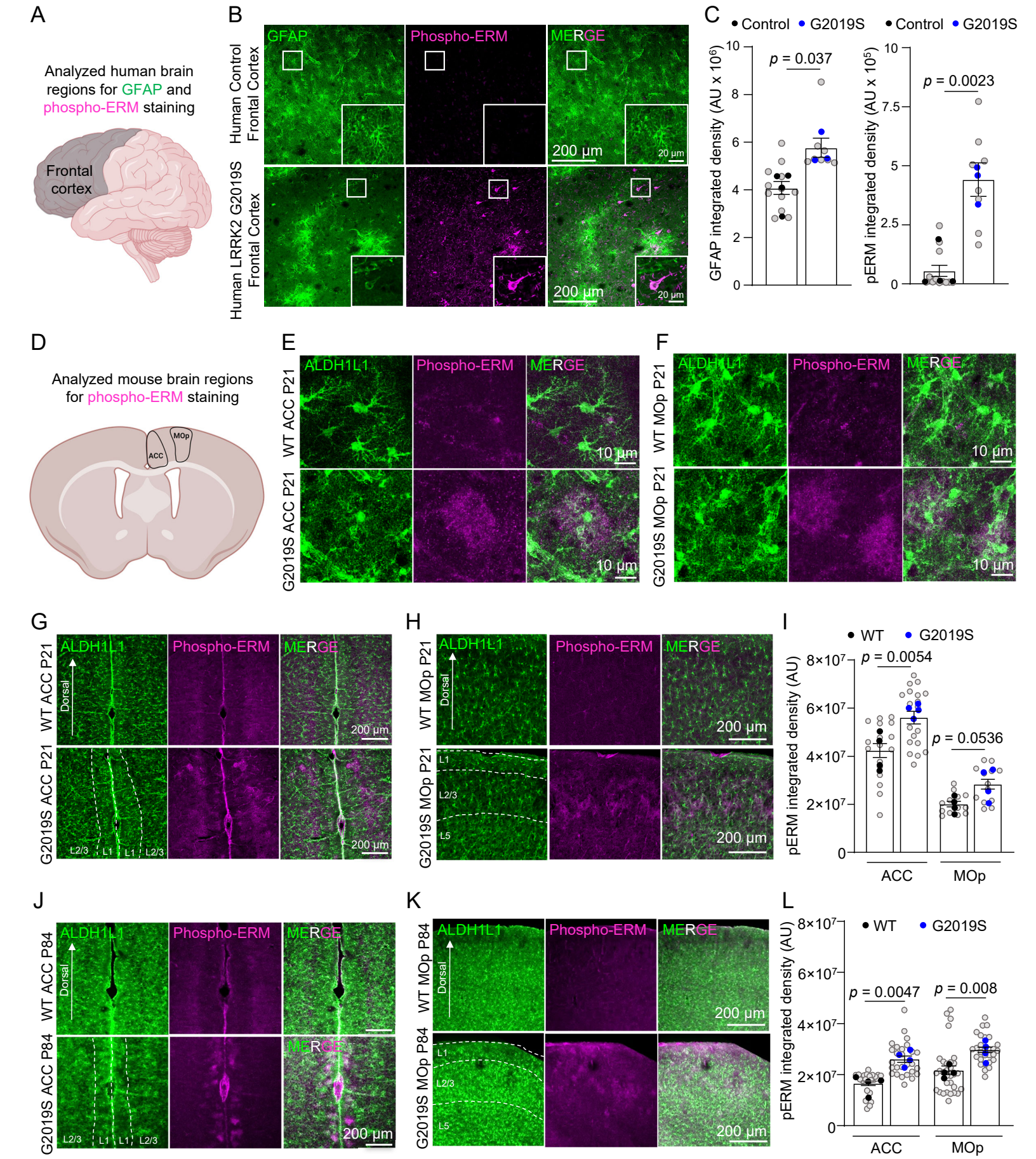
A
Analyzed human brain regions for GFAP and phospho-ERM staining
Frontal cortex
B
Human Control Frontal Cortex
Human LRRK2 G2019S Frontal Cortex
GFAP
Phospho-ERM
MERGE
200 µm
20 µm
C
Control
G2019S
GFAP integrated density (AU x 10^6)
p = 0.037
pERM integrated density (AU x 10^5)
p = 0.0023
D
Analyzed mouse brain regions for phospho-ERM staining
ACC
MOp
E
WT ACC P21
G2019S ACC P21
ALDH1L1
Phospho-ERM
MERGE
10 µm
F
WT MOp P21
G2019S MOp P21
G
Dorsal
L2/3
L1
L5
H
I
WT
G2019S
pERM integrated density (AU)
p = 0.0054
p = 0.0536
ACC
MOp
J
WT ACC P84
G2019S ACC P84
K
WT MOp P84
G2019S MOp P84
L
p = 0.0047
p = 0.008

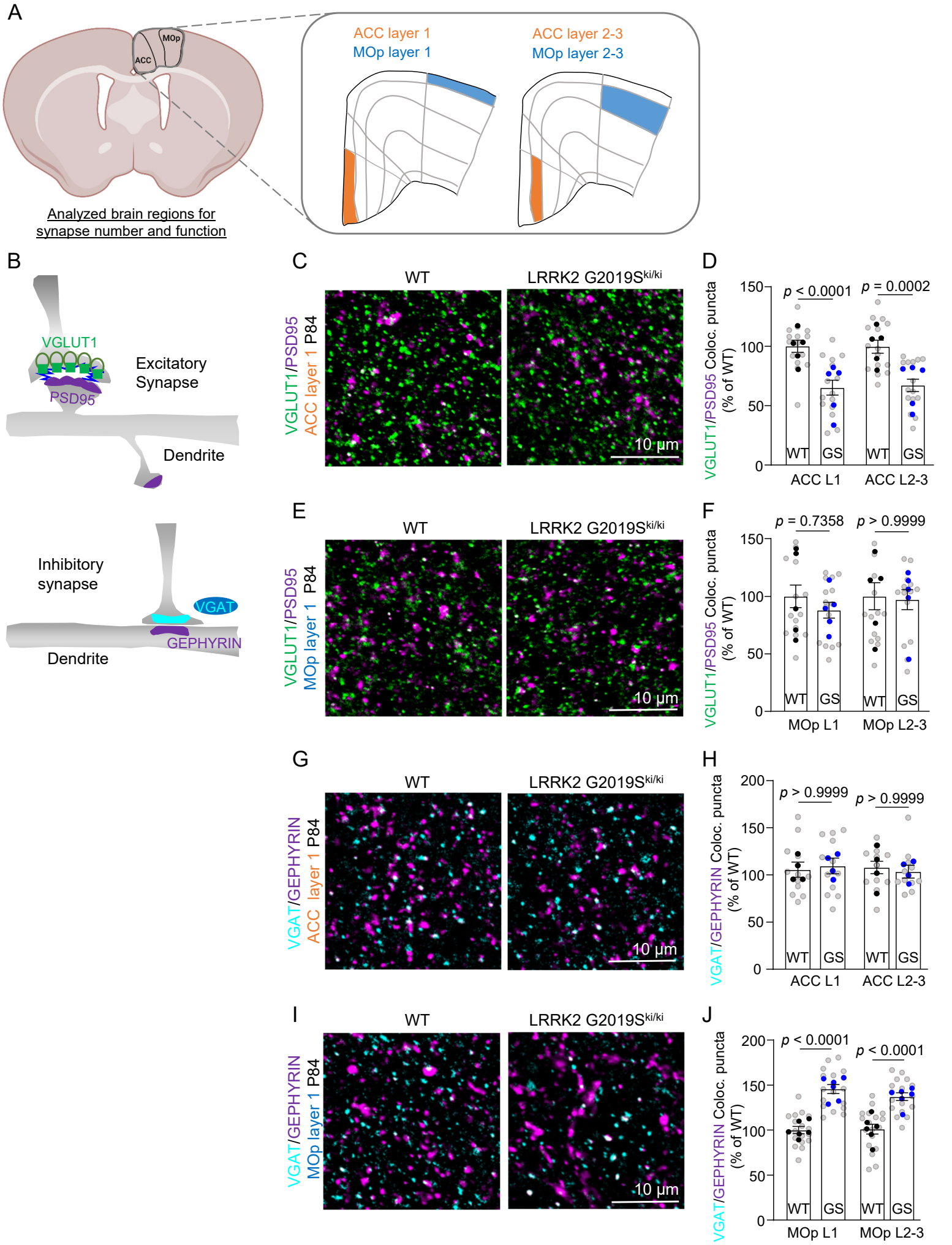
A
MOp
ACC
ACC layer 1
MOp layer 1
ACC layer 2-3
MOp layer 2-3
Analyzed brain regions for synapse number and function
B
VGLUT1
PSD95
Excitatory Synapse
Dendrite
Inhibitory synapse
VGAT
GEPHYRIN
Dendrite
C
WT
LRRK2 G2019S ki/ki
VGLUT1/PSD95
ACC layer 1 P84
10 µm
D
VGLUT1/PSD95 Coloc. puncta (% of WT)
p < 0.0001
p = 0.0002
WT
GS
ACC L1
ACC L2-3
E
VGLUT1/PSD95
MOp layer 1 P84
F
p = 0.7358
p > 0.9999
MOp L1
MOp L2-3
G
VGAT/GEPHYRIN
ACC layer 1 P84
H
VGAT/GEPHYRIN Coloc. puncta (% of WT)
p > 0.9999
I
VGAT/GEPHYRIN
MOp layer 1 P84
J
p < 0.0001

Figure 3

Wang et al.,

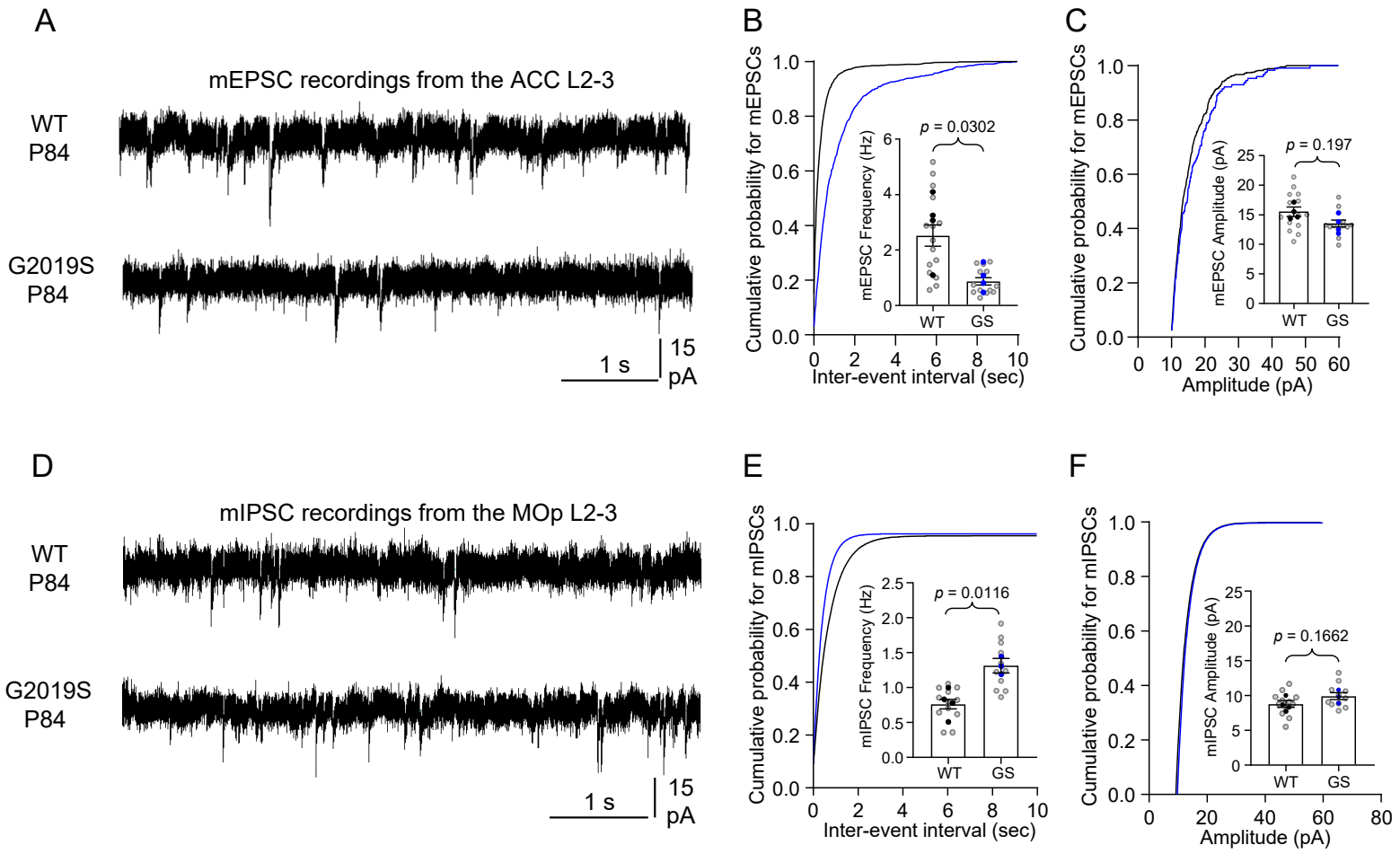

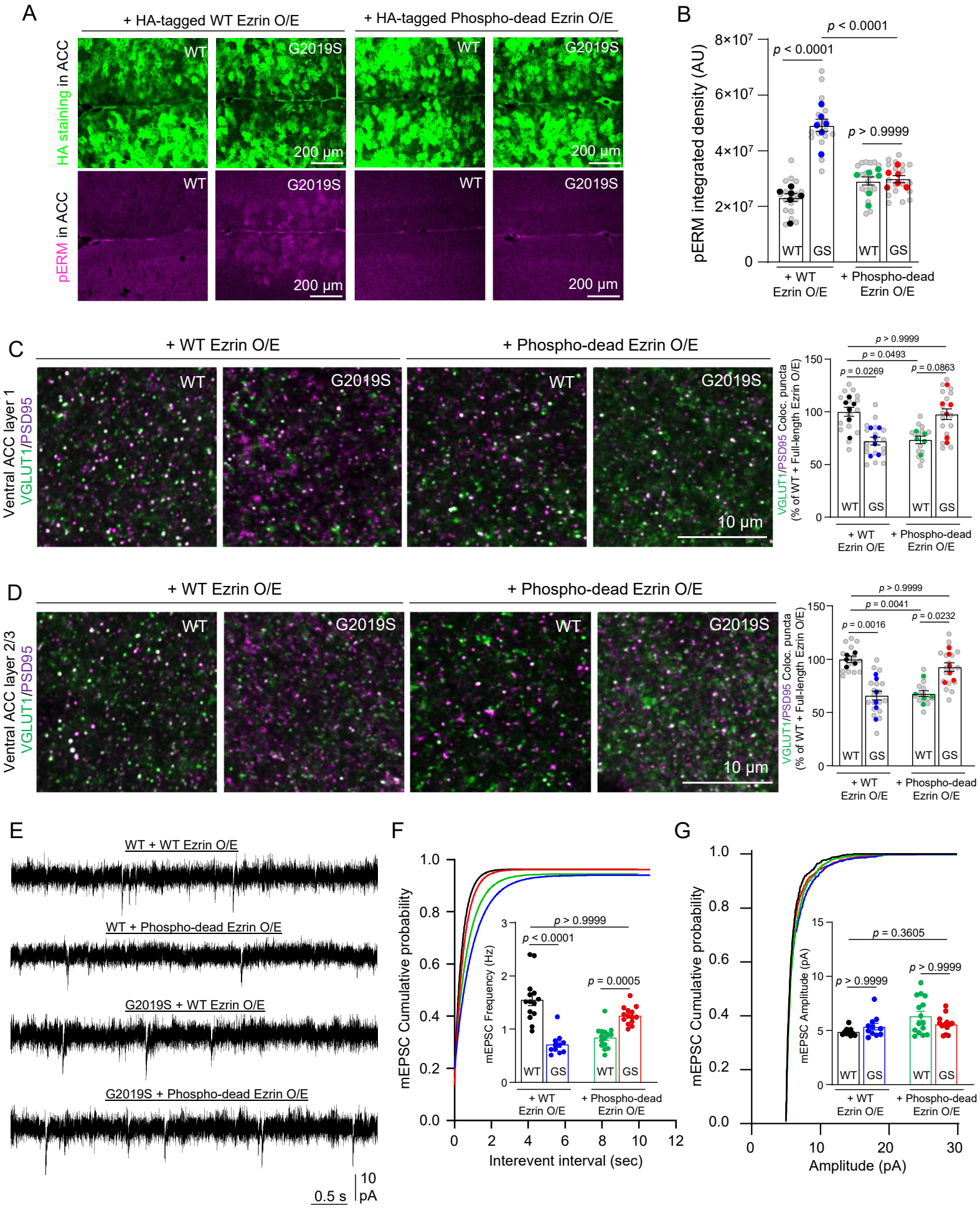
A
+ HA-tagged WT Ezrin O/E
+ HA-tagged Phospho-dead Ezrin O/E
HA staining in ACC
pERM in ACC
WT
G2019S
200 µm
B
pERM integrated density (AU)
p < 0.0001
p > 0.9999
+ WT Ezrin O/E
+ Phospho-dead Ezrin O/E
C
+ WT Ezrin O/E
+ Phospho-dead Ezrin O/E
Ventral ACC layer 1
VGLUT1/PSD95
10 µm
VGLUT1/PSD95 Coloc. puncta (% of WT + Full-length Ezrin O/E)
p = 0.0269
p = 0.0493
p = 0.0863
D
Ventral ACC layer 2/3
p = 0.0016
p = 0.0041
p = 0.0232
E
WT + WT Ezrin O/E
WT + Phospho-dead Ezrin O/E
G2019S + WT Ezrin O/E
G2019S + Phospho-dead Ezrin O/E
0.5 s
10 pA
F
mEPSC Cumulative probability
mEPSC Frequency (Hz)
p = 0.0005
Interevent interval (sec)
G
mEPSC Amplitude (pA)
p = 0.3605
Amplitude (pA)

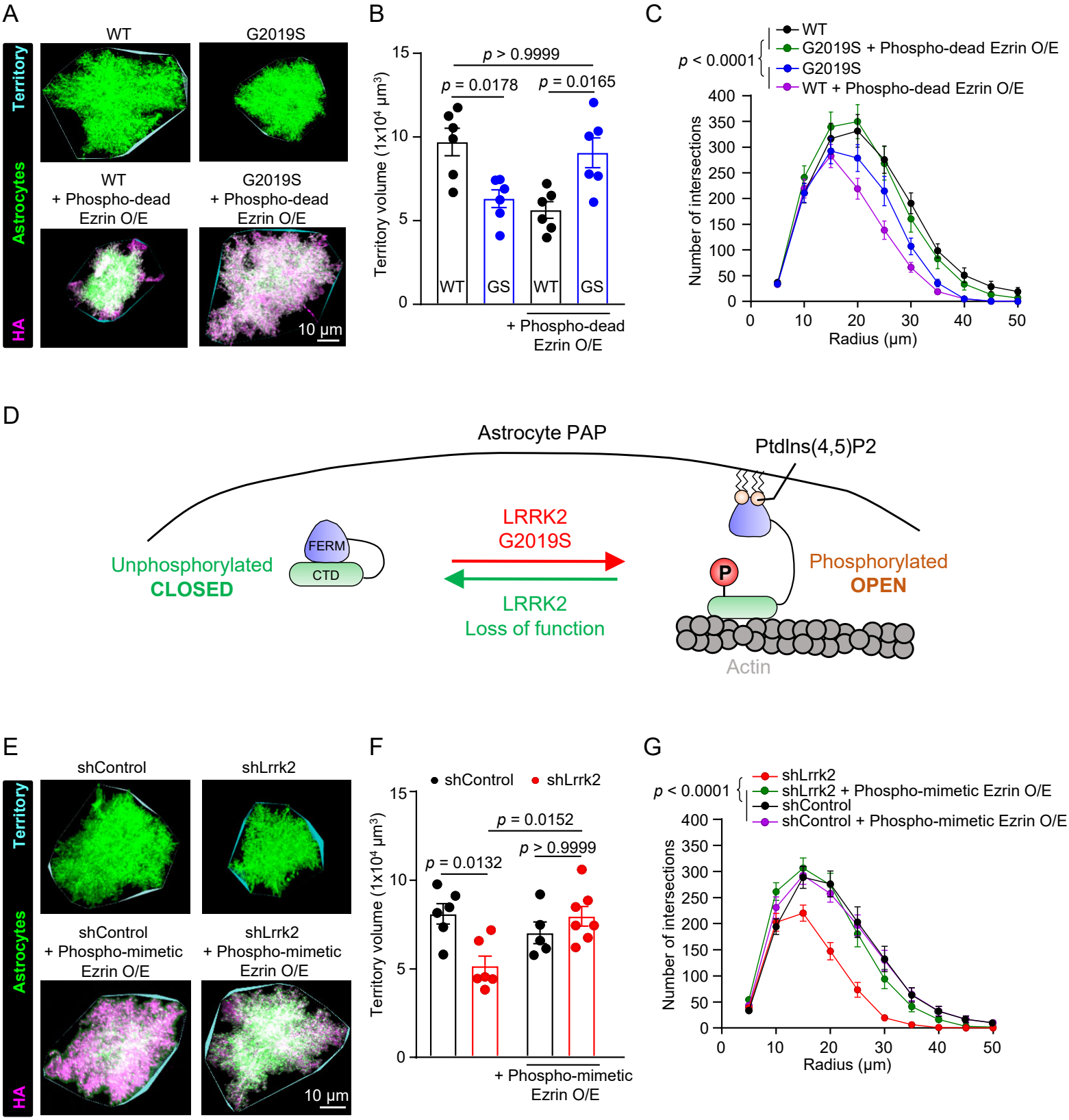
A
WT
G2019S
Territory
Astrocytes
HA
WT
+ Phospho-dead
Ezrin O/E
G2019S
+ Phospho-dead
Ezrin O/E
10 µm
B
Territory volume (1x10⁴ µm³)
p > 0.9999
p = 0.0178
p = 0.0165
WT
GS
WT
GS
+ Phospho-dead
Ezrin O/E
C
p < 0.0001
WT
G2019S + Phospho-dead Ezrin O/E
G2019S
WT + Phospho-dead Ezrin O/E
Number of intersections
Radius (µm)
D
Astrocyte PAP
PtdIns(4,5)P2
FERM
CTD
Unphosphorylated
CLOSED
LRRK2
G2019S
LRRK2
Loss of function
P
Phosphorylated
OPEN
Actin
E
shControl
shLrrk2
Territory
Astrocytes
HA
shControl
+ Phospho-mimetic
Ezrin O/E
shLrrk2
+ Phospho-mimetic
Ezrin O/E
10 µm
F
shControl
shLrrk2
Territory volume (1x10⁴ µm³)
p = 0.0152
p = 0.0132
p > 0.9999
+ Phospho-mimetic
Ezrin O/E
G
p < 0.0001
shLrrk2
shLrrk2 + Phospho-mimetic Ezrin O/E
shControl
shControl + Phospho-mimetic Ezrin O/E
Number of intersections
Radius (µm)

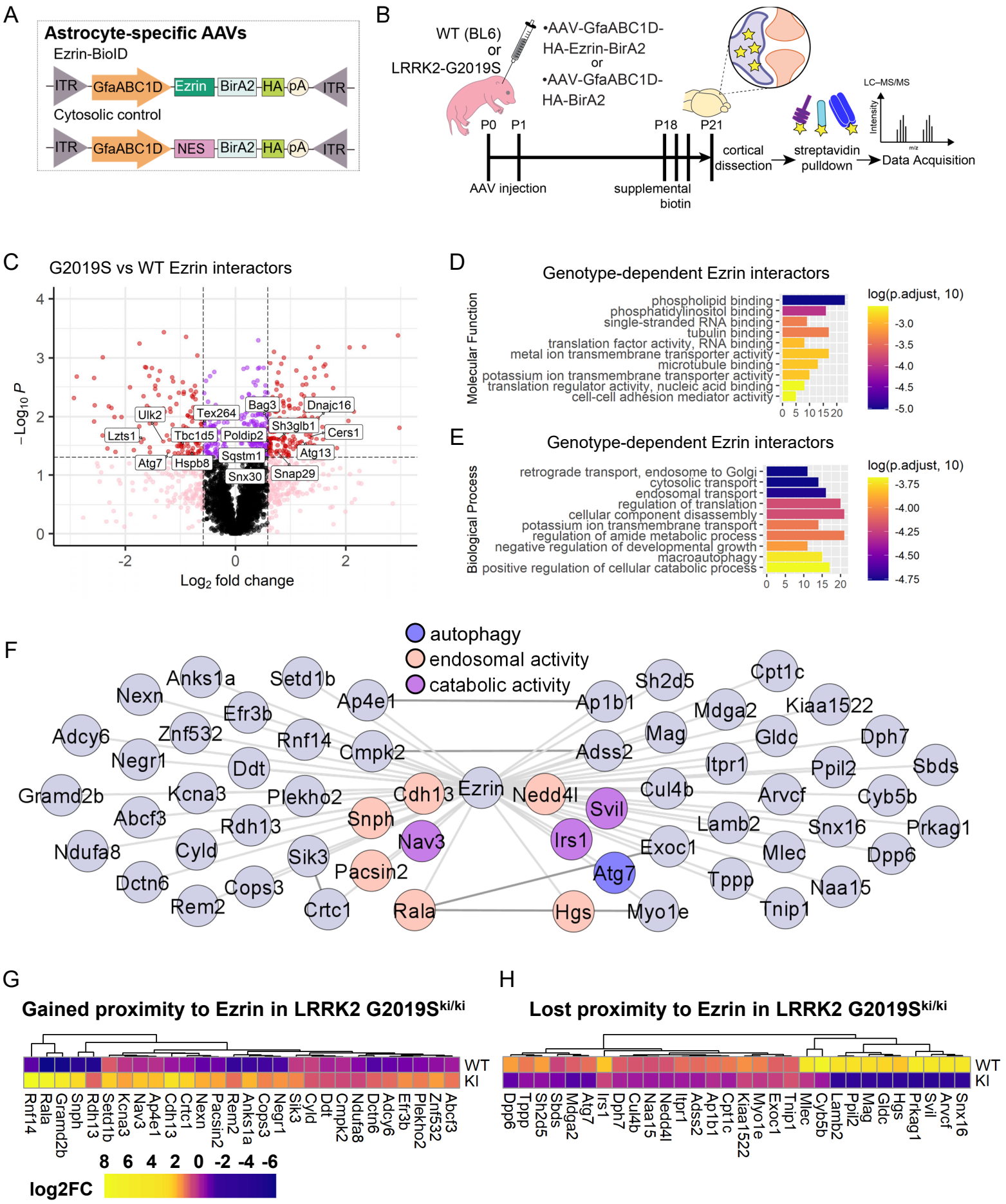
A
Astrocyte-specific AAVs
Ezrin-BioID
ITR GfaABC1D Ezrin BirA2 HA pA ITR
Cytosolic control
ITR GfaABC1D NES BirA2 HA pA ITR
B
WT (BL6) or LRRK2-G2019S
•AAV-GfaABC1D-HA-Ezrin-BirA2 or •AAV-GfaABC1D-HA-BirA2
P0 P1 P18 P21
AAV injection
supplemental biotin
cortical dissection
streptavidin pulldown
LC–MS/MS
Data Acquisition
C
G2019S vs WT Ezrin interactors
−Log10 P
Log2 fold change
Ulk2 Tex264 Bag3 Dnajc16 Lzts1 Tbc1d5 Poldip2 Sh3glb1 Cers1 Atg7 Hspb8 Sqstm1 Atg13 Snx30 Snap29
D
Genotype-dependent Ezrin interactors
Molecular Function
phospholipid binding
phosphatidylinositol binding
single-stranded RNA binding
tubulin binding
translation factor activity, RNA binding
metal ion transmembrane transporter activity
microtubule binding
potassium ion transmembrane transporter activity
translation regulator activity, nucleic acid binding
cell-cell adhesion mediator activity
log(p.adjust, 10)
E
Genotype-dependent Ezrin interactors
Biological Process
retrograde transport, endosome to Golgi
cytosolic transport
endosomal transport
regulation of translation
cellular component disassembly
potassium ion transmembrane transport
regulation of amide metabolic process
negative regulation of developmental growth
macroautophagy
positive regulation of cellular catabolic process
log(p.adjust, 10)
F
autophagy
endosomal activity
catabolic activity
Ezrin
G
Gained proximity to Ezrin in LRRK2 G2019Ski/ki
WT
KI
log2FC
H
Lost proximity to Ezrin in LRRK2 G2019Ski/ki
WT
KI

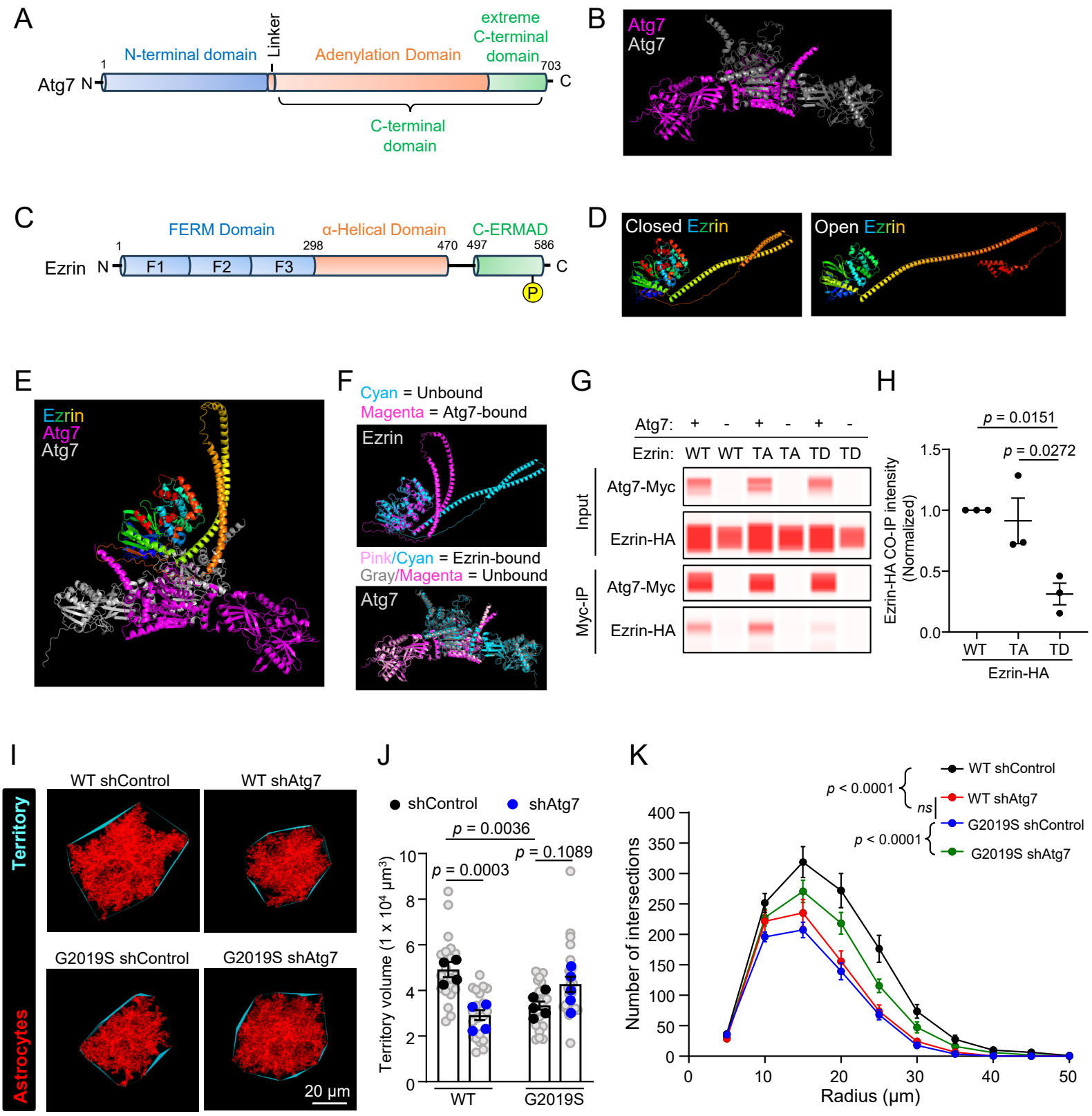
A
Atg7 N
1
N-terminal domain
Linker
Adenylation Domain
extreme C-terminal domain
703
C
C-terminal domain
B
Atg7
Atg7
C
Ezrin N
1
FERM Domain
F1
F2
F3
298
α-Helical Domain
470
497
C-ERMAD
586
C
P
D
Closed Ezrin
Open Ezrin
E
Ezrin
Atg7
Atg7
F
Cyan = Unbound
Magenta = Atg7-bound
Ezrin
Pink/Cyan = Ezrin-bound
Gray/Magenta = Unbound
Atg7
G
Atg7: + - + - + -
Ezrin: WT WT TA TA TD TD
Input
Atg7-Myc
Ezrin-HA
Myc-IP
Atg7-Myc
Ezrin-HA
H
p = 0.0151
p = 0.0272
Ezrin-HA CO-IP intensity (Normalized)
1.5
1.0
0.5
0.0
WT TA TD
Ezrin-HA
I
Territory
Astrocytes
WT shControl
WT shAtg7
G2019S shControl
G2019S shAtg7
20 µm
J
shControl
shAtg7
p = 0.0036
p = 0.0003
p = 0.1089
Territory volume (1 x 10⁴ µm³)
10
8
6
4
2
0
WT
G2019S
K
WT shControl
WT shAtg7
G2019S shControl
G2019S shAtg7
p < 0.0001
ns
p < 0.0001
Number of intersections
400
350
300
250
200
150
100
50
0
0 10 20 30 40 50
Radius (µm)

Supplemental information

PD-linked LRRK2 G2019S mutation impairs astrocyte morphology and synapse maintenance via ERM hyperphosphorylation

Shiyi Wang, Ryan Baumert, Gabrielle Séjourné, Dhanesh Sivadasan Bindu, Kylie Dimond, Kristina Sakers, Leslie Vazquez, Jessica Moore, Christabel Xin Tan, Tetsuya Takano, Maria Pia Rodriguez, Nick Brose, Luke Bradley, Reed Lessing, Scott H. Soderling, Albert R. La Spada, and Cagla Eroglu

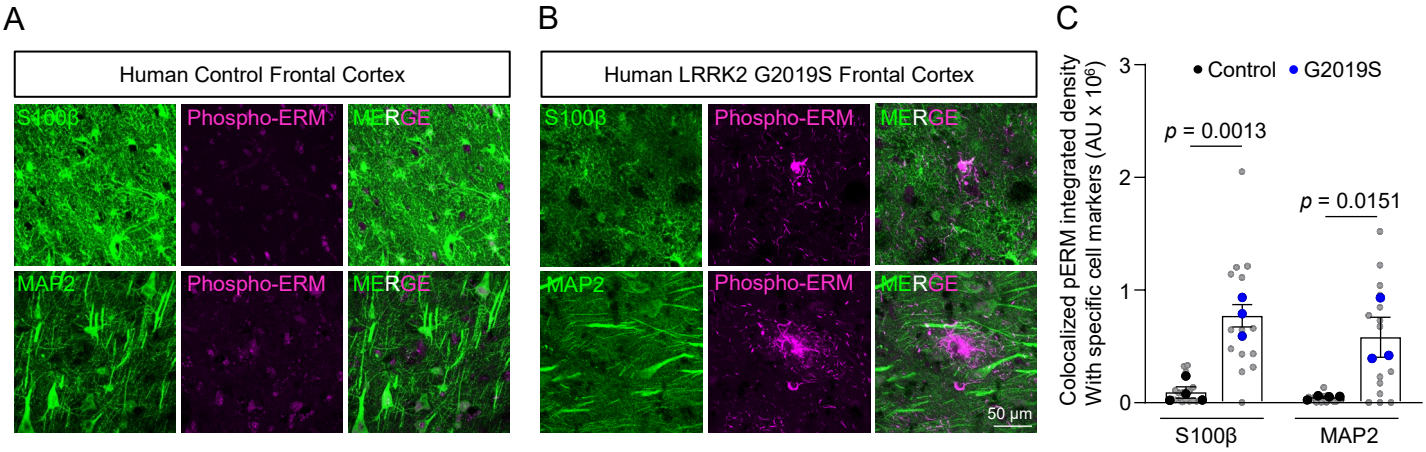

Figure S1: Human phospho-ERM is significantly increased and colocalizes with S100β and MAP2. Related to Figure 1.

(A-B) Representative confocal images of phospho-ERM (purple) and S100β (green) or MAP2 (green) in the frontal cortex of human control subjects or human PD patients carrying LRRK2 G2019S mutation carriers at age >80 years old. Scale bar, 50 µm. **(C)** Quantification of phospho-ERM integrated density in (A-B), n = 4 (Human control, 3 males and 1 female), 3 (LRRK2 G2019S mutation carriers, 2 males and 1 female) subjects, nested t-test, unpaired two-tailed t-test. For colocalized phospho-ERM with S100β, t (5) = 6.541, p = 0.0013. For colocalized phospho-ERM with MAP2, t (5) = 3.625, p = 0.0151. Grey dots are the data acquired from each image. Black dots are the averaged data acquired from each control subject. Blue dots are the averaged data acquired from each LRRK2 G2019S mutation carrier.

Figure S2 (related to Figure 1) **Wang et al.,**

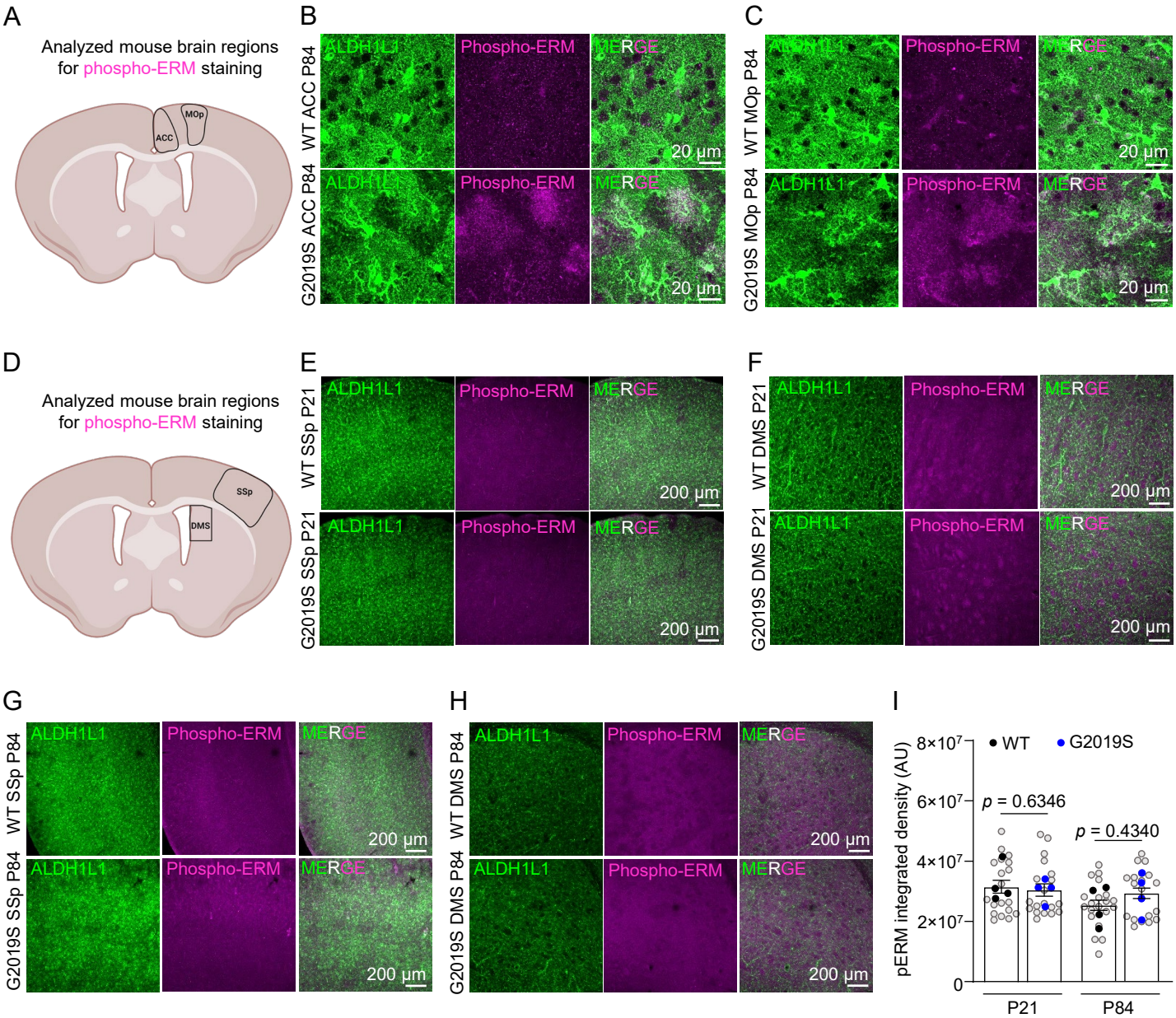

Figure S2: Phospho-ERM is upregulated in LRRK2 G2019S$^{ki/ki}$ astrocytes in ACC and MOp but not SSp and DMS. Related to Figure 1.

(A) Schematic representation of analyzed mouse brain regions for phospho-ERM staining, the ACC, and the MOp. **(B-C)** Representative confocal images of ERM phosphorylation (purple) in the ACC and MOp of WT or LRRK2 G2019S$^{ki/ki}$ Aldh1L1-eGFP mice at P84. Scale bar, 20 µm. **(D)** Schematic representation of analyzed mouse brain regions for phospho-ERM staining, the somatosensory cortex (SSp), and the dorsal medial striatum (DMS). **(E-H)** Representative confocal images of ERM phosphorylation (purple) in the SSp and DMS of WT or LRRK2 G2019S$^{ki/ki}$ Aldh1L1-eGFP mice at P21 (E-F) and at P84 (G-H). Scale bar, 200 µm. **(I)** Quantification of phospho-ERM integrated density in (E-H). For phospho-ERM integrated density at P21, nested t-test, unpaired two-tailed t-test. t (6) = 0.5005, p = 0.6346. n = 4 (WT, 2 males and 2 females), 4 (LRRK2 G2019S$^{ki/ki}$, 2 males and 2 females) mice. For phospho-ERM integrated density at P84, nested t-test, unpaired two-tailed t-test. t (6) = 0.8383, p = 0.1123. n = 4 (WT, 2 males and 2 females), 4 (LRRK2 G2019S$^{ki/ki}$, 2 males and 2 females) mice.

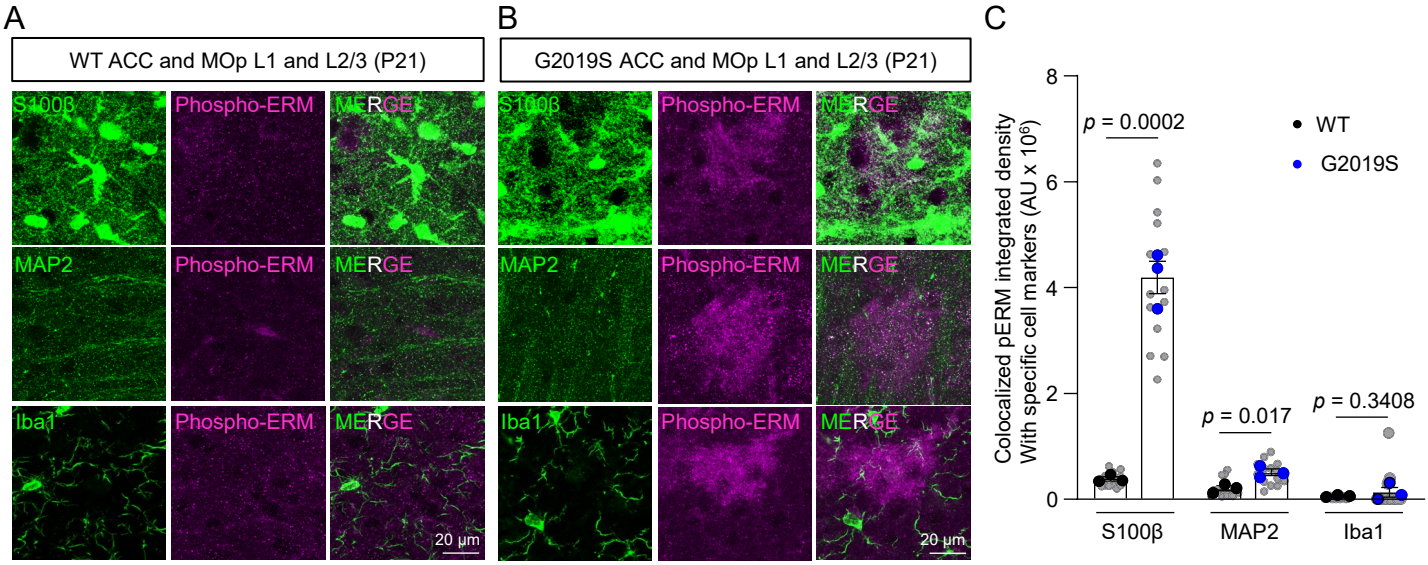

Figure S3: mouse phospho-ERM is significantly increased and colocalizes with S100β and MAP2. Related to Figure 1.

(A-B) Representative confocal images of phospho-ERM (purple) and S100β (green), MAP2 (green), or Iba1 (green) from the ACC and MOp of WT or LRRK2 G2019S$^{ki/ki}$ mice at P21. Scale bar, 20 µm. **(C)** Quantification of colocalized phospho-ERM integrated density with S100β, MAP2, and Iba1 in (D-E), n = 3 (WT, 1 male and 2 females), 3 (LRRK2 G2019S$^{ki/ki}$, 1 male and 2 females) mice, nested t-test, unpaired two-tailed t-test. For colocalized phospho-ERM with S100β, t (4) = 12.37, p = 0.0002. For colocalized phospho-ERM with MAP2, t (4) = 3.939, p = 0.017. For colocalized phospho-ERM with Iba1, t (4) = 1.08, p = 0.3408. Grey dots are the data acquired from each image. Black dots are the averaged data acquired from each WT mouse. Blue dots are the averaged data acquired from each LRRK2 G2019S$^{ki/ki}$ mouse.

Figure S4 (related to Figure 1) **Wang et al.,**

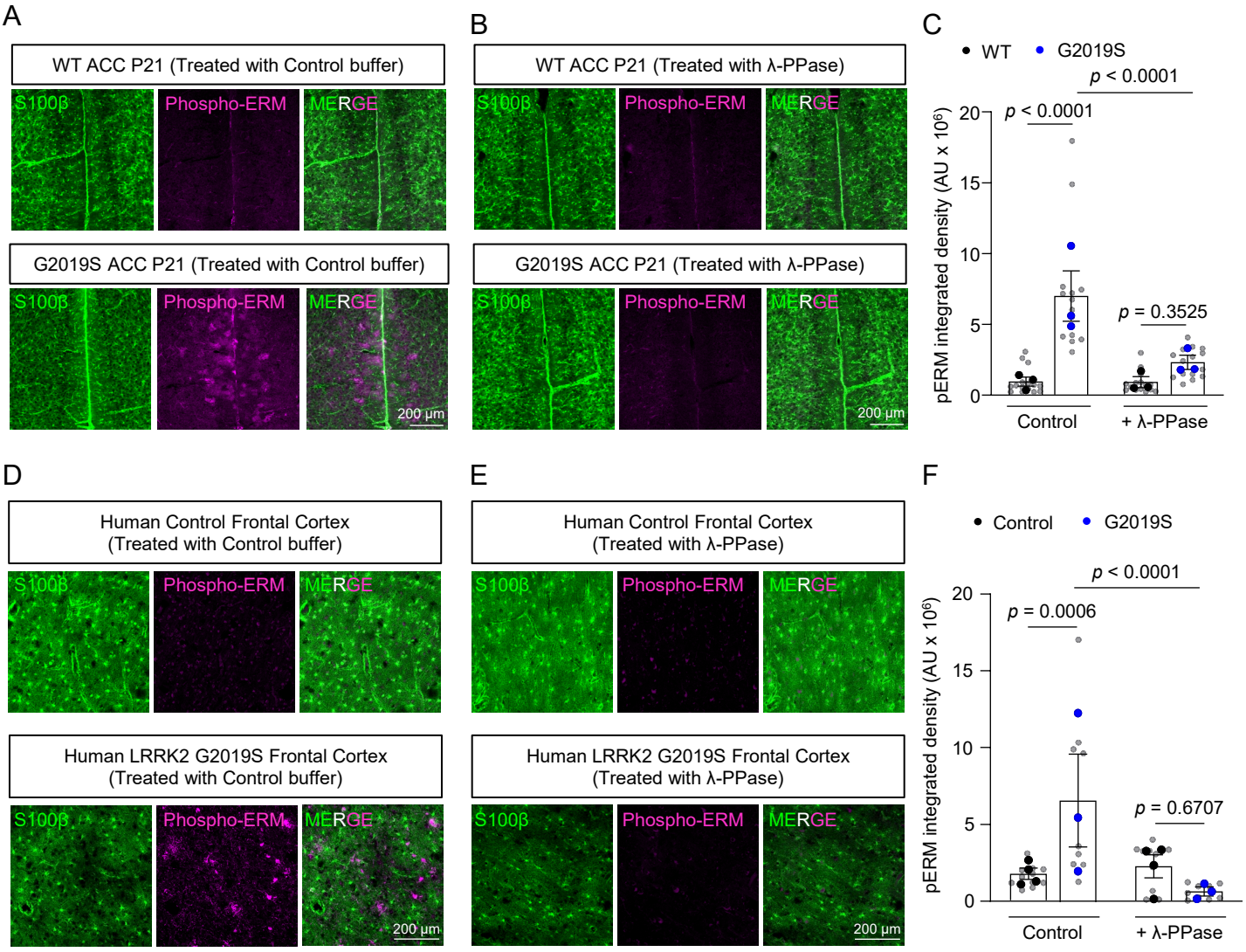

Figure S4: phospho-ERM is eliminated after Lambda protein phosphatase (λ-PPase) treatment. Related to Figure 1.

(A-B) Representative confocal images of S100β (green) and phospho-ERM (purple) in the ACC of WT or LRRK2 G2019S$^{ki/ki}$ mice at P21 with or without λ-PPase treatment. Scale bar, 200 μm. **(C)** Quantification of phospho-ERM integrated density in (A-B), n = 3 (WT, 1 male and 2 females), 3 (LRRK2 G2019S$^{ki/ki}$, 1 male and 2 females) mice, Nested One-way ANOVA [F (3, 56) = 25.19, $p < 0.0001$], Bonferroni's multiple comparisons test revealed a significant difference between WT mice and LRRK2 G2019S$^{ki/ki}$ mice without λ-PPase treatment ($p < 0.0001$, 95% C.I. = [-8107799, -3924949]), and between LRRK2 G2019S$^{ki/ki}$ mice with and without λ-PPase treatment ($p < 0.0001$, 95% C.I. = [2605448, 6788298]). alpha = 0.05. Grey dots are the data acquired from each image. Black dots are the averaged data acquired from each WT mouse. Blue dots are the averaged data acquired from each LRRK2 G2019S$^{ki/ki}$ mouse. **(D-E)** Representative confocal images of S100β (green) and phospho-ERM (purple) in the frontal cortex of human control subjects or human PD patients carrying LRRK2 G2019S mutation carriers at age >80 years old with or without λ-PPase treatment. Scale bar, 200 μm. **(F)** Quantification of phospho-ERM integrated density in (D-E), n = 4 (Human control, 3 males and 1 female), 3 (LRRK2 G2019S mutation carriers, 2 males and 1 female) subjects, Nested One-way ANOVA [F (3, 38) = 9.296, $p < 0.0001$], Bonferroni's multiple comparisons test revealed a significant difference between human control subjects and human PD patients carrying LRRK2 G2019S mutation carriers without λ-PPase treatment ($p = 0.0006$, 95% C.I. = [-7928018, -1867234]), and between human PD patients carrying LRRK2 G2019S mutation carriers with and without λ-PPase treatment ($p < 0.0001$, 95% C.I. = [2768186, 9247437]). alpha = 0.05. Grey dots are the data acquired from each image. Black dots are the averaged data acquired from each control subject. Blue dots are the averaged data acquired from each LRRK2 G2019S mutation carrier.

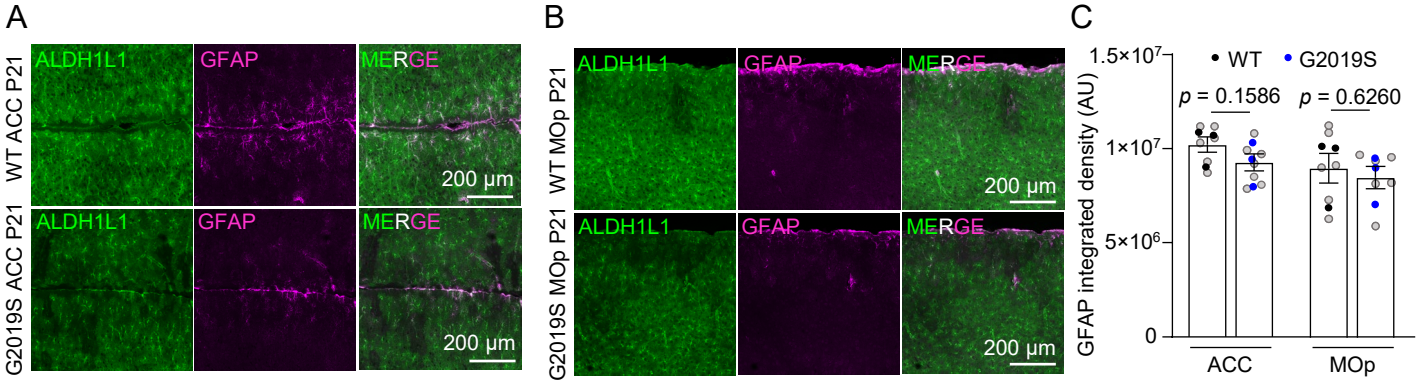

Figure S5: GFAP level is not altered in LRRK2 G2019S$^{ki/ki}$ ACC and MOp. Related to Figure 1.

(A-B) Representative confocal images of GFAP (purple) in the ACC and MOp of WT or LRRK2 G2019S$^{ki/ki}$ Aldh1l1-eGFP mice at P21. Scale bar, 200 µm. **(C)** Quantification of GFAP integrated density in (A-B), n = 3 (WT, 2 males and 1 female), 3 (LRRK2 G2019S$^{ki/ki}$, 2 males and 1 female) mice, For GFAP quantification in the ACC, nested t-test, unpaired two-tailed t-test. t (4) = 1.023, p = 0.364. For GFAP quantification in the MOp, nested t-test, unpaired two-tailed t-test. t (4) = 0.375, p = 0.7267. Grey dots are the data acquired from each image. Black dots are the averaged data acquired from each WT mouse. Blue dots are the averaged data acquired from each LRRK2 G2019S$^{ki/ki}$ mouse.

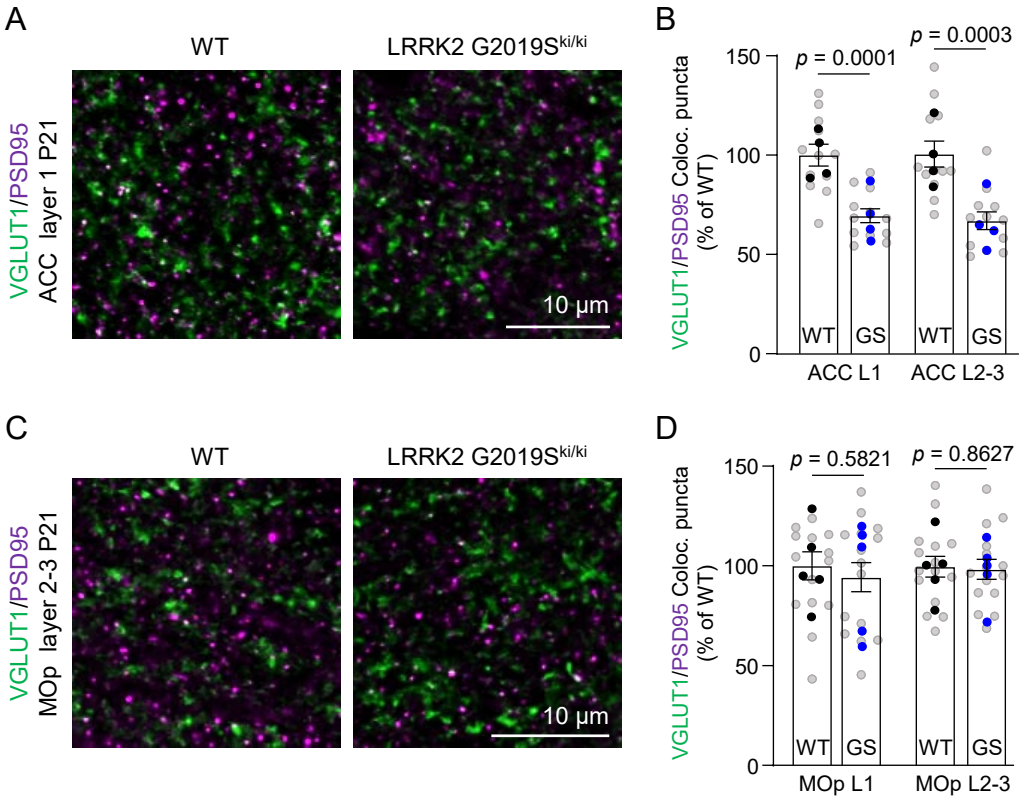

Figure S6: LRRK2 G2019S does not change excitatory synapse numbers in the primary motor cortex. Related to Figure 2.

(A) Representative images from the ventral ACC of WT and LRRK2 G2019S$^{ki/ki}$ mice that were stained with VGluT1 and PSD95 antibodies at P21. Scale bar, 10 µm. **(B)** Quantification of VGluT1-PSD95 co-localized puncta, normalized using the means of WT values in the ventral ACC. n = 4 (WT, 2 males and 2 females), 4 (LRRK2 G2019S$^{ki/ki}$, 2 males and 2 females) mice. Nested One-way ANOVA [F (3, 44) = 12.98, $p < 0.0001$], Bonferroni's multiple comparisons test revealed a significant difference between WT ACC L1 and LRRK2 G2019S$^{ki/ki}$ ACC L1 (p = 0.0002, 95% C.I. = [13.71, 47.33]), and between WT ACC L2-3 and LRRK2 G2019S$^{ki/ki}$ ACC L2-3 ($p < 0.0001$, 95% C.I. = [16.48, 50.10]). alpha = 0.05. **(C)** Representative images from the MOp of WT and LRRK2 G2019S$^{ki/ki}$ mice that were stained with VGluT1 and PSD95 antibodies at P21. Scale bar, 10 µm. **(D)** Quantification of VGluT1-PSD95 co-localized puncta, normalized using the means of WT values in the MOp L1 and L2-3. n = 5 (WT), 5 (LRRK2 G2019S$^{ki/ki}$) mice, 3 males and 2 females. Nested One-way ANOVA [F (3, 56) = 0.1837, p = 0.9070], Bonferroni's multiple comparisons test revealed a significant difference between WT MOp L1 and LRRK2 G2019S$^{ki/ki}$ MOp L1 ($p > 0.9999$, 95% C.I. = [-14.69, 25.97]), and between WT MOp L2-3 and LRRK2 G2019S$^{ki/ki}$ MOp L2-3 ($p > 0.9999$, 95% C.I. = [-19.06, 21.61]). alpha = 0.05. Grey dots are the data acquired from each image. Black dots are the averaged data acquired from each WT mouse. Blue dots are the averaged data acquired from each LRRK2 G2019S$^{ki/ki}$ mouse.

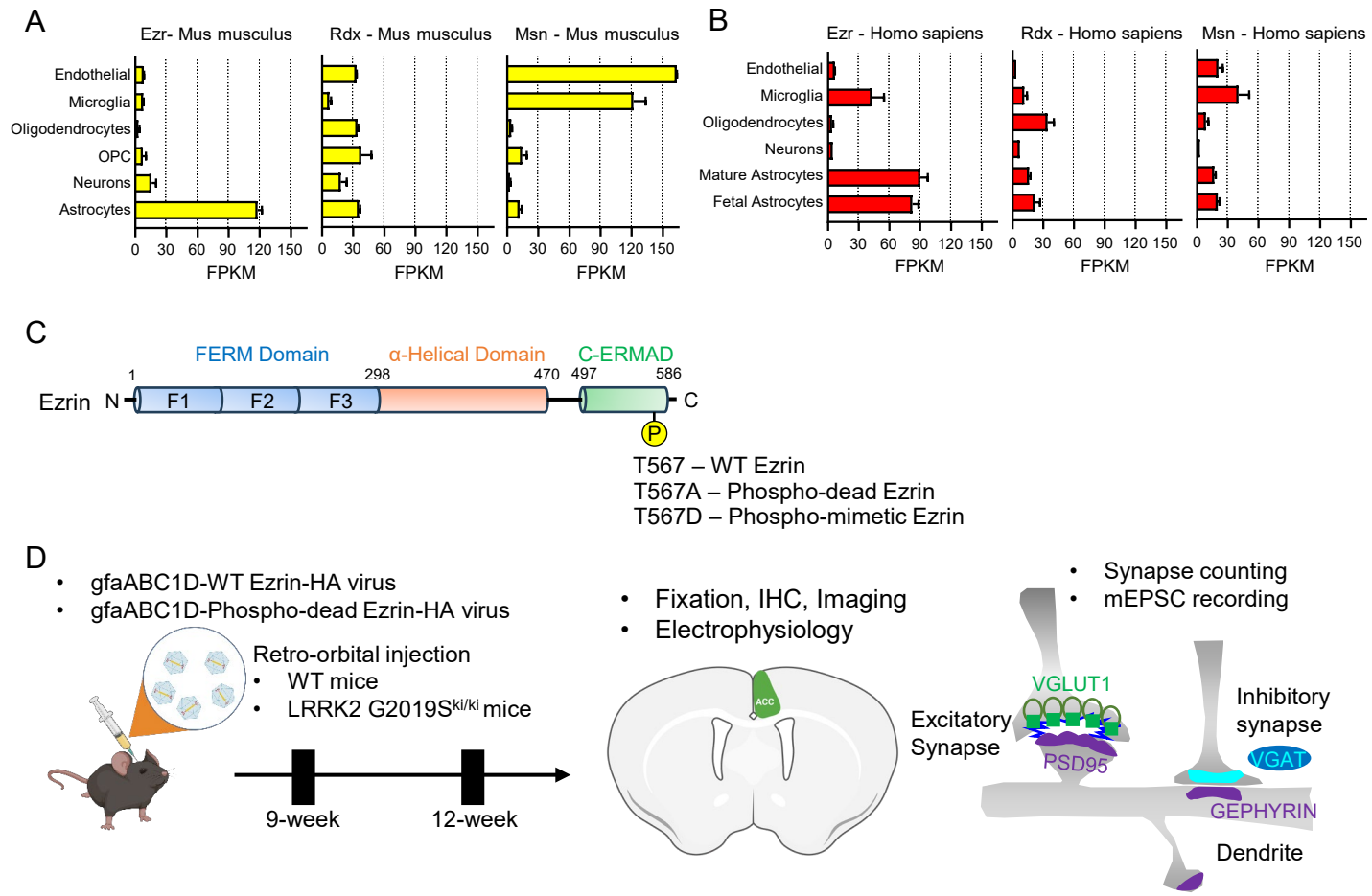

Figure S7: Overexpression of AAV-HA-tagged-WT Ezrin and AAV-HA-tagged-Phospho-dead Ezrin in WT and LRRK2 G2019S$^{ki/ki}$ astrocytes. Related to Figure 4.

(A-B) Bar plots of Ezr, Rdx, and Msn gene expression in various brain cell types in mice (yellow) or humans (red). These plots are generated using publicly available data at https://www.brainrnaseq.org **(C)** Schematic of domains within Ezrin. **(D)** Experiment workflow of AAV-HA-tagged-WT Ezrin and AAV-HA-tagged-Phospho-dead Ezrin in WT and LRRK2 G2019S$^{ki/ki}$ astrocytes.

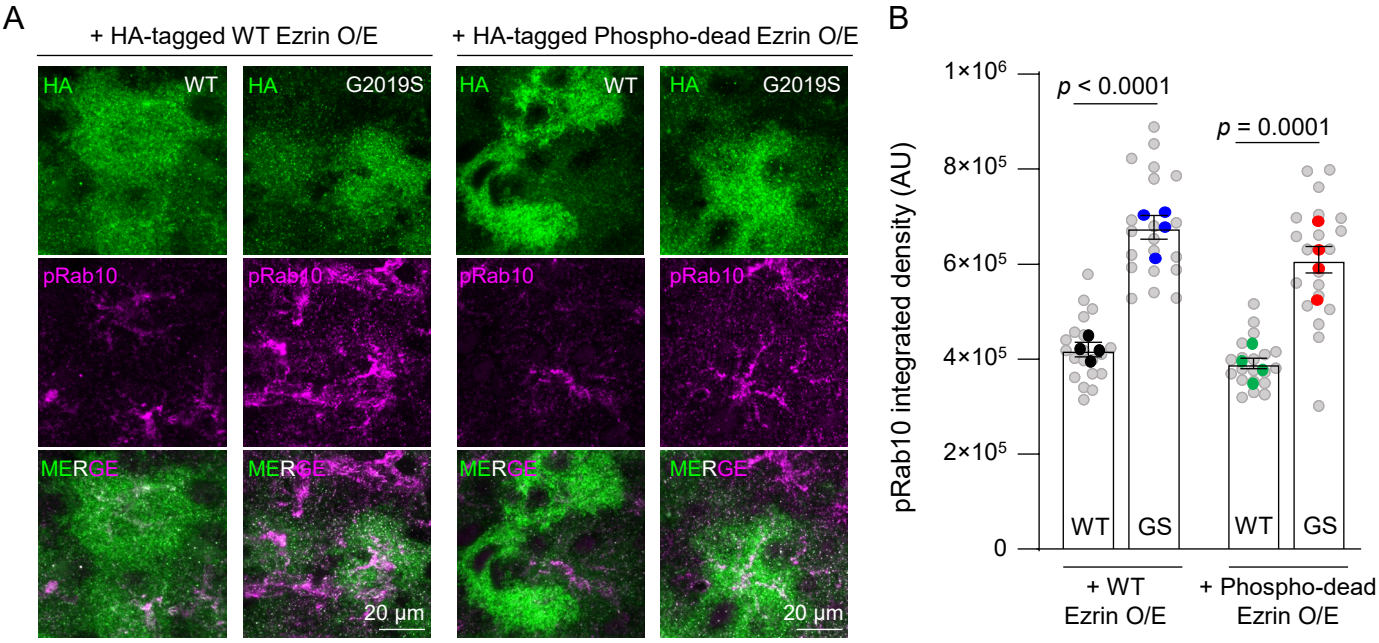

Figure S8: Overexpression of AAV-HA-tagged-WT Ezrin and AAV-HA-tagged-Phospho-dead Ezrin in WT and LRRK2 G2019S$^{ki/ki}$ astrocytes. Related to Figure 4.
(A) Representative images from the ventral ACC of WT and LRRK2 G2019S$^{ki/ki}$ mice injected with AAV-HA-tagged WT Ezrin or Phospho-dead Ezrin, stained with HA and phospho-Rab10 antibodies at P84. Scale bar, 20 µm. **(B)** Quantification of phospho-Rab10 integrated density. n = 4 per group (2 males and 2 females). One-way ANOVA [$F(3,12) = 38.34$, $p < 0.0001$] with Bonferroni's post hoc test revealed significant differences between groups, except WT + WT Ezrin O/E vs. WT + Phospho-dead Ezrin O/E ($p > 0.9999$) and LRRK2 G2019S$^{ki/ki}$ groups ($p = 0.3303$).

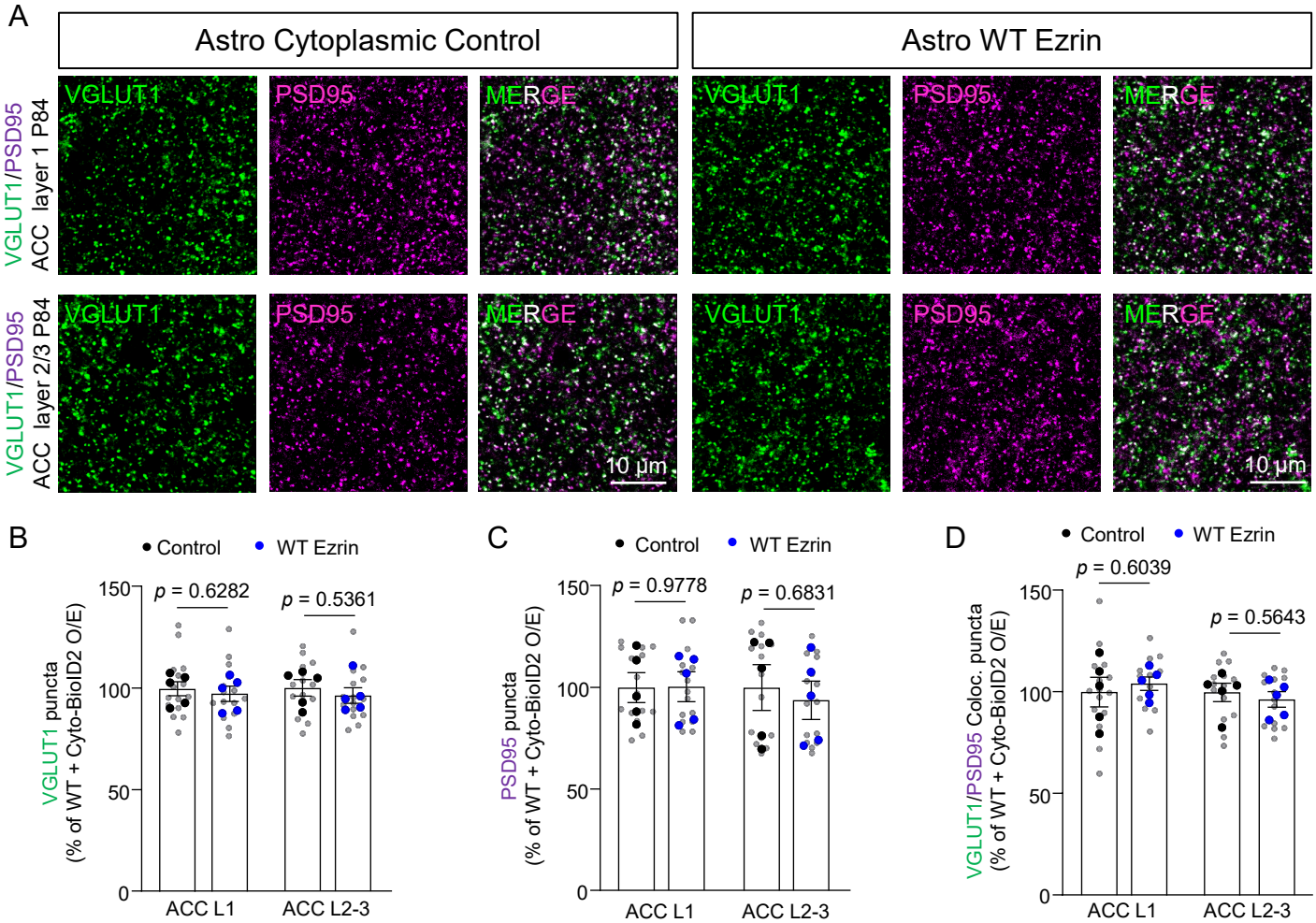

Figure S9: WT Ezrin overexpression does not change excitatory synapse numbers in the ACC of WT mice. Related to Figure 4.

(A) Representative images from the ventral ACC of WT mice injected with AAV-HA-tagged BirA2 (cytoplasmic control) or WT Ezrin that were stained with VGLUT1 and PSD95 antibodies at P84. Scale bar, 10 µm. **(B)** Quantification of VGLUT1 puncta, normalized using the means of BirA2 values in the ventral ACC. n = 5 mice per group. For ACC L1, nested t-test, unpaired two-tailed t-test. t (8) = 0.5035, p = 0.6282. For ACC L2/3, nested t-test, unpaired two-tailed t-test. t (8) = 0.6465, p = 0.5361. **(C)** Quantification of PSD95 puncta, normalized using the means of BirA2 values in the ventral ACC. n = 5 mice per group. For ACC L1, nested t-test, unpaired two-tailed t-test. t (8) = 0.02872, p = 0.9778. For ACC L2/3, nested t-test, unpaired two-tailed t-test. t (8) = 0.4235, p = 0.6831. **(D)** Quantification of VGLUT1-PSD95 puncta, normalized using the means of BirA2 values in the ventral ACC. n = 5 mice per group. For ACC L1, nested t-test, unpaired two-tailed t-test. t (8) = 0.5400, p = 0.6039. For ACC L2/3, nested t-test, unpaired two-tailed t-test. t (8) = 0.6013, p = 0.5643.

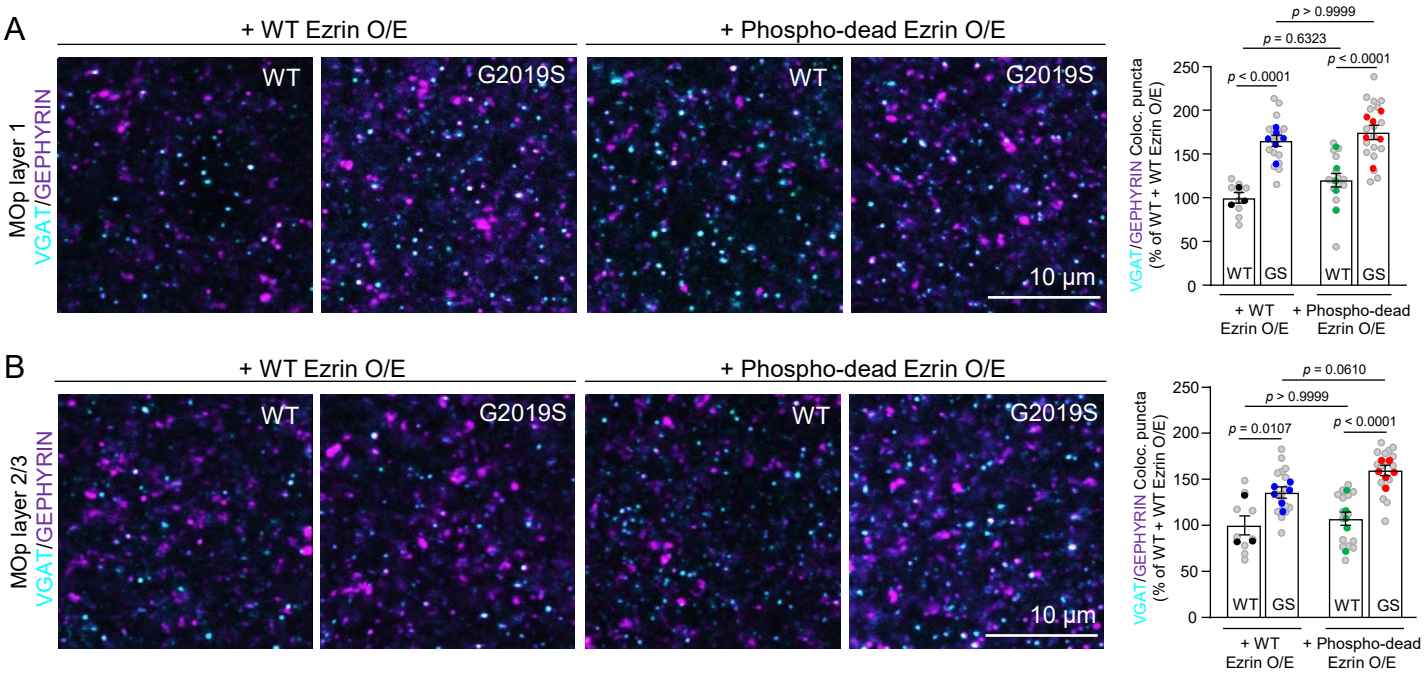

Figure S10: Overexpression of AAV-HA-tagged-WT Ezrin and AAV-HA-tagged-Phospho-dead Ezrin in WT and LRRK2 G2019S$^{ki/ki}$ astrocytes. Related to Figure 4.
(A) Representative images from the MOp L1 of the same groups stained with VGAT and GEPHYRIN antibodies. Scale bar, 10 µm. Quantification of VGAT-GEPHYRIN co-localized puncta, normalized to WT + WT Ezrin O/E. n = 3–6 per group. One-way ANOVA [$F(3,55) = 19.7$, $p < 0.0001$] with Bonferroni's post hoc test revealed significant differences between WT + WT Ezrin O/E and LRRK2 G2019S$^{ki/ki}$ + WT Ezrin O/E, and between WT + Phospho-dead Ezrin O/E and LRRK2 G2019S$^{ki/ki}$ + Phospho-dead Ezrin O/E ($p < 0.0001$). No differences were found between WT or LRRK2 G2019S$^{ki/ki}$ groups within Ezrin conditions ($p > 0.05$). **(B)** Representative images from the MOp L2-3 of WT and LRRK2 G2019S$^{ki/ki}$ mice injected with AAV-HA-tagged WT Ezrin or Phospho-dead Ezrin, stained with VGAT and GEPHYRIN antibodies at P84. Scale bar, 10 µm. Quantification of VGAT-GEPHYRIN co-localized puncta normalized to WT + WT Ezrin O/E. n = 3–6 per group. One-way ANOVA [$F(3,54) = 15.10$, $p < 0.0001$] with Bonferroni's post hoc test showed significant differences between WT + WT Ezrin O/E and LRRK2 G2019S$^{ki/ki}$ + WT Ezrin O/E ($p = 0.0107$) and between WT + Phospho-dead Ezrin O/E and LRRK2 G2019S$^{ki/ki}$ + Phospho-dead Ezrin O/E ($p < 0.0001$). No differences were observed between WT groups ($p > 0.9999$) or between LRRK2 G2019S$^{ki/ki}$ groups ($p = 0.0610$).

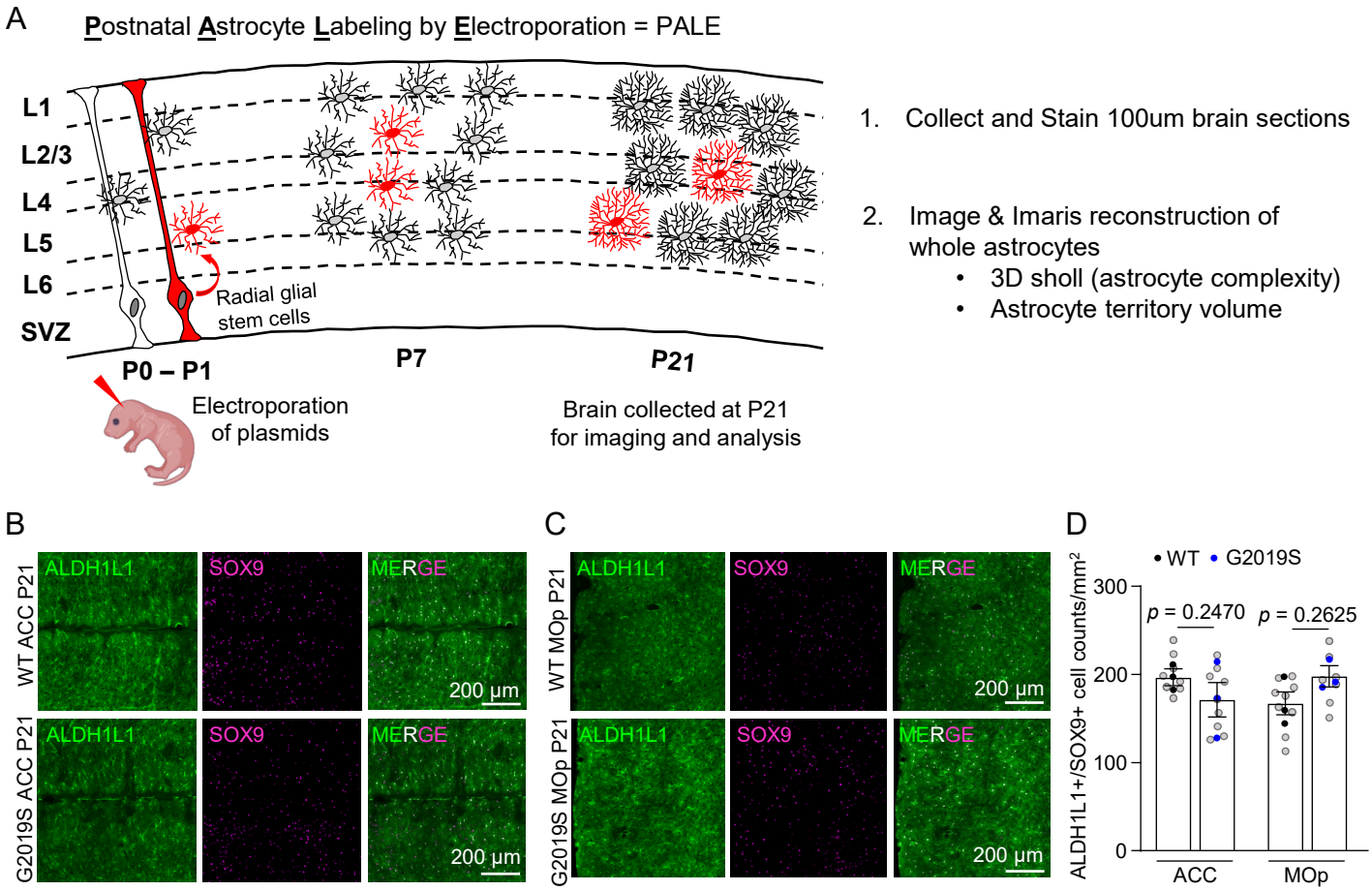

Figure S11: LRRK2 G2019S does not change ALDH1L1+/SOX9+ cell numbers in the ACC and MOp. Related to Figure 5.

(A) Overview of postnatal astrocyte labeling by electroporation (PALE) with PiggyBac plasmids. **(B-C)** Representative confocal images of SOX9 (purple) in the ACC and MOp of WT or LRRK2 G2019S$^{ki/ki}$ Aldh1l1-eGFP mice at P21. Scale bar, 200 µm. **(D)** Quantification of ALDH1L1+/SOX9+ cell numbers in (B-C), n = 3 (WT, 2 males and 1 female), 3 (LRRK2 G2019S$^{ki/ki}$, 2 males and 1 female) mice, For ALDH1L1+/SOX9+ cell counting in the ACC, nested t-test, unpaired Two-tailed t-test. t (4) = 0.9619, p = 0.3906. For ALDH1L1+/SOX9+ cell counting in the MOp, nested t-test, unpaired two-tailed t-test. t (4) = 1.684, p = 0.1675. Grey dots are the data acquired from each image. Black dots are the averaged data acquired from each WT mouse. Blue dots are the averaged data acquired from each LRRK2 G2019S$^{ki/ki}$ mouse.

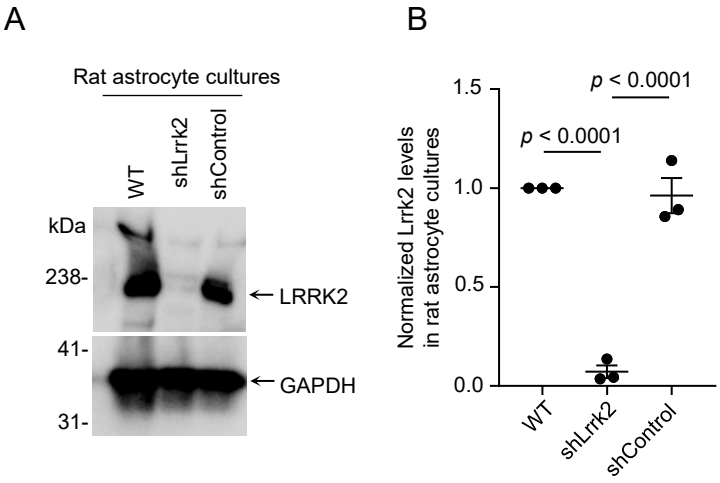

Figure S12: Expression of LRRK2 in astrocytes. Related to Figure 5.
(A) Cultured WT, shControl, and shLrrk2 transfected rat cortical astrocytes were lysed, and cytoplasmic proteins were subjected to Western blotting using LRRK2 and GAPDH antibodies. Results are representative of 3 independent experiments. **(B)** Densitometric analysis of LRRK2 levels in (E). Signals corresponding to LRRK2 were first normalized to that for β-actin. Relative LRRK2 levels were then normalized to the LRRK2 signals in WT rat cortical astrocytes. Statistical significance was determined by One-way ANOVA [$F(2, 6) = 92.25$, $p < 0.0001$], Bonferroni multiple comparisons revealed a significant difference between WT and shLrrk2 ($p < 0.0001$, 95% C.I. = [0.6743, 1.183]) and between shLrrk2 and shControl ($p < 0.0001$, 95%C.I. = [-1.145, -0.6363]) and no differences between WT and shControl ($p > 0.9999$, 95%C.I. = [-0.2165, 0.2923]), alpha = 0.05.

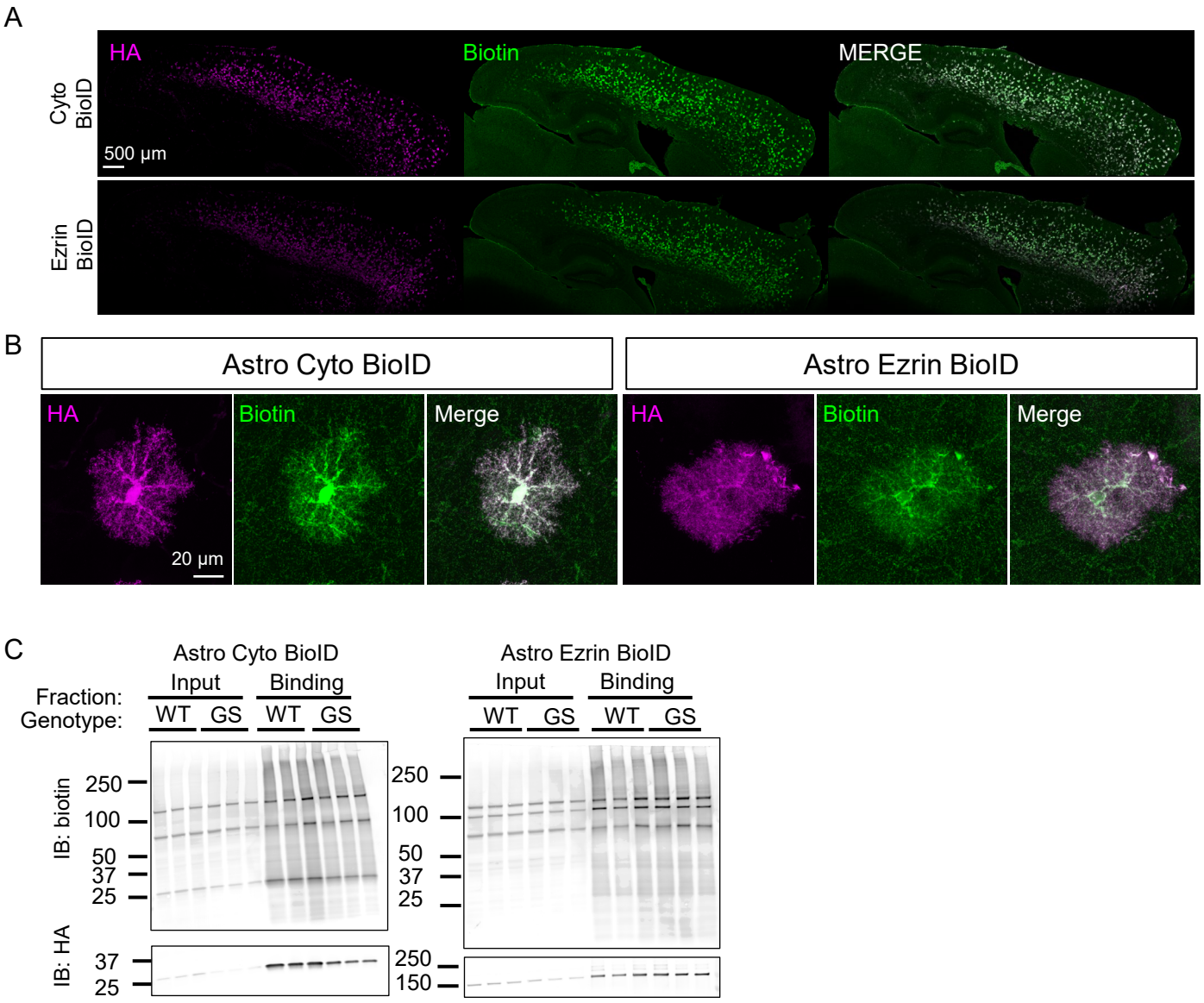

Figure S13: BioID constructs expression and biotinylation *in vivo* and *in vitro*. Related to Figure 6.

(A-B) Representative images of *in vivo* expression in the cortex of different BioID constructs labeled with HA and the biotinylating activity labeled with streptavidin. Merged images show the colocalization of HA and biotin signals in astrocytes. Scale bar, 500 µm (A). Scale bar, 20 µm (B). **(C)** Western blot analysis of BioID constructs expression (HA) and biotinylation activity (Streptavidin) *in vitro* in cortical lysates and subsequent immunoprecipitation.

Figure S14 (related to Figure 6) **Wang et al.,**

A

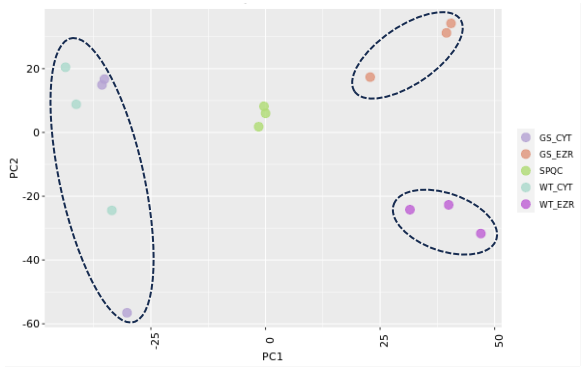

B

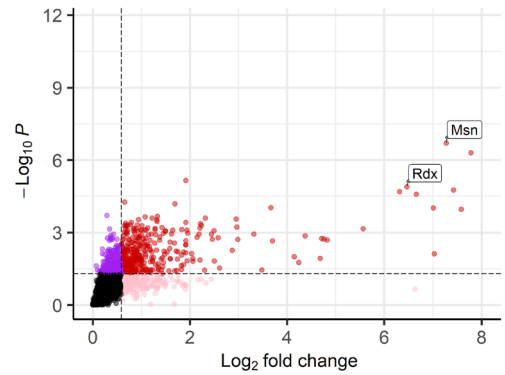

C

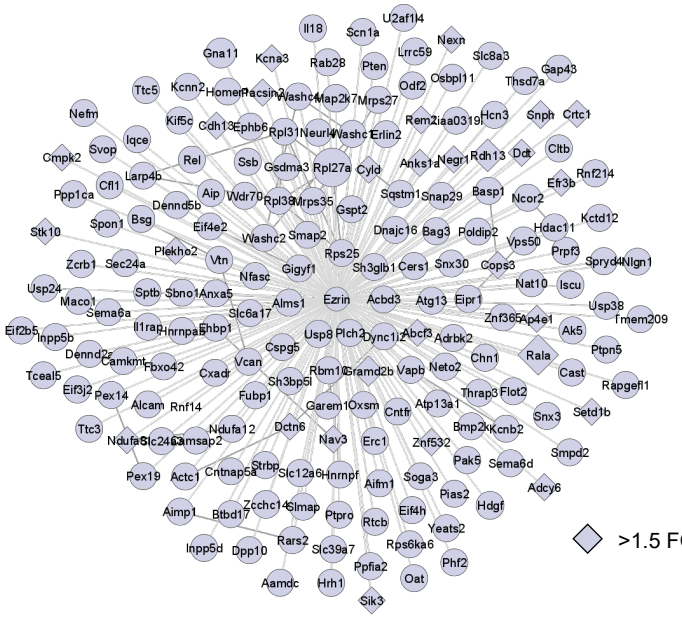

D

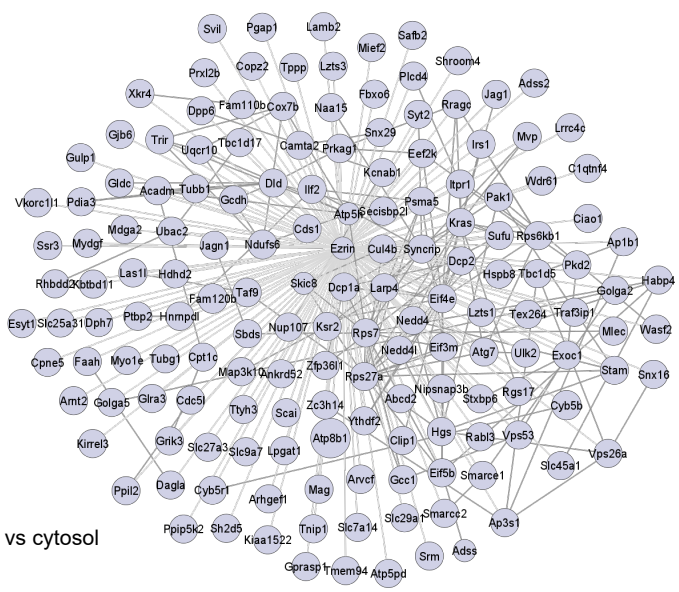

>1.5 FC vs cytosol

E

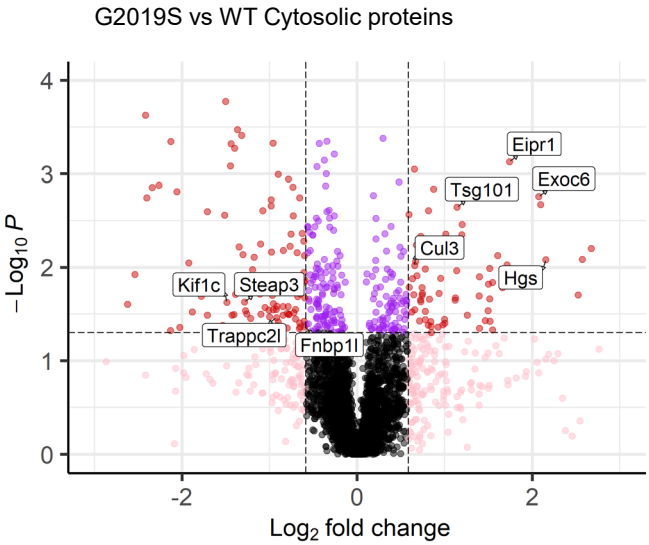

F

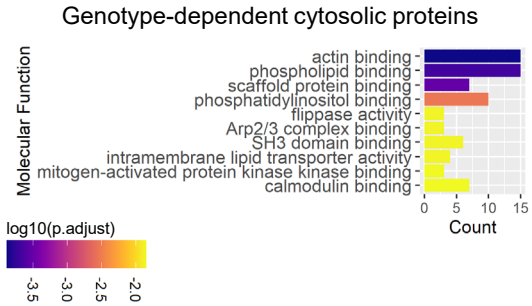

G

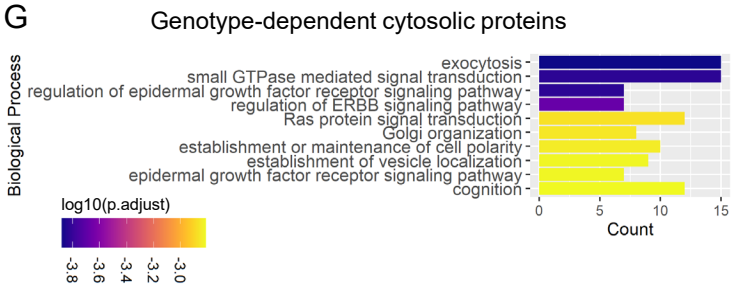

Figure S14: LRRK2 G2019S changes the composition of cytoplasmic proteins in astrocytes *in vivo*. Related to Figure 6.

(A) Principle component analyses (PCA) of Cyto-BioID (control) and Ezrin-BioID (bait) samples. **(B)** The plot shows that Radixin and Moesin, known as Ezrin interacting proteins, are significantly enriched in the Ezrin-BioID sample compared to Cyto-BioID. **(C-D)** Interaction networks depict Ezrin interactions detected by BioID and known protein-protein interactions identified in the publicly available stringDB database for proteins with gained (C) or lost (D) proximity to Ezrin in LRRK2 G2019S$^{ki/ki}$ astrocytes compared to WT astrocytes. **(E)** Volcano plot showing the differential abundance of cytosolic proteins in WT and LRRK2 G2019S$^{ki/ki}$ cortices. **(F-G)** Bars show the top 10 most significant Gene Ontology (GO) terms, ordered by highest gene count and lowest adjusted p-value, for the proteins differentially detected by Astro-cyto-BioID in WT compared to LRRK2 G2019S$^{ki/ki}$ (F) Molecular function (G) Biological Process.

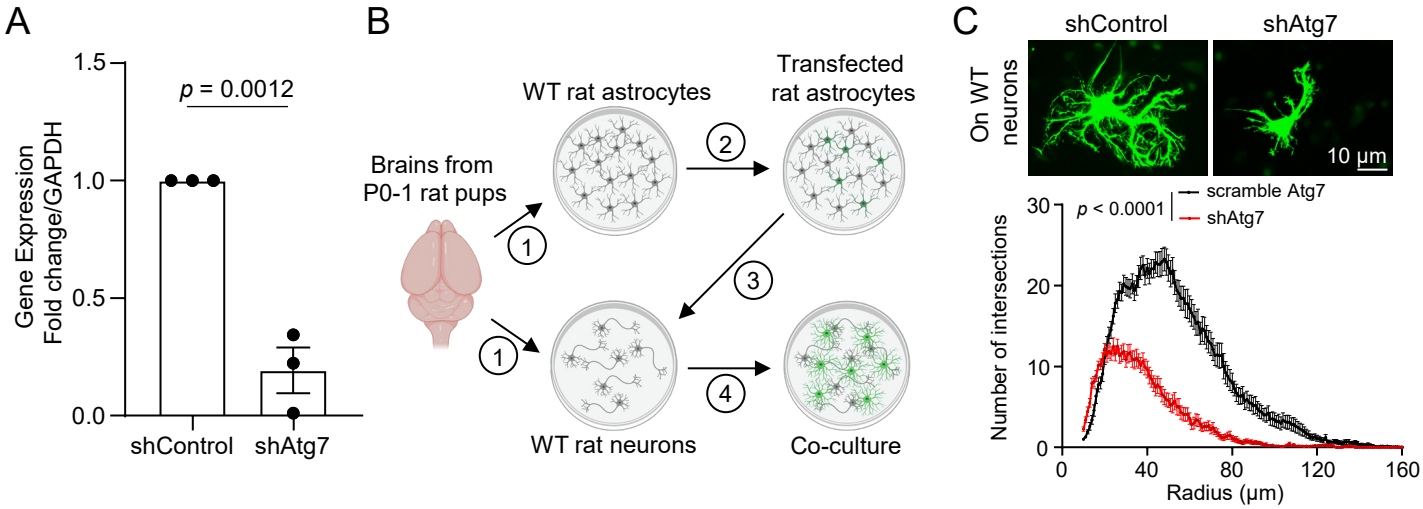

Figure S15: Astrocytic Atg7 is essential astrocyte morphological complexity *in vitro*. Related to Figure 7.

(A) Comparable expression of Atg7 mRNA transcripts by RT-PCR in N2A cells transfected with scrambled shRNA (shControl-GFP) or shRNA targeting Atg7 (shAtg7-GFP). n = 3 independent cultures. unpaired Two-tailed t-test. t (4) = 8.258, p = 0.0012. **(B)** Schematic of astrocyte-neuron co-culture assay. **(C)** (Upper) Rat cortical astrocytes transfected with scrambled shRNA (shControl-GFP) or shRNA targeting Atg7 (shAtg7-GFP) co-cultured with wild-type cortical neurons. Scale bar, 10 µm. (Lower) Quantification of astrocyte branching complexity. n = 30 (shControl-GFP), 30 (shAtg7-GFP) astrocytes co-cultured with WT cortical neurons compiled from two independent experiments. We fitted a linear mixed model with a number of intersections as the outcome variable, condition as a predictor, and a number of cells and cell radius entered as random effects. Within this model, shAtg7 (beta = 2.91, t(58) = 7.14) led to a significant decrease in the number of intersections compared to shControl astrocytes (beta = 7.89, t(58) = 19.35). Tukey multiple comparisons test revealed a significant difference between shControl and shAtg7 astrocytes co-cultured on WT neurons (p < 0.0001).